Qubit dynamics under alternating controls

by

Clarice Demarchi Aiello

Submitted to the Department of Electrical Engineering
and Computer Science
in partial fulfillment of the requirements for the degree of

Doctor of Philosophy in Computer Science and Engineering

at the

MASSACHUSETTS INSTITUTE OF TECHNOLOGY

September 2014

Author ..... Signature redacted .....
Department of Electrical Engineering
and Computer Science
July 25, 2014

Certified by ..... Signature redacted ..
Paola Cappellaro
Esther and Harold E. Edgerton Associate Professor
of Nuclear Science and Engineering
Thesis Supervisor

Accepted by ..... Signature redacted .....
Leslie Kolodziejski
Chairman, Department Committee on Graduate Theses

Qubit dynamics under alternating controls

by

Clarice Demarchi Aiello

Submitted to the Department of Electrical Engineering
and Computer Science
on July 25, 2014, in partial fulfillment of the
requirements for the degree of
Doctor of Philosophy in Computer Science and Engineering

Abstract

In this thesis, we discuss two problems of quantum dynamics in the presence of alternating controls. Alternating controls arise in many protocols designed to extend the duration over which a qubit is a useful computational resource. This is accomplished by control sequences that either retard decoherence, or that accomplish a quantum operation in as short a time as possible.

The first problem tackles the use of a composite-pulse control sequence known as 'rotary-echo' for quantum magnetometry purposes. The sequence consists in the continuous drive of a qubit, with field phases that alternate at specific intervals. We implement such a magnetometry protocol using an electronic qubit in diamond, and experimentally confirm the flexibility yielded by the tuning of sequence parameters that achieves a good compromise between decoherence resilience and sensitivity.

The second problem theoretically investigates the time-optimal evolution of a qubit in the case of a restricted control set composed of alternating rotations around two non-parallel axes on the Bloch sphere. Using accessible algebraic methods, we show that experimental parameters, such as the angle between the two rotation axes, restrict the necessary structure of time-optimal sequences. We propose to implement such an evolution through alternate driving as an advantageous alternative to the slow, noisy direct addressing of a nuclear qubit anisotropically hyperfine-coupled to an electronic spin in diamond.

Thesis Supervisor: Paola Cappellaro
Title: Esther and Harold E. Edgerton Associate Professor
of Nuclear Science and Engineering

Acknowledgments

I am incredibly grateful for the support of the following people - in reverse alphabetical order:

- Vera, for teaching and mentoring me on everything teaching and mentoring
- thesis committee: Franco, Scott & Terry, for being so generous with their time
- Teaching and Learning Lab: the wonderful Janet, Dipa, Leann, for teaching me to teach without numbers
- students (6.728-F09, 6.728-F13, TCP-S14), for the most fulfilling times at MIT
- Research Lab of Electronics staff, always always on top of things: Al & Bill, Dave & Will, Erik, Joanna...
- Peter, my mentor
- Paola, my advisor and mentor
- Office of the Dean for Graduate Education: Dean Ortiz, Dean Staton, Jessica, for their genuine care
- Michele, my also-lefty-also-reader collaborator
- Masashi, for being there from Day 1
- Leslie, who has the back of every single EECS grad student
- Laura, organizational mastermind
- Jane, humanist with a *goût* for statistics
- International Students Office: Danielle and warm crew
- graduate offices' heros: Janet, Clare, Peter, Angelita, Alicia, Lisa...
- friends from home: Ri (coping with me *est.* 2000) & Ieva, Mari & Gu, Helena & Christian & baby, Clau & Tchelo & Gabi & baby

- friends from here: the Quantum Girls, the Brain-Damaged Monkey Society, Jamie, Orso & Luz, Vero & Jason, Irina & Sebastian, Qi & Florian, Liza, QEGgers, Doylers
- family, my dear dear family: mãe & pai, vó & vô, my Boetter-half
- co-outreachers, with gratitude: Tornado team, CUA Kids Day, IAP's Implementations of Quantum Computing, Quantum Mechanics Slam
- co-organizers of the Brazil Symposium, the sunny Ale, Cris & Rosa
- Boerge, for inspiring me, and for being the scientist I aspire to become

Contents

List of Figures

List of Tables

Chapter 1

Introduction

The emergence of quantum information science and technology has seen the concomitant development of many different implementations of quantum bits (qubits). These are paving the way for both 'crypto-cracker' quantum computers and quantum sensors with unprecedented resolution. Solid-state quantum systems such as electronic and nuclear spins are among the most promising qubit candidates, due to their potential scalability and engineering properties.

Nevertheless, such solid-state qubit implementations strongly couple to a complex lattice environment that accelerates their decoherence, or loss of quantum character, in a much more dramatic fashion than, for example, in isolated atomic systems. Thus, in order to harness the usefulness of solid-state qubits, it is of relevance to develop quantum control protocols that either mitigate the effect of noise, or are realized in as little time as possible.

In this thesis, we concentrate on one control protocol that can tackle different realistic situations of noise strength and origin, in the context of nano-magnetometry; and on another control protocol aimed at synthesizing qubit unitaries in a time-optimal way.

The two protocols have some similarities. They are 'bang-bang' control schemes:

in both cases there is always a parameter that instantaneously alternates between discrete values. This switching - and the unwelcoming discontinuities it brings - adds to the richness of the ensuing dynamical description. In the magnetometry protocol, the control field is always 'on'; especially for solid-state implementations, continuous excitation can be beneficial because the dephasing time of the quantum system is naturally extended (in the sense that a kicked oscillator will oscillate for longer than a free-evolving one). The time-optimal protocol, in turn, can be experimentally implemented with controls which are always 'on', or with pulsed controls.

We focus our experiments and theoretical proposals on a spinor qubit stemming from a well-known color center in diamond, the so-called single negatively charged nitrogen-vacancy center. This center counts as a relevant qubit candidate due to the fact that it combines electronic spin degrees of freedom with strong transitions that allow for it to be addressed optically. It is, in addition, very stable, so that it can be regarded as nature's own 'trapped ion'.

The above mentioned protocols are described in what follows, together with the organization of this thesis.

1.1 A flipping of phases: composite-pulse magnetometry

In Chapters 2 and 3 of this thesis, we theoretically and experimentally investigate a magnetometry scheme using a solid-state nanosensor. Quantum magnetometry employs the fact that, in the presence of an external magnetic field, the Zeeman effect causes an energy shift which is spin-dependent; a known resonance between two distinct spin states is changed by an amount which is proportional to the strength of the external magnetic field. The problem of measuring a magnetic field is thus mapped into the problem of measuring the detuning from a known resonance.

Our proposed method for measuring such detunings is based on a composite-pulse known as 'rotary-echo' and having roots in nuclear magnetic resonance. Composite-pulses are continuous excitation sequences with a smart tayloring of the pulse phases. Specifically, the rotary-echo has a periodic shift of the excitation phases by π.

We could show that the dynamics of a qubit nanosensor subjected to a continuous stream of rotary-echoes can be chosen so as to maximize either resilience to different types of noise, or sensitivity. This tunable trade-off makes the control protocol attractive in realistic experimental settings.

1.2 A flipping of rotation axes: time-optimal algebraic $SU(2)$ synthesis with alternating controls

Quantum operations are only useful if they preserve the quantum coherence of the system; a figure of merit is the number of gates that can be performed before decoherence has kicked in. In this sense, it is relevant to learn how best to synthesize unitaries in as short a time as possible, given the available control resources.

In Chapter 4 of this thesis, we explore the structure of time-optimal operations in $SU(2)$ in the case of a restricted control set that only allows rotations around two non-parallel axis of the Bloch sphere. Employing an accessible algebraic method, we can determine necessary conditions that time-optimal sequences generating any unitary in $SU(2)$ must fulfill; these conditions depend on experimental parameters such as the angle between the two rotation axes.

There are relevant experimental settings for which, indeed, resources are limited and described by the control set in question; in particular, when amplitude and phase modulation of the fields is not a trivial task; and when degrees of freedom are restricted, as for nuclear qubits anisotropically hyperfine-coupled to an electronic qubit.

This latter case is discussed in detail in Chapter 5, considering the specific case of a proximal ^{13}C nuclear spin hyperfine coupled to the electronic spin of a nitrogen-vacancy center. When compared with direct driving, we show that there are experimentally relevant scenarios for which the nuclear qubit can be steered, in a faster and virtually noise-free fashion, solely by switching between electronic spin states.

Chapter 2

Composite-pulse magnetometry: theory

The unparalleled sensitivity offered by quantum magnetometers [1] is challenged by experimental imperfections and, especially in the solid-state, by their relatively short coherence times. Standard refocusing techniques can overcome these limitations and improve the sensitivity to periodic (AC) fields, but they come at the cost of reduced bandwidth and are thus not applicable to sensing static (DC) or aperiodic fields.

In this Chapter, we theoretically investigate a DC quantum magnetometry protocol. We show that continuous driving of the sensor spin by composite pulses [2] yields a flexible magnetometry scheme, mitigating both power imperfections in the interrogation pulses and decoherence due to a spin bath. We demonstrate the method using a continuous sequence of a composite pulse known as 'rotary-echo' (RE) [3], which consists of two consecutive pulses of identical duration and phases shifted by π.

After a discussion of the sensitivity yielded by the rotary-echo control scheme, we study how the sensor spin under this sequence reacts to the presence of different types of noise. We determine that the rotary-echo magnetometry scheme is flexible, as a suitable choice of the pulse length compensates for different scenarios of noise strength and origin, allowing adjustment to experimental conditions.

2.1 Introduction

Magnetometry schemes based on quantum spin probes (qubits) usually measure the detuning $\delta\omega$ from a known resonance. The most widely used method is Ramsey spectroscopy [4], which measures the relative phase $\delta\omega \cdot t$ the qubit acquires when evolving freely for a time t after preparation in a superposition state. In the solid state, a severe drawback of this scheme is the short free-evolution dephasing time, $T_2^\star$, which limits the interrogation time.

Dynamical decoupling (DD) techniques such as Hahn-echo [5] or CPMG [6] sequences can extend the coherence time. Unfortunately, such schemes also refocus the effects of static magnetic fields and are thus not applicable for DC-magnetometry. Even if $\delta\omega$ oscillates with a known frequency (AC-magnetometry), DD schemes impose severe restrictions on the bandwidth, as the optimal sensitivity is reached only if the AC field period matches the DD cycle time [1].

Schemes based on continuous driving are thus of special interest for metrology in the solid-state because they can lead to extended coherence times [7], without completely cancelling out the field to be measured. Recently, DC-magnetometry based on Rabi frequency beats was demonstrated [8]; in that method, a small frequency shift $\delta\omega$ along the static magnetic field produces a shift $\approx \frac{\delta\omega^2}{2\Omega}$ in the bare Rabi frequency Ω. Despite ideally allowing for very long interrogation times, on the order of the Rabi fringe decay which approaches the relaxation time T_1, limiting factors such as noise in the driving field [8] and the bad scaling in $\delta\omega \ll \Omega$ make Rabi-beat magnetometry unattractive.

Composite-pulses [2] can provide not only a better refocusing of the driving field inhomogeneities, but also different scaling with frequency offsets, and can thus be

used for improved magnetometry. Our method both extends coherence times, and keeps a good signal scaling with respect to $\delta\omega$, which increases sensitivity.

2.2 Background: sensitivity in metrology protocols

Consider N measurements with results $\{m_1, m_2, \ldots, m_N\}$. One wants to use a function $B_{\text{est}}(m_1, m_2, \ldots, m_N)$ to estimate the true value of a relevant parameter B. To characterize how precisely the N data points determine the parameter B, one could simply use the variance of the estimator,

$$(\Delta B_{\text{est}})^2 \equiv \langle B_{\text{est}}^2 \rangle - \langle B_{\text{est}} \rangle^2 \; ; \tag{2.1}$$

however, considering the variance of the estimator alone does not guarantee that the estimator is unbiased, i.e., that $\langle B_{\text{est}} \rangle = B$; the estimator mean could be very sharply centered around a value removed from the true parameter value. Moreover, and this will be of relevance in the studied case, the estimator could potentially have different units from the parameter; in this case, the variance of the estimator might not be a clear measure of parameter accuracy. To tackle both issues, one can define a better statistical measure of the distance between a parameter B and its estimator B_{est} through the parameter increment δB [9, 10],

$$\delta B \equiv \frac{B_{\text{est}}}{\left| \frac{\partial B_{\text{est}}}{\partial B} \right|} - B \; ; \tag{2.2}$$

note that δB is measured in units of 'deviations of the estimator' away from the true parameter value. The estimator, after being corrected for its units, is then compared to the parameter itself, not to its own mean, thus solving both aforementioned issues.

Inserting the relationship of Eq. 2.2 into the formula for the estimator variance,

which can now be safely used, yields

$$(\Delta B_{\text{est}})^2 = \left|\frac{\partial B_{\text{est}}}{\partial B}\right|^2 \left(\langle (B - \delta B)^2\rangle - \langle B - \delta B\rangle^2\right)$$
$$= \left|\frac{\partial B_{\text{est}}}{\partial B}\right|^2 \left((\Delta B)^2 - \langle \delta B\rangle^2\right) \ . \tag{2.3}$$

Hence, the variance of the true parameter is expressed as

$$(\Delta B)^2 = \frac{(\Delta B_{\text{est}})^2}{\left|\frac{\partial B_{\text{est}}}{\partial B}\right|^2} + \langle \delta B\rangle^2 \ . \tag{2.4}$$

If $\langle \delta B\rangle \neq 0$, there is a systematic error in the measurements and $\langle B_{\text{est}}\rangle \neq B$. Conversely, if the estimator B_{est} is unbiased, Eq. 2.4 reduces to

$$(\Delta B)^2 = \frac{(\Delta B_{\text{est}})^2}{\left|\frac{\partial B_{\text{est}}}{\partial B}\right|^2} \ . \tag{2.5}$$

The quantity above can be shown to be bounded from below by

$$(\Delta B)^2 \geq \frac{1}{N\mathcal{F}(B)} \ , \tag{2.6}$$

where $\mathcal{F}(B)$ is the Fisher information of the parameter B, a measure of how much information is obtained by sampling data to infer B [9, 10]. This inequality is known as the (classical) Cramer-Rao bound, and it is sufficient to bound the sensitivity in the magnetometry protocols of interest in this thesis, which comprise a single qubit. Nevertheless, in quantum metrology applications involving entanglement and squeezing, another version of this bound, the quantum Cramer-Rao bound, is of relevance [11, 12].

For magnetometry purposes, one wishes to estimate the strength of an external magnetic field B to a very good accuracy. A natural figure of merit, which is incidentally independent of B, is the minimum resolvable field, given by the quantity ΔB above (in other words, by the standard deviation of the true parameter). The

estimator function itself is to be recognized as the temporal signal that the sensor yields, $B_{\text{est}} = \mathcal{S} \equiv \mathcal{S}(t, B)$, so that

$$\Delta B = \frac{\Delta \mathcal{S}}{\left|\frac{\partial \mathcal{S}}{\partial B}\right|} \,. \tag{2.7}$$

In order to minimize ΔB, the term $\left|\frac{\partial \mathcal{S}}{\partial B}\right|$ needs to be at a maximum; in other words, the magnetometer will be at its most sensitive where the variation of the signal with respect to the magnetic field to be measured is at its greatest.

The exact expression for the signal $\mathcal{S}(t, B)$ is a function of the controls applied to the sensor. In our case, the sensor is a qubit, and the controls will explore its (finite) quantum character in order to minimize ΔB. The loss of quantum character of the sensor is evident from the signal via a decay term with exponential shape, $\mathcal{S}(t, B) \propto e^{-\left(\frac{t}{\tau}\right)^m}$. Here, t is the interrogation time; τ a characteristic coherence time; and m a factor. Both τ and m are determined by the control protocol and by the relevant noise profile. From this, one immediately recognizes that

$$\Delta B \propto e^{+\left(\frac{t}{\tau}\right)^m} \,, \tag{2.8}$$

that is, the minimum resolvable field is proportional to a term that grows exponentially with interrogation time. Hence, it will be of utmost importance to find control protocols that both extend the characteristic decay time τ, and provide a strong scaling of the term $\left|\frac{\partial \mathcal{S}}{\partial B}\right|$ with t so as to counter the influence of the exponential term in the numerator.

Dynamical decoupling techniques [5, 6, 13] can and have been extensively used to extend coherence times; they are open-loop control sequences that correct for noise sources inducing decoherence by filtering unwanted dynamics. By exploiting memory effects in the system-bath interaction, dynamical decoupling sequences can reverse part of the quantum evolution due to noise. The original dynamical decoupling se-

quence is the Hahn spin-echo [5], which removes inhomogeneous dephasing from a free qubit evolution; many other sequences, such as the Car-Purcel-Meiboom-Gill [6] echo train acquisition, or, more recently, the Uhrig dynamical decoupling scheme [13], are, similarly to the Hahn spin-echo, pulsed schemes, in which the quantum evolution is steered by very short control pulses at regular intervals. Nevertheless, schemes for which the control fields are continuously applied also exist [14, 15], and have their roots in composite and spin-locking pulses in nuclear magnetic resonance [2]. As it will become clear in Section 2.3, the proposed magnetometry scheme will be one of continuous dynamical decoupling flavour.

We can now formally introduce the concept of sensitivity η of a magnetometer. For N measurements and a signal standard deviation $\Delta\mathcal{S}$, the sensitivity, expressed as magnetic field resolution per unit measurement time, is defined [1, 16]

$$\eta = \Delta B\sqrt{\mathcal{T}} = \frac{\Delta\mathcal{S}}{\left|\frac{\partial\mathcal{S}}{\partial B}\right|}\sqrt{Nt} \quad , \tag{2.9}$$

where the factor $\sqrt{\mathcal{T}}$, with $\mathcal{T} = Nt$ the total measurement time, associates a 'cost' with long interrogation times.

In the absence of noise (i.e., when $\tau \to \infty$), the Ramsey sequence [4] is the control for which the sensitivity attains a minimum,

$$\eta_{\mathrm{Ram}} = \frac{1}{\gamma\sqrt{t}} \, , \tag{2.10}$$

where t is the interrogation time, and γ the gyromagnetic ratio of the sensor. In the presence of noise, the Ramsey signal decoheres very fast, in a timescale known as $\tau = T_2^\star$, and the sensitivity degrades accordingly; we reinforce the fact that, in realistic experimental conditions, dynamical decoupling techniques will be advantageous as a means of preserving sensitivities for increasing interrogation times.

Finally, we anticipate the discussion of Chapter 3 and affirm that the quantum sensor that will be used for proof-of-principles experiments is a spin qubit in diamond, where signal read-out is done entirely by optical means, with very low efficiencies (see Section 3.3). Photon collection being a rare event modelled by Poisson statistics, the physical origin of the term $\Delta\mathcal{S}$ is predominantly photon shot-noise. In control schemes where read-out inefficiencies are reduced (for example, the repeated read-out methods discussed in Section 3.3), spin-projection noise, due to intrinsic quantum fluctuations, and which can also be modelled by Poisson statistics, should also be factored into $\Delta\mathcal{S}$.

2.3 Dynamics under rotary-echo sequence

In this Section, we study the dynamics of a qubit under a rotary-echo sequence, which will be used as the control protocol for magnetometry.

Consider a two-level system, $|0\rangle$ and $|1\rangle$, with resonance frequency ω_0. The qubit is excited by radiation of frequency ω with associated Rabi frequency Ω and phase modulation $\phi(t)$, such that the magnetic field amplitude is $\Omega\cos(\omega t + \phi(t))$. The Hamiltonian is then

$$\mathcal{H}_{\text{lab}} = \begin{pmatrix} 0 & \Omega\cos(\omega t + \phi(t)) \\ \Omega\cos(\omega t + \phi(t)) & \omega_0 \end{pmatrix} . \tag{2.11}$$

In a frame rotating with the excitation field, the operator

$$U_{\text{rot}} = \begin{pmatrix} 1 & 0 \\ 0 & e^{i\omega t} \end{pmatrix} \tag{2.12}$$

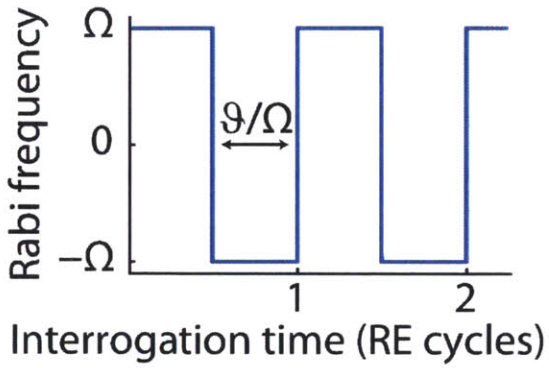

Figure 2-1: **Rotary-echo magnetometry scheme.** Experimental control sequence composed of n RE, in which the phase of the microwave field is switched by π at every pulse of duration $\frac{\theta}{\Omega}$.

transforms the Hamiltonian to

$$\mathcal{H} = U_{\text{rot}}\mathcal{H}_{\text{lab}}U_{\text{rot}}^{\dagger} - iU_{\text{rot}}\frac{dU_{\text{rot}}^{\dagger}}{dt} = \begin{pmatrix} 0 & \Omega\cos(\omega t + \phi(t))e^{-i\omega t} \\ \Omega\cos(\omega t + \phi(t))e^{i\omega t} & \omega_0 - \omega \end{pmatrix}. \tag{2.13}$$

Applying the rotating wave approximation and setting $\delta\omega \equiv \omega_0 - \omega$, the Hamiltonian reads

$$\mathcal{H} \approx \begin{pmatrix} 0 & \frac{\Omega}{2}e^{i\phi(t)} \\ \frac{\Omega}{2}e^{-i\phi(t)} & \delta\omega \end{pmatrix}. \tag{2.14}$$

One rotary-echo (RE) is composed of two identical pulses of nominal rotation angle θ applied with excitation phases shifted by π. The θ-RE (depicted in Figure 2-1) is the simplest composite pulse designed to correct for inhomogeneities in the excitation field. For $\theta \neq 2\pi k$, $k \in \mathbb{Z}$, RE does not refocus magnetic fields along the qubit quantization axes and can therefore be used for DC-magnetometry. For $\theta = 2\pi k$, RE provides superior decoupling from both dephasing [14, 15] and microwave noise and can be used to achieve AC magnetometry [17].

Under a sequence of RE, $e^{i\phi(t)} = \mathbb{SW}(t)$, with $\mathbb{SW}(t)$ the square wave of period

$T = \frac{2\theta}{\Omega}$ equal to the RE cycle time:

$$\mathbb{SW}(t) = \frac{4}{\pi} \sum_{k=1,\text{odd}}^{\infty} \frac{1}{k} \sin\left(\frac{k\pi\Omega t}{\theta}\right) . \tag{2.15}$$

On resonance ($\delta\omega = 0$) the evolution operator is trivially obtained:

$$\begin{aligned} U_0 &= \begin{pmatrix} \cos(\frac{\Omega}{2}\mathbb{TW}(t)) & -i\sin(\frac{\Omega}{2}\mathbb{TW}(t)) \\ -i\sin(\frac{\Omega}{2}\mathbb{TW}(t)) & \cos(\frac{\Omega}{2}\mathbb{TW}(t)) \end{pmatrix} \\ &= \cos\left(\frac{\Omega}{2}\mathbb{TW}(t)\right)\mathbb{1} - i\sin\left(\frac{\Omega}{2}\mathbb{TW}(t)\right)\sigma_x , \end{aligned} \tag{2.16}$$

where $\mathbb{TW}(t)$ is the triangular wave representing the integral of $\mathbb{SW}(t)$,

$$\mathbb{TW}(t) = \frac{\theta}{2\Omega} - \frac{4\theta}{\pi^2\Omega} \sum_{k=1,\text{odd}}^{\infty} \frac{1}{k^2} \cos\left(\frac{k\pi\Omega t}{\theta}\right) . \tag{2.17}$$

Using U_0 we make a transformation to the toggling frame of the microwave [18] to obtain the Hamiltonian $\tilde{\mathcal{H}}$:

$$\begin{aligned} \tilde{\mathcal{H}} &= U\mathcal{H}U^\dagger - iU\frac{dU^\dagger}{dt} = \frac{\delta\omega}{2}\begin{pmatrix} 1-\cos(\Omega\mathbb{TW}(t)) & i\sin(\Omega\mathbb{TW}(t)) \\ -i\sin(\Omega\mathbb{TW}(t)) & 1+\cos(\Omega\mathbb{TW}(t)) \end{pmatrix} \\ &= \frac{\delta\omega}{2}\left[\mathbb{1} - \cos(\Omega\mathbb{TW}(t))\sigma_z - \sin(\Omega\mathbb{TW}(t))\sigma_y\right] . \end{aligned} \tag{2.18}$$

$\tilde{\mathcal{H}}$ is periodic with T and has a strength $T\delta\omega \ll 1$, and can thus be analyzed with an average Hamiltonian expansion [19]. In order to do so, we first express the elements of $\tilde{\mathcal{H}}$ in their Fourier series:

$$\cos(\Omega\mathbb{TW}(t)) = \frac{\sin\theta}{\theta} + 2\theta\sin\theta \sum_{k=1,\text{odd}}^{\infty} \frac{(-1)^k}{\theta^2 - k^2\pi^2} \cos\left(\frac{k\pi\Omega t}{\theta}\right) ; \tag{2.19}$$

$$\sin(\Omega\mathbb{TW}(t)) = \frac{1-\cos\theta}{\theta} + 2\theta \sum_{k=1,\text{odd}}^{\infty} \frac{(-1)^k((-1)^k - \cos\theta)}{\theta^2 - k^2\pi^2} \cos\left(\frac{k\pi\Omega t}{\theta}\right) . \tag{2.20}$$

To first order then,

$$\overline{\mathcal{H}}^{(1)} = \frac{1}{T}\int_0^T \tilde{\mathcal{H}}(t')\mathrm{d}t' = \frac{\delta\omega}{\theta}\sin\left(\frac{\theta}{2}\right)\begin{pmatrix} -\cos(\theta/2) & i\sin(\theta/2) \\ -i\sin(\theta/2) & \cos(\theta/2) \end{pmatrix}$$
$$= -\frac{\delta\omega}{\theta}\sin\left(\frac{\theta}{2}\right)\left[\cos\left(\frac{\theta}{2}\right)\sigma_z - \sin\left(\frac{\theta}{2}\right)\sigma_y\right] . \tag{2.21}$$

For n rotary cycles, the propagator is approximated by $U_{RE} = e^{i\tilde{\mathcal{H}}(t)t} \approx e^{inT\overline{\mathcal{H}}^{(1)}}$. The population of a system initially prepared in $|0\rangle$, under the action of U_{RE}, is described at full echo times by the signal

$$\mathcal{S}(n) \approx \frac{1}{2}\left[1 + \cos^2\left(\frac{\theta}{2}\right) + \sin^2\left(\frac{\theta}{2}\right)\cos\left(\frac{4\delta\omega n}{\Omega}\sin\left(\frac{\theta}{2}\right)\right)\right] . \tag{2.22}$$

Extending the above approximation to include the fast Rabi-like oscillations of frequency $\frac{\pi\Omega}{(\theta \mathrm{mod} 2\pi)}$, we obtain

$$\mathcal{S}(t) \approx \frac{1}{2}\left[1 + \cos^2\left(\frac{\theta}{2}\right) + \sin^2\left(\frac{\theta}{2}\right)\cos\left(\frac{2\delta\omega t}{\theta}\sin\left(\frac{\theta}{2}\right)\right)\cos\left(\frac{\pi\Omega t}{(\theta \mathrm{mod} 2\pi)}\right)\right] , \tag{2.23}$$

indicating the presence of two spectral lines at $\frac{\pi\Omega}{(\theta \mathrm{mod} 2\pi)} \pm \frac{2\delta\omega}{\theta}\sin\left(\frac{\theta}{2}\right)$ for each existing detuning $\delta\omega$.

Numerical studies suggest the existence of further signal components arising from higher frequency components in the Fourier expansion, which are not included in the first-order approximation outlined above. Such components are $\propto \cos\left(\frac{2k\pi\Omega t}{(\theta \mathrm{mod} 2\pi)}\right)$ and $\propto \cos\left(\frac{2\delta\omega t}{\theta}\sin\left(\frac{\theta}{2}\right)\right)\cos\left(\frac{(2k+1)\pi\Omega t}{(\theta \mathrm{mod} 2\pi)}\right)$, $k \in \mathbb{Z}$, thus being linked to split pairs of spectral lines around $\frac{(2k+1)\pi\Omega t}{(\theta \mathrm{mod} 2\pi)}$, and single lines at $\frac{2k\pi\Omega t}{(\theta \mathrm{mod} 2\pi)}$.

2.4 Sensitivity under rotary-echo control sequence

Thanks to the linear dependence of the rotary-echo phase shift on $\delta\omega$, we expect a favorable scaling of the sensitivity η, which we rewrite as

$$\eta = \Delta B\sqrt{\mathcal{T}} = \frac{1}{\gamma_e}\lim_{\delta\omega\to 0}\frac{\Delta\mathcal{S}}{|\frac{\partial\mathcal{S}}{\partial\delta\omega}|}\sqrt{N(t+t_d)} \ , \tag{2.24}$$

where γ_e ($\approx 2.8\text{MHzG}^{-1}$ for the diamond sensor described in detail in Chapter 3) is the sensor gyromagnetic ratio and ΔB is the minimum detectable field. We broke down the total measurement time $\mathcal{T}$ into interrogation time t and the dead time t_d required for initialization and read-out. In the absence of relaxation, and neglecting t_d, a RE magnetometer interrogated at complete echo cycles $t = n\frac{2\theta}{\Omega}$ yields $\eta_{RE} = \frac{1}{\gamma_e\sqrt{t}}\frac{\theta}{2\sin^2(\theta/2)}$.

As shown in Figure 2-2, RE magnetometry has thus sensitivities comparable to Ramsey spectroscopy, $\eta_{\text{Ram}} \approx \frac{1}{\gamma_e\sqrt{t}}$. On the other hand, Rabi-beat magnetometry has $\eta_{\text{Rabi}} \approx \frac{\sqrt{2\Omega}}{\gamma_e}$ at large times t (see below), which makes it unsuitable for magnetometry, despite the long coherence times.

The sensitivity for rotary-echo magnetometry has its global minimum $\eta_{RE} \approx 1.38/\sqrt{t}$ (comparable to Ramsey magnetometry) for $\theta \approx \frac{3\pi}{4}$ and consecutively increasing local minima for $\theta \approx (2k+1)\pi$. A decrease in sensitivity is followed by an increase in coherence time, which can approach T_1 as in Rabi-beat magnetometry, whose sensitivity is limited by Ω, and derived in what follows.

Rabi-beat magnetometry using a single solid-state qubit was recently demonstrated [8]. The scheme presupposes the existence of an absolute frequency standard against which one wishes to resolve a nearby frequency. For magnetometry purposes then,

$$\mathcal{S} = \frac{1}{2}(\mathcal{S}_{\text{Rabi}}(\delta\omega) - \mathcal{S}_{\text{Rabi}}(0)) \ , \tag{2.25}$$

where $\delta\omega$ denotes a detuning from the frequency standard.

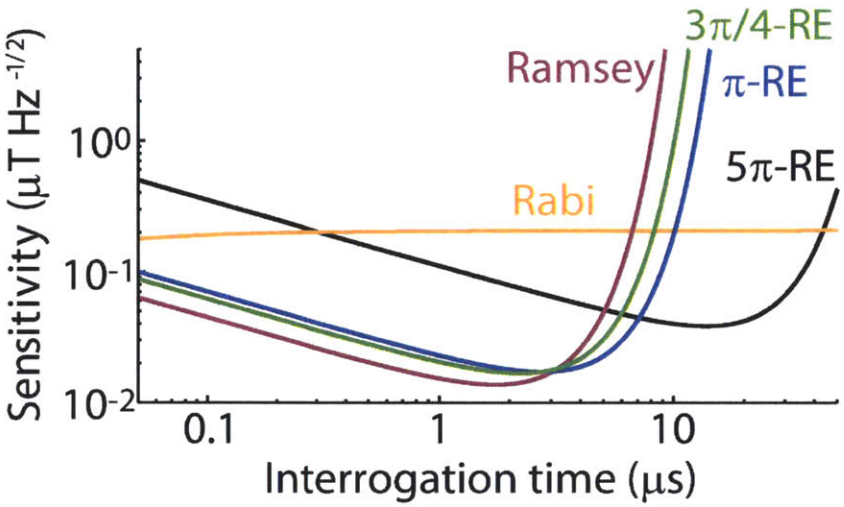

Figure 2-2: **Expected sensitivity of rotary-echo magnetometry.** Magnetometry sensitivities η_{RE} of $\theta = \{3\pi/4, \pi, 5\pi\}$-RE sequences (green, blue, black), showing the tunability with the half-echo rotation angle. For small θ, the sensitivity of rotary-echo magnetometry is comparable to Ramsey magnetometry. The sensitivity for Rabi-beat magnetometry is depicted in orange. Sensitivities are simulated in the presence of static bath noise, of strength obtained using a fit to a Ramsey experiment (depicted in Chapter 3, Figure 3-14.b).

The sensitivity reads

$$\eta = \frac{1}{\gamma_e} \lim_{\delta\omega \to 0} \frac{\Delta\mathcal{S}}{|\frac{\partial \mathcal{S}}{\partial \delta\omega}|} \sqrt{t} \approx \frac{\sqrt{2\Omega}}{\gamma_e} \sqrt{\frac{t\Omega}{2 - 2\cos(t\Omega) - t\Omega \sin(t\Omega)}} \; ; \tag{2.26}$$

η is close to minima at $t \approx (2k + \frac{3}{2})\frac{\pi}{\Omega}$, yielding

$$\eta_{min} \approx \frac{\sqrt{2\Omega}}{\gamma_e} \Big/ \sqrt{1 + \frac{2}{t\Omega}} \; , \tag{2.27}$$

which tends to $\sqrt{2\Omega}/\gamma_e$ for increasingly large interrogation times. This is a rare case of a control sequence with sensitivity η that does not scale well with increasing interrogation times; as stated and calculated previously, both Ramsey and rotary-echo sequences yield $\eta \propto \frac{1}{\sqrt{t}}$.

2.5 Evolution under bath noise

In the presence of classic Gaussian static noise in the z-direction with variance σ^2, the RE signal decays as

$$\langle \mathcal{S}_{\mathrm{RE}} \rangle = \frac{1}{2}\left[1 + \cos^2\left(\frac{\theta}{2}\right) + \sin^2\left(\frac{\theta}{2}\right)\cos\left(\frac{2\delta\omega t}{\theta}\sin\left(\frac{\theta}{2}\right)\right) e^{(t/T'_{\mathrm{RE}})^2}\right] , \tag{2.28}$$

where we define the dephasing time

$$T'_{\mathrm{RE}} = \frac{\theta}{\sigma\sqrt{2}|\sin(\theta/2)|} . \tag{2.29}$$

Similarly, one obtains for the Ramsey signal

$$\langle \mathcal{S}_{\mathrm{Ram}} \rangle = \frac{1}{2}\left(1 + \cos(\delta\omega t) e^{-(t/T'_{\mathrm{Ram}})^2}\right) , \quad \text{with} \quad T'_{\mathrm{Ram}} = T_2^{\star} = \frac{\sqrt{2}}{\sigma} . \tag{2.30}$$

Note that $T'_{\mathrm{RE}} > T'_{\mathrm{Ram}}$ always; nevertheless, at the optimum interrogation time calculated for both sequences as $\frac{T'}{2}$,

$$\frac{\eta_{\mathrm{RE}}}{\eta_{\mathrm{Ram}}} = \sqrt{\frac{\theta}{2\sin(\theta/2)^3}} > 1 ; \tag{2.31}$$

the sensitivity ratio above has a minimum $\eta_{\mathrm{RE}}/\eta_{\mathrm{Ram}} \sim 1.20$ for $\theta \sim \frac{3\pi}{4}$, which is the angle that yields the highest sensitivity for the RE sequence.

We now turn our attention to the evolution of the Rabi signal under Gaussian dephasing noise. For $\delta\omega \ll \Omega$, the Rabi signal is approximately

$$\mathcal{S}_{\mathrm{Rabi}} = 1 - \frac{\Omega^2}{\Omega^2 + \delta\omega^2}\sin^2\left(\frac{t}{2}\sqrt{\Omega^2 + \delta\omega^2}\right) \approx 1 - \left(1 - \frac{\delta\omega^2}{\Omega^2}\right)\sin^2\left(\frac{t}{2}\left(\Omega + \frac{\delta\omega^2}{\Omega}\right)\right) ; \tag{2.32}$$

calculating the expected value $\langle \mathcal{S}_{\text{Rabi}} \rangle$ under the noise distribution yields

$$\langle \mathcal{S}_{\text{Rabi}} \rangle = \frac{1}{2}\left[1 + \frac{\cos(t\Omega + \arctan(t\sigma^2/\Omega)/2)}{\left(1+\frac{t^2\sigma^4}{\Omega^2}\right)^{\frac{1}{4}}} + \frac{\sigma^2}{\Omega^2}\left(1 - \frac{\cos(t\Omega + 3\arctan(t\sigma^2/\Omega)/2)}{\left(1+\frac{t^2\sigma^4}{\Omega^2}\right)^{\frac{3}{4}}}\right)\right] . \tag{2.33}$$

In the presence of stochastic (Ornstein-Uhlenbeck) noise with zero mean and autocorrelation function $\sigma^2 e^{-\frac{t}{\tau_c}}$, a Ramsey signal decays as [20]

$$\langle \mathcal{S}_{\text{Ram}} \rangle = \frac{1}{2}\left(1 + e^{-\zeta'(t)}\right) , \quad \text{with} \quad \zeta'(t) = \sigma^2\tau_c^2(t/\tau_c + e^{-\frac{t}{\tau_c}} - 1) . \tag{2.34}$$

Numerical simulations valid for $\tau_c\sigma \lesssim \theta/2$ and $\tau_c \gtrsim \theta/(2\Omega)$ indicate that the RE signal decays as

$$\langle \mathcal{S}_{\text{RE}} \rangle = \frac{1}{2}\left[1 + \cos^2\left(\frac{\theta}{2}\right) + \sin^2\left(\frac{\theta}{2}\right) e^{-\zeta(t)}\right] , \tag{2.35}$$

with

$$\zeta(t) = \zeta'(t)\frac{4\sin^2(\theta/2)}{\theta^2} . \tag{2.36}$$

Note the additional factor $\frac{4\sin^2(\theta/2)}{\theta^2} = \left(\frac{T'_{\text{Ram}}}{T'_{\text{RE}}}\right)^2 < 1$.

A comparison of different θ-RE signals for $\theta = \{3\pi/4, \pi, 5\pi\}$ and Ramsey signals in the presence of stochastic bath noise are depicted in Figure 2-3. Numerical simulations agree with the derived formulas. The Ramsey sequence is the least resilient to bath noise, whereas one can adjust the dephasing of the RE by the choice of θ; RE sequences are more resilient to bath noise for longer θ. The used numerical parameters are: $\Omega = 2\pi \times 20\text{MHz}$, $\delta\omega = 2\pi \times 2\text{MHz}$, $\tau_c = 200\text{ns}$, $\sigma = 0.05\Omega$.

Previous calculations [21] indicate that, for slow baths $\frac{1}{\tau_c} \ll \frac{\sigma^2}{\Omega}$, the Rabi signal follows the static noise behaviour for short times, and decays $\propto e^{-\frac{\sigma t}{2\sqrt{\tau_c\Omega}}}$ for long times. Fast baths $\frac{1}{\tau_c} \gg \frac{\sigma^2}{\Omega}$ induce a decay of the Rabi signal $\propto e^{\frac{4\Omega^2}{\sigma^4\tau_c}}$.

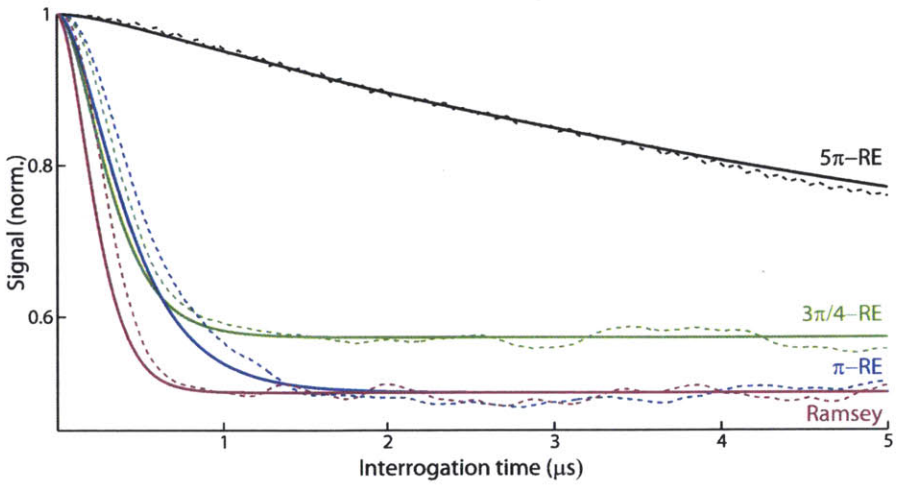

Figure 2-3: **Rotary-echo signal decay in the presence of stochastic noise along σ_z.** Analytical solutions for the decay of different θ-RE signals, with $\theta = \{3\pi/4, \pi, 5\pi\}$ (solid lines in green, blue, black), are compared against a the decay of a Ramsey sequence (purple). Numerical simulations are plotted in dashed lines, and agree with the analytical formulas. RE sequences are more resilient to bath noise for longer θ.

2.6 Evolution under noise in the excitation field

In the presence of a constant error in the Rabi frequency such that $\Omega \to (1+\epsilon)\Omega$, the infidelity $(1 - \mathrm{Tr}[U(\epsilon)U(0)]/2) \equiv (1-F)$ of the pulse sequence is given to second order in the detuning from resonance $\delta\omega$ and in ϵ by

$$(1-F)_{\mathrm{RE}} \approx \frac{\epsilon^2 t^2 \delta\omega^2}{8} \frac{(2+\theta^2-2\cos\theta-2\theta\sin\theta)}{\theta^2} \tag{2.37}$$

for RE and

$$(1-F)_{\mathrm{Rabi}} \approx \frac{\epsilon^2 t^2 \Omega^2}{8} - \frac{\epsilon^2 \delta\omega^2(-2+t^2\Omega^2+2\cos(t\Omega))}{8\Omega^2} \tag{2.38}$$

for Rabi-beat magnetometry.

Similarly, an error in the Rabi frequency will yield a flip-angle error in the Ramsey

sequence, resulting in the infidelity

$$(1-F)_{\text{Ram}} \approx \frac{\epsilon^2\pi^2}{8} - \frac{\epsilon^2\delta\omega^2(-16+4\pi^2+\pi t\Omega(8+\pi t\Omega))}{32\Omega^2} \ . \tag{2.39}$$

In the presence of stochastic noise in the excitation field with zero mean and autocorrelation function $\sigma^2 e^{-\frac{t}{\tau_c}}$, the resonant cases for RE, Rabi have simple analytical solutions.

A cumulant expansion technique applied to periodic Hamiltonians [20, 22] yields for the envelope of a resonant RE sequence

$$\langle \mathcal{S}_{\text{RE}} \rangle = \frac{1}{2}\left(1+e^{-\zeta(n)}\right) \ , \tag{2.40}$$

with

$$\zeta(n) = \tau_c^2\sigma^2\left[\frac{2n\theta}{\sigma\tau_c} + 2n(e^{-\frac{\theta}{\Omega\tau_c}}-1) - \tanh^2\left(\frac{1}{2}\frac{\theta}{\Omega\tau_c}\right)\left(2n(e^{-\frac{\theta}{\Omega\tau_c}}+1)+e^{-\frac{2n\theta}{\tau_c\sigma}}-1\right)\right] . \tag{2.41}$$

We note that this decay is equivalent to the decay under pure dephasing for a PDD sequence [23].

In Figure 2-4, we simulate the signal for different θ-RE and Rabi sequences if noise in the excitation field is present. As shown experimentally in Chapter 3, RE sequences can refocus excitation noise with correlation times longer than the echo period.

We note that the Rabi signal decay for noise along σ_x should be comparable to Ramsey signal decay in the presence of stochastic noise along σ_z. We thus have the decay

$$\langle \mathcal{S}_{Rabi} \rangle = \frac{1}{2}\left(1+e^{-\zeta'(t)}\right) \ , \quad \text{with} \quad \zeta'(t) = \sigma^2\tau_c^2(t/\tau_c + e^{-\frac{t}{\tau_c}} - 1) \ . \tag{2.42}$$

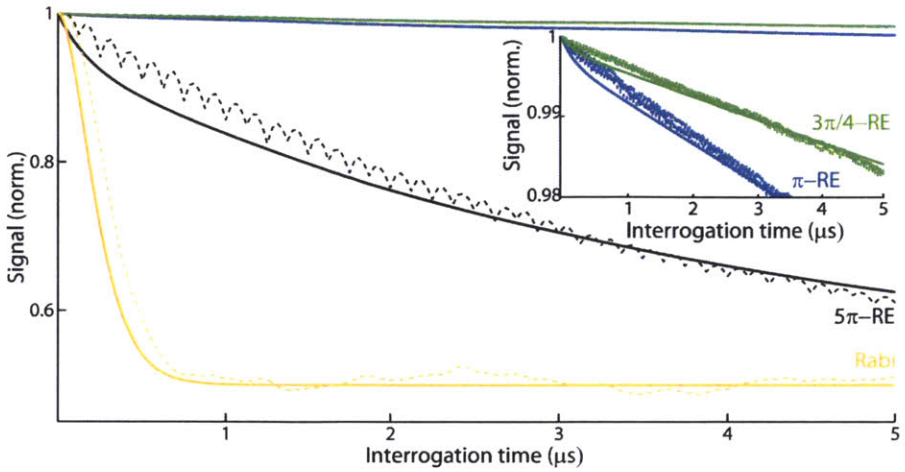

Figure 2-4: **Rotary-echo signal decay in the presence of stochastic noise along σ_x.** In the presence of stochastic noise in the excitation field, RE sequences refocus microwave noise with correlation times longer than the echo period; the decay of the Rabi sequence (orange) is plotted for comparison. Used parameters are the same as in Figure 2-3, except for $\delta\omega = 0$.

The advantage of the RE sequence over the Rabi is thus the same advantage that dynamical decoupling sequences can offer for dephasing noise.

2.7 Conclusion

We have both analytically and numerically demonstrated that, under a θ-RE magnetometry protocol, effects of experimentally relevant noise profiles can be mitigated by a careful choice of the rotation angle θ. Moreover, fixed θ, ensuing sensitivities range from those of the golden standard of Ramsey spectroscopy, to those of Rabi spectroscopy.

Our protocol is, thus, useful in experimental settings with unpredictable or variable environments; and, more generally, benefits experimental runs with especially long dead-times.

In the next chapter, we experimentally implement composite-pulse magnetometry using a solid-state qubit in diamond.

Chapter 3

Composite-pulse magnetometry: experiment

The field of nanoscale metrology, or, in particular, magnetometry, is concerned with measuring tiny signals arising, oftentimes, from quantum objects. In this sense, it is clear that the required precision will only be met by quantum sensors, which either operate under quantum control protocols [4], or whose quantum properties such as spin squeezing and entanglement offer increased sensitivities [11, 12].

Solid-state quantum sensors attract much attention given their combined potential for high sensitivity, tailored engineering and, importantly, scalability. In particular, the electronic spin of the nitrogen-vacancy color center in diamond [24] is a robust quantum sensor due to a combination of highly desirable properties: optical initialization, read-out via stable fluorescence, long coherence times at room temperature ($T_1 > 2$ ms [25, 26], $T_2 \gtrsim 0.5$ms [27]), the potential to harness the surrounding spin bath for memory and sensitivity enhancement [28, 29], and bio-compatibility [30].

In a room-temperature implementation based on a single electronic spin in diamond [31, 32], throughout this Chapter we study the composite-pulse magnetometry protocol developed in Chapter 2, and confirm that it yields a tunable trade-off between sensitivities in the $\mu\text{THz}^{-\frac{1}{2}}$ range, comparable to those obtained with Ramsey

spectroscopy [32], and coherence times approaching the spin-lattice relaxation time T_1 of Rabi-beat spectroscopy [8].

We conclude by proposing a realistic application to magnetic sensing at the nanoscale, and in variable environments, such as in distinct calcium signalling domains in cells, or in samples whose noise characterization is required.

3.1 Experimental description

In this section, the solid-state electronic qubit employed in the experiments, as well as the experimental setup, are described in detail.

3.1.1 Physical system

The nitrogen-vacancy center is a naturally occurring color defect in diamond [24], composed of a vacancy adjacent to a substitutional nitrogen in the carbon lattice, as depicted in Figure 3-1. It can exist in two charge states: the neutral defect, noted NV^0, and the defect with an additional electron, noted NV^-, which have differing energy structures and dynamics [33]. For nanosensing purposes, of relevance is the negatively charged nitrogen-vacancy center (henceforth simply referred to as 'NV' for simplicity), for reasons that will become clear in what follows.

The ground state of the NV center is a spin-triplet with zero-field splitting $\Delta =$ 2.87GHz between the $m_s = |0\rangle$ and $m_s = |\pm 1\rangle$ sub-levels [34, 35], where we denote m_s the spin projection along the defect quantization axis linking the vacancy and the nitrogen. Coherent optical excitation, for example at 532nm, promotes the quantum state of the defect non-resonantly to the first orbital excited state, also a spin triplet, and not resolvable at room-temperature. While the $m_s = |0\rangle$ state mostly relaxes via phonon-mediated fluorescent emission (zero-phonon line at 637nm; broadband

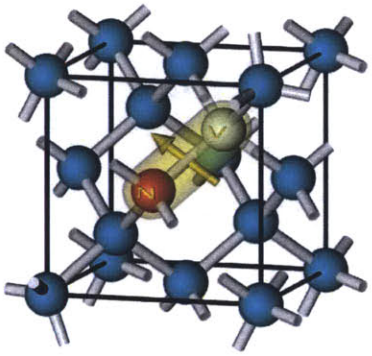

Figure 3-1: **Structure of the nitrogen-vacancy center in diamond.** The nitrogen-vacancy center in diamond, a naturally occurring color center defect, arises when a vacancy in the lattice is adjacent to a nitrogen impurity. The defect quantization axis joins the nitrogen and the vacancy.

emission at room temperature at $\approx 650-800$nm), the $m_s = |\pm 1\rangle$ states have in addition an alternative, slower, non-radiative decay mode mostly to the $m_s = |0\rangle$ via metastable singlet states; the competing relaxation processes are shown in Figure 3-2. Due to this property, the quantum state $m_s = |0\rangle$ is distinguishable from $|\pm 1\rangle$ by monitoring the intensity of emitted photons during a short pulse of optical excitation. Additionally, continuous optical excitation polarizes the NV into the $m_s = |0\rangle$ state. Thus, the NV can be initalized and read-out by optical means.

Even a small magnetic field can lift the degeneracy of the $|\pm 1\rangle$ ground states. The quantum state $|0\rangle$ and either $|+1\rangle$ or $|-1\rangle$ can then be singled out as an effective qubit, and coherently addressed by microwaves.

A 7-level semi-classical rate equation, for levels depicted in Figure 3-3, models the NV center dynamics in a simplified way. In the density matrix formalism, it reads

$$\dot{\rho}_{ij} = -\frac{i}{\hbar}\left[\mathcal{H}, \rho\right]_{ij} - \Gamma_{ij}\rho_{ij} + \delta_{ij}\sum_r \gamma_{ir}\rho_{rr} \ . \tag{3.1}$$

Here, $\mathcal{H}$ is the full Hamiltonian describing the interaction of the nitrogen-vacancy center with the initialization and read-out laser, and with the microwaves that drive

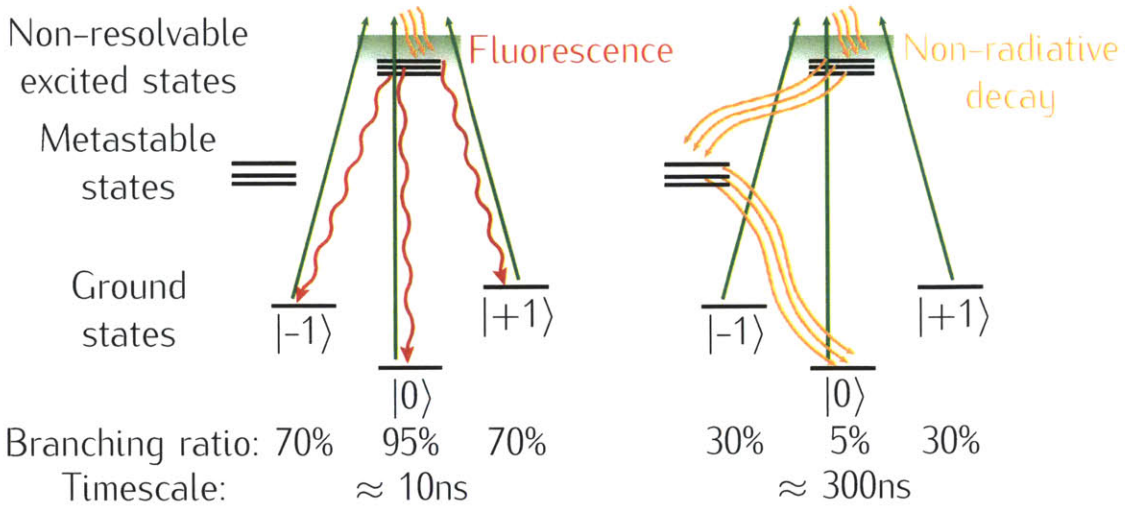

Figure 3-2: **Competing relaxation paths in nitrogen-vacancy centers in diamond.** The fluorescence of the defect is spin-dependent in that two competing processes, namely a fast fluorescence decay and a slower non-radiative decay, create an effective time window during which the quantum state of the defect can be distinguished by average fluorescence levels. At room temperature, the excited state manifold levels cannot be resolved.

coherent transitions between levels; the Γ_{ij} represent the decay rates of the matrix elements; and γ_{ij} the population 'feeding' terms, i.e. γ_{ij} is the rate with which the j^{th} level decays into the i^{th} level. The parameters obey

$$\Gamma_{jj} = \sum_i \gamma_{ij} \ ; \tag{3.2}$$

$$\Gamma_{ij} = \frac{1}{2}\left(\Gamma_{ii} + \Gamma_{jj}\right) \ . \tag{3.3}$$

A simplified picture, sufficient to model for example the read-out and adiabatic passage processes described in Subsection 3.1.2, is obtained by describing the effect of the read-out laser as a rate that populates (depopulates) the excited (ground) states.

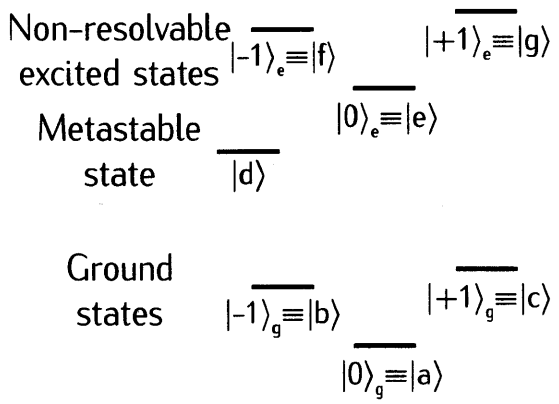

Figure 3-3: **Relevant nitrogen-vacancy levels for semi-classical rate equation.** The dynamics of a NV center interacting with photons for initialization, control and read-out can be modelled with a 7-level semi-classical rate equation. The metastable state $|d\rangle$ in the model accounts for the existence of at least two real metastable states in between the ground and excited state manifolds.

In this case, the appropriate parameters are [36]:

$$\gamma_{bf} = \gamma_{ae} = \gamma_{cg} \approx 77\text{MHz} \; ; \tag{3.4}$$

$$\gamma_{be} = \gamma_{ce} = \gamma_{af} = \gamma_{ag} \approx 1.5\text{MHz} \; ; \tag{3.5}$$

$$\gamma_{dg} = \gamma_{df} \approx 30\text{MHz} \; ; \tag{3.6}$$

$$\gamma_{ad} \approx 3.3\text{MHz} \; ; \tag{3.7}$$

$$\gamma_{be} = \gamma_{ce} = \gamma_{af} = \gamma_{ag} \approx 1.5\text{MHz} \; ; \tag{3.8}$$

$$\gamma_{fb} = \gamma_{ea} = \gamma_{gc} \approx I_0 \cdot 77\text{MHz} \; ; \tag{3.9}$$

in the laser rates, $I_0 \sim 1$ is a saturation parameter; all other rates are approximately zero.

We plot in Figs. 3-4, 3-5 typical simulations obtained using the rate equations above. They model population evolution during read-out and expected integrated number of emitted photons per time.

The coherence time of the NV spin is limited by dipolar interactions with a bath of

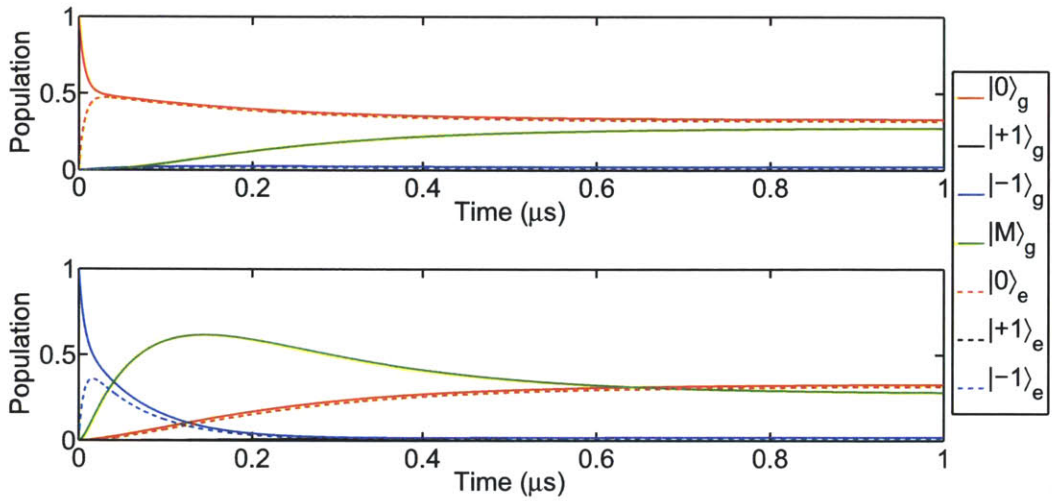

Figure 3-4: **Population evolution during read-out.** The dynamics of the populations in the 7 relevant levels for the NV center system during read-out are modelled by the rate equations. Top-most panel, case for the NV center starting in $|0\rangle_g$; lower-most panel, case for the NV center starting in $|-1\rangle_g$.

spins within the diamond lattice; in particular, with neutral and 'dark' substitutional nitrogen atoms in the diamond lattice (also called 'P1' or 'C' centers, with electronic spin $\frac{1}{2}$) [37]; and with ^{13}C nuclear spins, which exist in a natural abundance of 1.1%. Materials research efforts have been underway to produce diamond samples that are virtually spuriouos spin-free [38].

3.1.2 Apparatus

Experiments were run at room-temperature with single NV centers from an electronic grade single crystal plate ([100] orientation, Element 6) with a substitutional nitrogen concentration < 5 ppb. We apply a magnetic field ($\approx$ 100G) along a crystal axis $\langle 111 \rangle$ to lift the degeneracy between the $m_s = |\pm 1\rangle$ states and drive an effective two-level system $m_s = \{|0\rangle, |1\rangle\}$ at the resonant frequency ($\omega_0 \approx 3.15$GHz) obtained by continuous wave electron spin resonance [24, 39] and Ramsey fringe experiments [4].

A modest static magnetic field $B_{\|} \approx$ 100G is applied by a permanent magnet

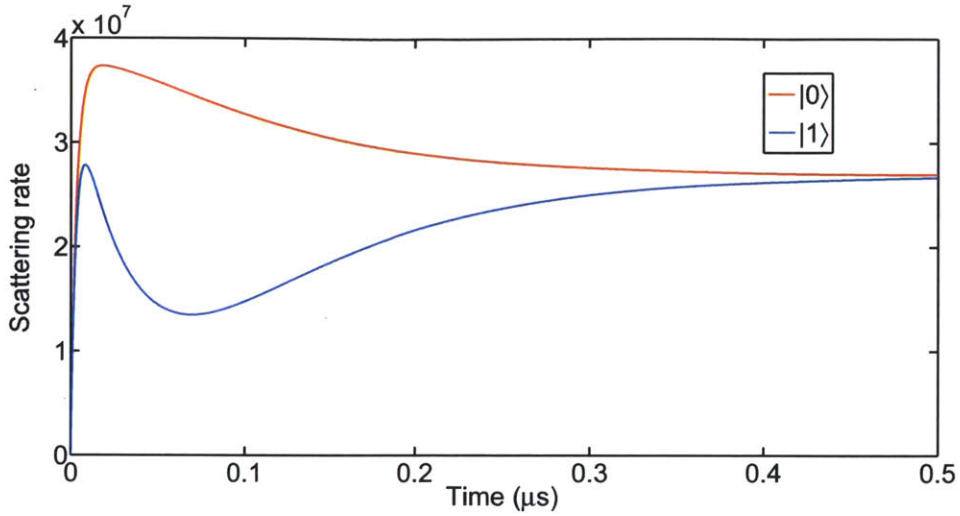

Figure 3-5: **Fluorescence rate during read-out.** Using the rate equations, the scattering rate of the NV center can be predicted, contingent upon the state of the defect.

(BX0X0X0-N52, K&J Magnetics) mounted on a rotation stage, which in turn is attached to a three-axis translation stage; this arrangement enables the adjustment of the magnetic field angle with respect to the sample. The magnetic field is aligned along a [111] axis by maximizing the Zeeman splitting in a continuous-wave electron spin resonance spectrum.

The fluorescence of single NV centers is identified by a home-built confocal scanning microscope, depicted in Figure 3-6. The sample is mounted on a piezo stage (Nano-3D200, Mad City Labs). The excitation at 532nm is provided by a diode-pumped laser (Coherent Compass 315M), and fluorescence in the phonon sideband ($\sim$ 650 $-$ 800nm) is collected by a 100x, NA = 1.3 oil immersion objective (Nikon Plan Fluor). The fluorescence photons are collected into a single-mode broadband fiber of NA = 0.12 (Font Canada) and sent to a single-photon counting module (SPCM-AQRH-13-FC, Perkin Elmer) with acquisition time 100 or 200 ns.

In each experimental run, we normalize the signal with respect to the reference counts from the $m_s = \{|0\rangle, |1\rangle\}$ states, where the transfer to state $m_s = |1\rangle$ is done

by adiabatic passage [40, 41]. The spin flipping rate after passage time Δt is given by $e^{-\frac{\Delta t}{\tau}}$, with

$$\tau = \frac{\Delta f}{2\pi\Omega^2} , \tag{3.10}$$

Δf being the passage frequency range, and Ω the experimental Rabi frequency in Hz. Given typical experimental Rabi frequencies $\sim 10-20$MHz, we induce a spin-flip from a prepared $|0\rangle$ state into states $|\pm 1\rangle$ with $\Delta t \approx 600$ns and $\Delta f \approx 200$MHz. Typical contrast-to-noise ratios are $\sim 3-4$.

Laser pulses for polarization and detection are generated by an acousto-optic modulator with rise time $\lesssim 7$ns (1250C-848, Isomet). A signal generator (N5183A-520, Agilent) provides microwave fields to coherently manipulate the qubit. An arbitrary waveform generator at 1.2GS/s (AWG5014B, Tektronix) is employed to shape microwave pulses with the help of an I/Q mixer (IQ-0318L, Marki Microwave), and to time the whole experimental sequence. Microwaves are then amplified (GT-1000A, Gigatronics) and subsequently delivered to the sample by a copper microstrip mounted on a printed circuit board, fabricated in MACOR to reduce losses. Alternatively, microwaves can be delivered by a copper wire 0.025mm thick (Alfa Aeser 10970, Puratronics).

Schematics of the optical and electronics setups are found, respectively, in Figures 3-6 and 3-7.

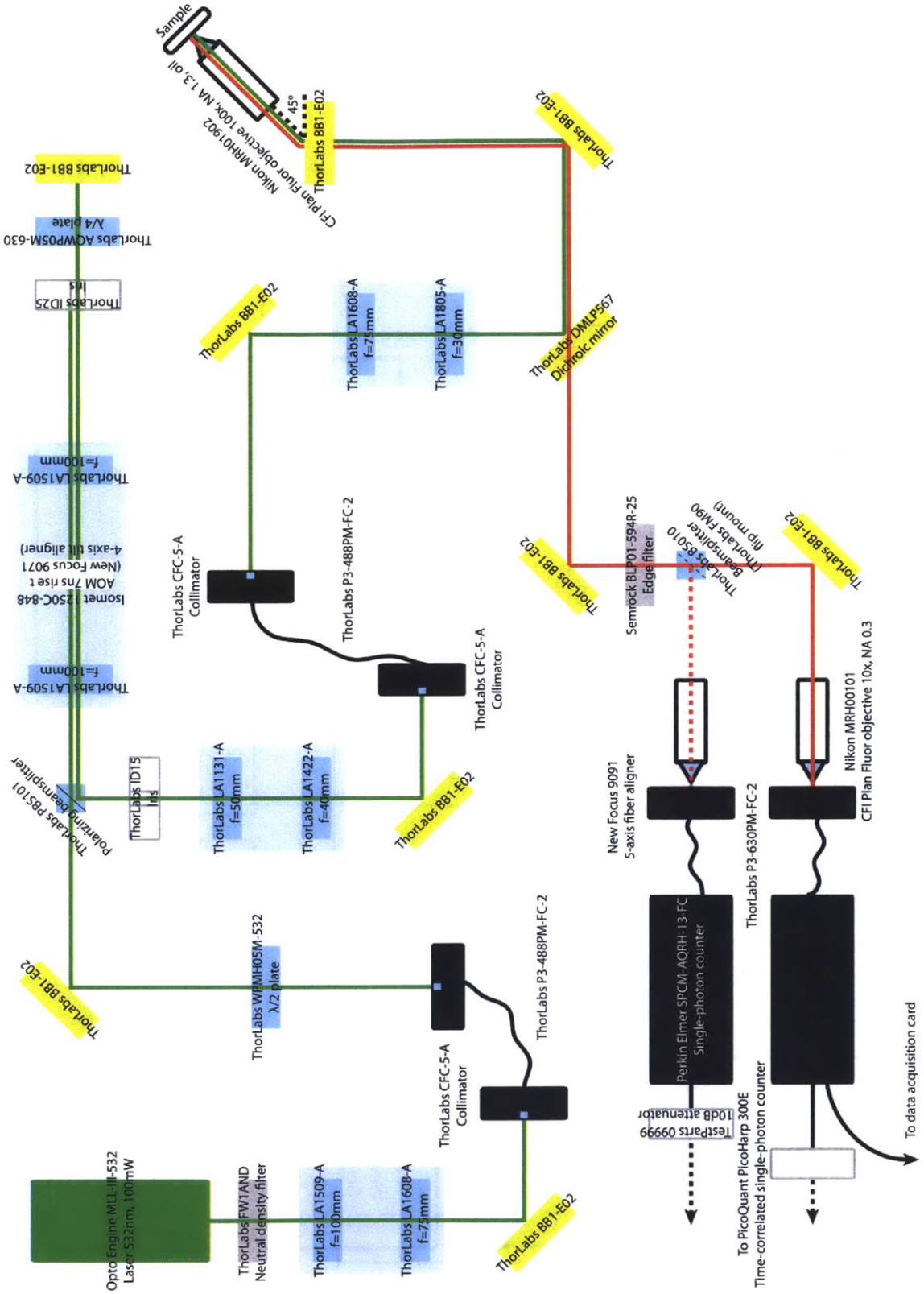

Figure 3-6: **Schematics of optical setup.** Home-built confocal microscopy setup to detect and control nitrogen-vacancy centers in diamond.

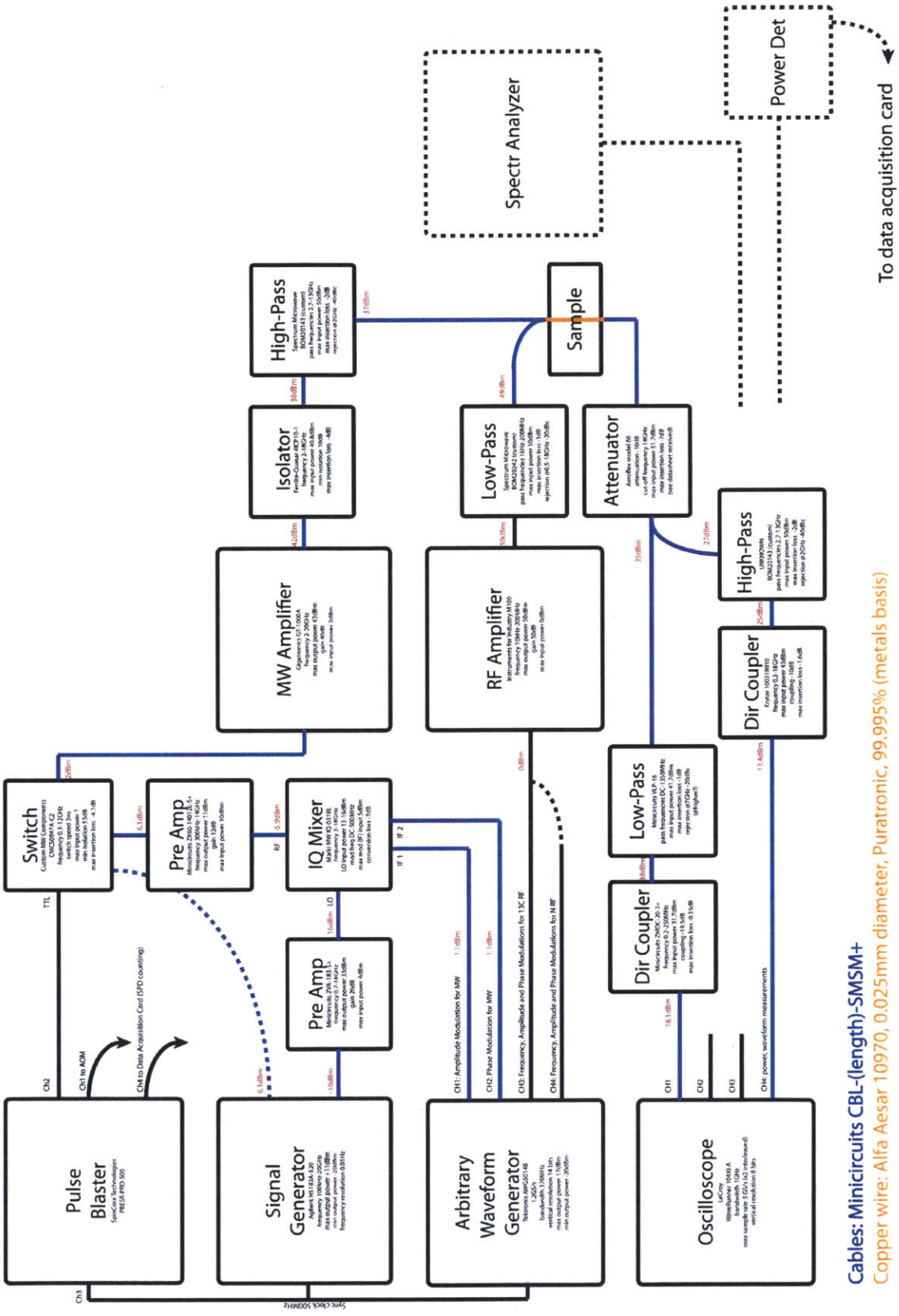

Figure 3-7: **Schematics of electronics setup.** Electronics setup to control nitrogen-vacancy centers in diamond.

3.2 Rotary-echo signal and frequency content

To establish the sensitivity limits of rotary-echo (RE) magnetometry and compare them to other DC-magnetometry strategies, we carried out proof-of-principle experiments in single NV centers using the experimental apparatus described above.

The qubit is coupled to the spin-1 ^{14}N nucleus that composes the defect by an isotropic hyperfine interaction of strength $A \approx 2\pi \times 2.17$MHz. After optical polarization into state $|0\rangle$, we apply a stream of n RE cycles using microwaves with frequency ω close to the qubit resonance $\omega_0 = \Delta + \gamma_e B_\parallel$, where $\Delta = 2.87$GHz is the NV zero-field splitting. Because of the hyperfine coupling, ω_0 is the resonant frequency only when the nuclear state is $m_I = 0$. At room temperature, the nitrogen nucleus is unpolarized and, while its state does not change over one experimental run, in the course of the $N \sim 10^6$ experimental realizations, $\approx 2/3$ of the times the qubit is off-resonantly driven by $|\delta\omega| = A$.

A typical n-cycle RE fluorescence signal is plotted in Figure 3-8 for $\theta = \pi$ and $\Omega \approx 2\pi \times 17$MHz. Here, $n = 55$. the modulation in the signal is due to the hyperfine interaction with the ^{14}N nucleus. The signal is filtered for even harmonics of $\pi\Omega/(\theta \mathrm{mod} 2\pi)$ and then fitted to Eq. 2.23 modified to include decoherence induced by static bath noise (of strength inferred from the Ramsey experiment of Figure 3-14.b).

In order to determine the frequency content of the signal we plot the periodogram in Figure 3-9. The periodogram is defined as the squared magnitude of the Fourier transform of the signal $\mathcal{S}(t)$ at times t_j $(j = 1, \ldots, M)$, $\mathcal{P} \equiv \frac{1}{M} |\sum_{j=1}^{M} d_j e^{i\omega t_j}|^2$, where d_j are the M data points [42].

Unlike the Fourier Transform, the periodogram does provide bounds for frequency estimation from spectral analysis, besides being able to accommodate for noise profiles beyond static and white noise [42]. Take a simple sinusoidal signal $d_t = K \cos(2\pi f t) +$

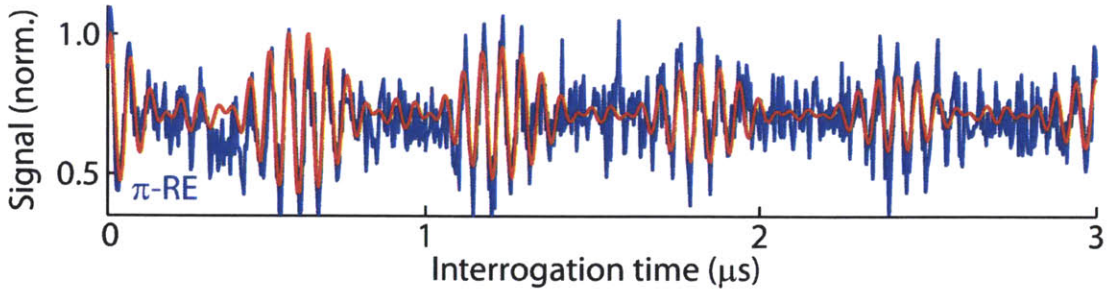

Figure 3-8: **Typical rotary-echo signal.** A typical $n = 55$ cycles RE normalized fluorescence for $\theta = \pi$ and $\Omega \approx 2\pi \times 17$MHz (blue); the modulation in the signal is due to the hyperfine interaction with the ^{14}N nucleus. The signal is filtered for even harmonics of $\frac{\pi\Omega}{(\theta \mathrm{mod} 2\pi)}$ (see discussion in Chapter 2) and then fitted to Eq. 2.23, modified to include decoherence induced by static bath noise (red).

e_t, where e_t is the added noise characterized by a (least informative) Gaussian probability distribution Normal$(0,\sigma^2)$, with σ in circular frequency units. To σ is assigned Jeffrey's prior $\frac{1}{\sigma}$, which indicates complete ignorance of this scale parameter. Under these conditions, the estimate frequency content of the signal is given by $f_{est} = f_{peak} \pm \delta f$, where f_{peak} is the frequency of the periodogram peak, and

$$\delta f = \frac{2\sqrt{3}}{\pi} \frac{\sigma}{Kt\sqrt{M}} \,. \tag{3.11}$$

Here t is the total interrogation time for the M data points. δf correctly takes into account the effect of both the interrogation duration t and the $S/N \equiv \frac{K_{\mathrm{RMS}}}{\sigma} = \frac{K}{\sqrt{2}\sigma}$, and is shown to correspond to the classical Cramer-Rao bound [43]. Note that δf is in general smaller than the so-called Fourier limit, $\delta f_{Fl} = \frac{1}{2t}$. The method is readily applicable to signals with multiple frequency content $\{f_i\}$.

A pair of symmetric peaks about Ω signals the existence of one detuning $\delta\omega$. The number of resolved frequencies increases with time, at the expense of signal-to-noise ratio. After 5μs of interrogation, we can estimate both the hyperfine interaction $A \approx 2\pi \times (2.14 \pm 0.03)$MHz and a small residual detuning from the presumed resonance, $b \approx 2\pi \times (0.17 \pm 0.02)$MHz. In this estimate, we correct for the real rotation angle $\theta \approx 0.96\pi$ using the difference between the nominal and experimentally realized

Rabi frequency (symmetry point in the spectrum). The uncertainty in the measurement is estimated taking into account the total interrogation time, the number of points in the time-domain signal, and the S/N.

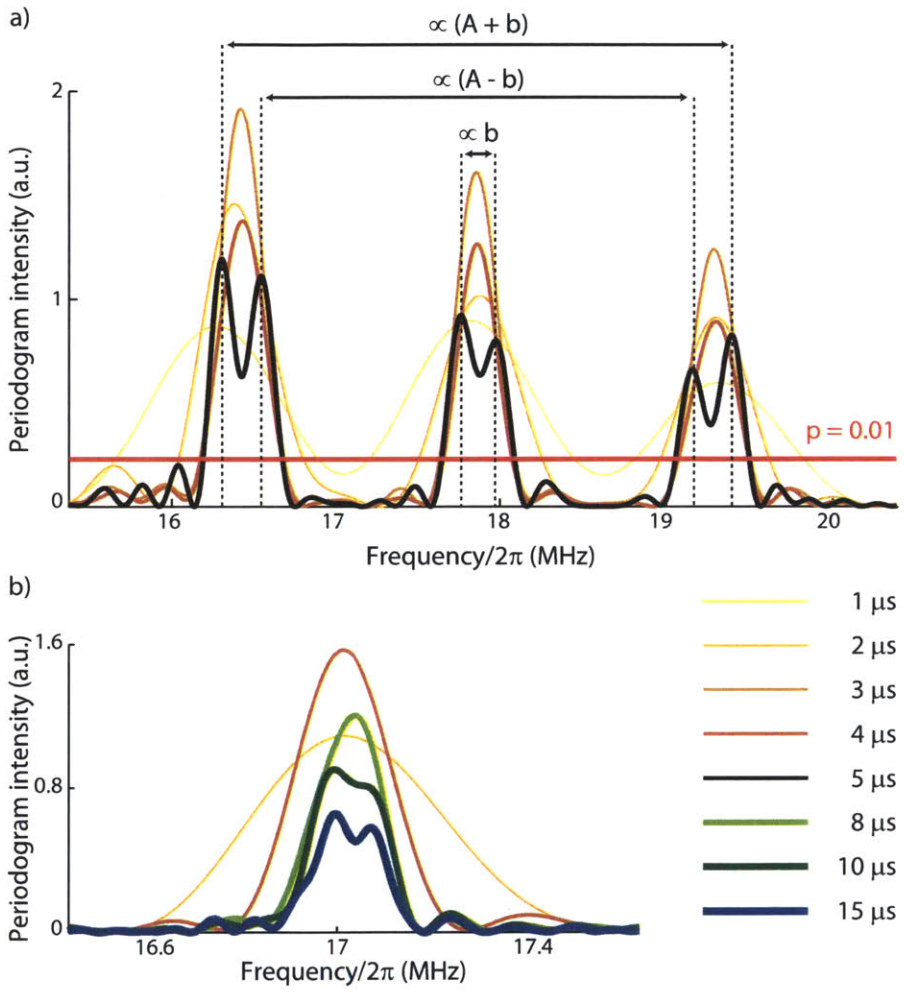

Figure 3-9: **The periodogram and the frequency content of the rotary-echo signal.** a) Periodogram for π-RE sequence for increasing interrogation times (thicker lines). The periodogram is defined as the squared magnitude of the Fourier transform of the time signal. b) Innermost pair of frequency peaks arising from a $b \approx 2\pi\times(64\pm 12)$kHz residual detuning in another experimental realization, for an interrogation time of 15μs.

Periodogram peaks can be tested for their statistical significance [44]. Letting I_m be the intensity of m-th largest ordinate among the total M in the periodogram, and

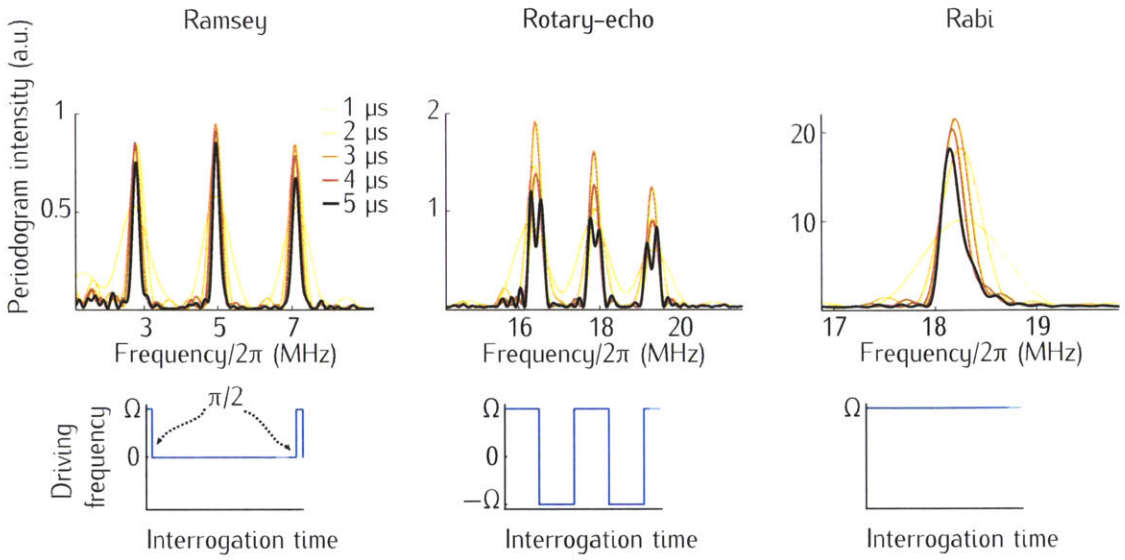

Figure 3-10: **Experimental periodograms for increasing interrogation times, for Rabi, Ramsey and rotary-echo sequences.** a) Ramsey (5MHz detuned from the presumed resonance), b) π-RE and c) Rabi sequences. There is a trade-off between signal intensity and sensitivity to the detunings $\{b, A \pm b\}$ in the signal.

calculating

$$T_m = \frac{I_m}{\sum_k I_k - \sum_{l=1}^{m} I_l} \ , \tag{3.12}$$

the statistical significance of the m-th peak p_m is approximated by

$$p_m \approx (M - (m-1))(1 - T_m)^{M-m} \ . \tag{3.13}$$

We confirm that all 6 frequency peaks are considerably more significant than a $p = 0.01$ significance level. At its turn, to determine δf, we first estimate the S/N for each periodogram peak by dividing the peak area by the noise floor below the line of $p = 0.01$.

The number of distinguishable frequencies increases with interrogation time, at the expense of signal-to-noise ratio. Not only can we observe the frequency shifts due to a measured hyperfine interaction $A \approx 2\pi \times (2.14 \pm 0.03)$MHz but, for interrogation times as short as 5μs, RE-magnetometry detects a small residual detuning $b \approx 2\pi \times (0.17 \pm 0.02)$MHz from the presumed resonance. In contrast, Rabi magne-

tometry would not show such a detuning under the same experimental conditions before an interrogation time $\approx 188\mu$s. With longer interrogation times $\sim 15\mu$s as in Figure 3-9.b, we can detect a detuning from the nominal resonance as small as $b \approx 2\pi \times (64 \pm 12)$ kHz.

In Figure 3-10, we compare typical experimental periodograms for π-RE, Ramsey and Rabi signals taken under the same conditions, for increasing interrogation times. The Ramsey periodogram, despite its lower signal intensity, clearly shows the 3 detunings $\{b + 2\pi \times 5\text{MHz}, A \pm (b + 2\pi \times 5\text{MHz})\}$ present in the signal after 1μs; π-RE is sensitive to the residual detuning $b \sim 2\pi \times 0.17$MHz after 5μs; finally, the Rabi sequence would only become sensitive to b after an interrogation time $\sim 188\mu$s, which is reflected in the broad single peak of the periodogram.

The periodogram for the RE sequence, if plotted over the full spectrum as in Figure 3-11, exhibits very high peaks corresponding to the even harmonics of Ω which are present in the signal, but which are not taken into account by the first order of average Hamiltonian theory. In the inset, the peak structure originated from the detunings of interest is plotted for times much longer than the dephasing time T'_{RE}. Under these conditions, it is not well-understood why the peaks do not branch out evenly in the presence of a small detuning. Additionally, it is not clear why pairs of peaks caused by the same detuning from resonance may appear in the periodogram with different intensities.

3.3 Experimental sensitivity

To determine the experimental sensitivities of RE magnetometry, we estimate $|\frac{\partial \mathcal{S}}{\partial \delta\omega}|$ by driving the qubit with varying ω, at fixed interrogation times; the results for $\theta = \pi$ are plotted in Figure 3-12. For each interrogation time, in Figure 3-13 we plot the minimum $\frac{1}{\gamma_e} \frac{\Delta \mathcal{S}}{|\frac{\partial \mathcal{S}}{\partial \delta\omega}|} \sqrt{Nt}$ and compare it to the adjusted theoretical sensitivity

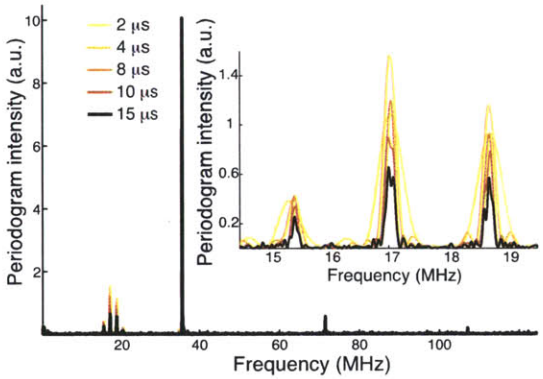

Figure 3-11: **Periodogram for rotary-echo signal over the full spectrum.** Frequencies corresponding to the even harmonics of Ω which are present in the signal, but which are not contemplated by the first order of average Hamiltonian theory, can be clearly identified. In the inset, the signal peaks arising from the frequencies of interest are shown for interrogation times much longer than the dephasing time T'_{RE}.

$\eta/(C \times C_A)$. Here $(C \times C_A)$, $\approx (5.9 \pm 1.4) \times 10^{-3}$ in our setup, is a factor taking into account read-out inefficiencies and a correction for the presence of the hyperfine interaction [1].

The reported sensitivities agree with the theoretical model, with minimum sensitivity $\sim 10\mu\mathrm{THz}^{-\frac{1}{2}}$. Improved sensitivities are expected with the use of isotopically pure diamond [38] for the increased coherence times; the correction factor C_A (respectively, C) can approach 1 upon polarization of the nuclear spin and adequate choice of interrogation times (upon the use of repeated read-out methods [45]).

In the following we describe the experimental procedure and data analysis used to determine the experimental sensitivity.

For a fixed interrogation time t, and scanning the detuning from resonance $\delta\omega$, we expect to observe the signal

$$\mathcal{S}(\delta\omega) \propto \cos\left(\frac{2\delta\omega t}{\theta}\sin\left(\frac{\theta}{2}\right)\right) \equiv \cos\left(\delta\omega\tau\right) \ , \tag{3.14}$$

with $\tau = \frac{2t}{\theta}\sin\left(\frac{\theta}{2}\right)$.

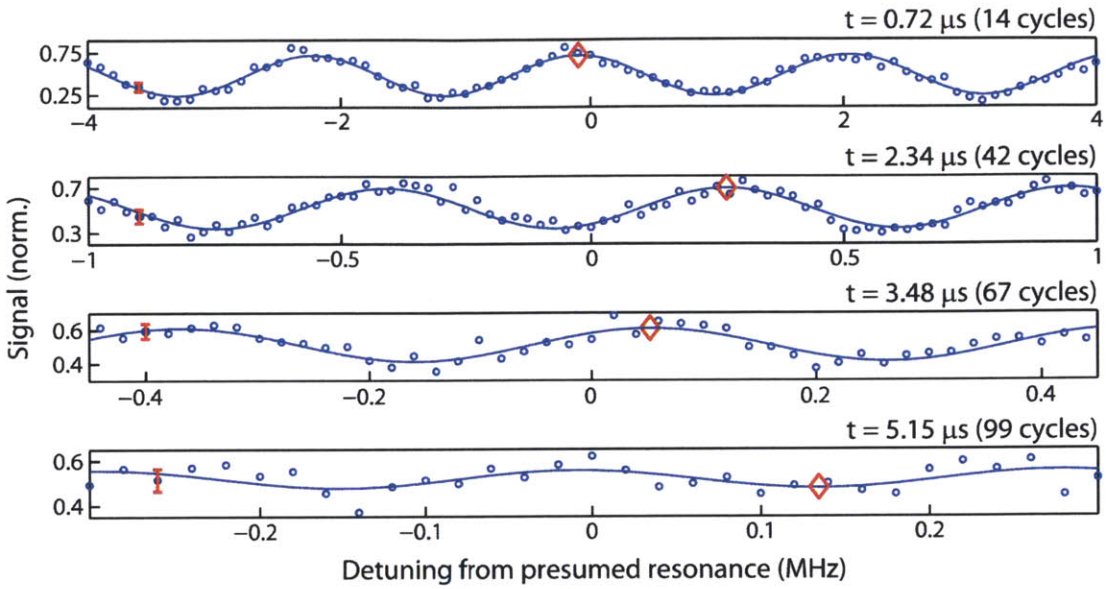

Figure 3-12: **Rotary-echo signals at four different fixed interrogation times, for different detunings.** RE signals at fixed interrogation times as a function of the detuning $\delta\omega$ from resonance, from which $|\frac{\partial \mathcal{S}}{\partial \delta\omega}|$ is numerically calculated to obtain the sensitivity η. With increasing interrogation times, the slopes initially increase, indicating an improvement in η; the effect of decoherence for the longer interrogation times degrades the sensitivity, and the slopes smoothen accordingly. The different amplitude modulations are due to the three-frequencies in the signal, $\{b, A \pm b\}$; polarizing the nuclear spin [46] would eliminate this modulation. From the fitted resonances for each curve (red diamonds), we estimate the true resonance to be at 0.09 ± 0.15MHz from the presumed resonance. Typical errors in the measurement are indicated (red errorbars). Interrogation times are chosen to coincide with minima of the sensitivity in the presence of the hyperfine interaction; in other words, C_A is at a local minimum at those times.

Firstly, in every experimental run, reference curves are acquired along with the signal $\mathcal{S}$; they are noted $\mathcal{R}_0$ for the $|0\rangle$ state as obtained after laser polarization, and $\mathcal{R}_1$ for the $|1\rangle$ state as calibrated by adiabatic inversion. The signal is then normalized as

$$\overline{\mathcal{S}} = \frac{\mathcal{S} - \mathcal{R}_1}{\mathcal{R}_0 - \mathcal{R}_1} \,. \tag{3.15}$$

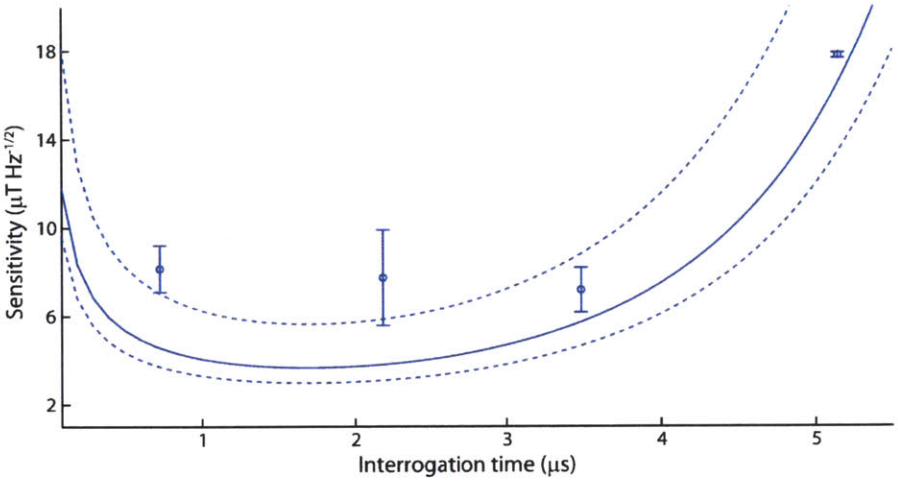

Figure 3-13: **Experimental sensitivity of rotary-echo magnetometry.** For each fixed interrogation time, the minimum sensitivity η within one oscillation period of the fitted oscillation frequency obtained in a), $\tau = \frac{2t\sin(\theta/2)}{\theta}$, is plotted. The experimental points agree in trend with the theoretically expected sensitivities $\eta/(C \times C_A)$ (solid blue curves), here corrected for the presence of static bath noise, $\eta \to \eta e^{(t/T'_{\mathrm{RE}})^2}$. T'_{RE} was computed using a $T_2^\star \approx 2.19 \pm 0.15\mu$s fitting from the Ramsey decay experiment depicted in Figure 3-14. The lower (higher) bounds for the sensitivity are estimated by dividing the theoretical sensitivity by the maximum (minimum) $C \times C_A$ value in the set of points, and are plotted in the dashed blue lines.

The standard deviation of the normalized signal is readily obtained

$$\Delta\overline{\mathcal{S}} = \sqrt{(\Delta\mathcal{R}_0)^2 \left|\frac{\mathcal{S}-\mathcal{R}_1}{(\mathcal{R}_0-\mathcal{R}_1)^2}\right|^2 + (\Delta\mathcal{R}_1)^2 \left|\frac{\mathcal{S}-\mathcal{R}_1}{(\mathcal{R}_0-\mathcal{R}_1)^2} - \frac{1}{\mathcal{R}_0-\mathcal{R}_1}\right|^2 + (\Delta\mathcal{S})^2 \left|\frac{1}{\mathcal{R}_0-\mathcal{R}_1}\right|^2}. \tag{3.16}$$

The sensitivity is calculated for the whole signal

$$\eta(\delta\omega) = \frac{1}{\gamma_e} \frac{\Delta\overline{\mathcal{S}}}{\left|\frac{\partial\overline{\mathcal{S}}}{\partial\delta\omega}\right|}\sqrt{Nt}\ ; \tag{3.17}$$

for each fixed interrogation time t, we single out the minimum sensitivity $\eta(\delta\omega)$ within one period of the fitted oscillation period τ, depicted in Figure 3-12.

The effect of decoherence is included in Figure 3-13 using a fit for $T_2^\star \sim 2.19 \pm 0.15\mu$s from the Ramsey experiment shown in Figure 3-14.b. Assuming static Gaussian noise, we let $\eta_A \to \eta_A e^{(t/T'_{\mathrm{RE}})^2}$, with $T'_{\mathrm{RE}} = \frac{T_2^\star \theta}{2\sin(\theta/2)}$.

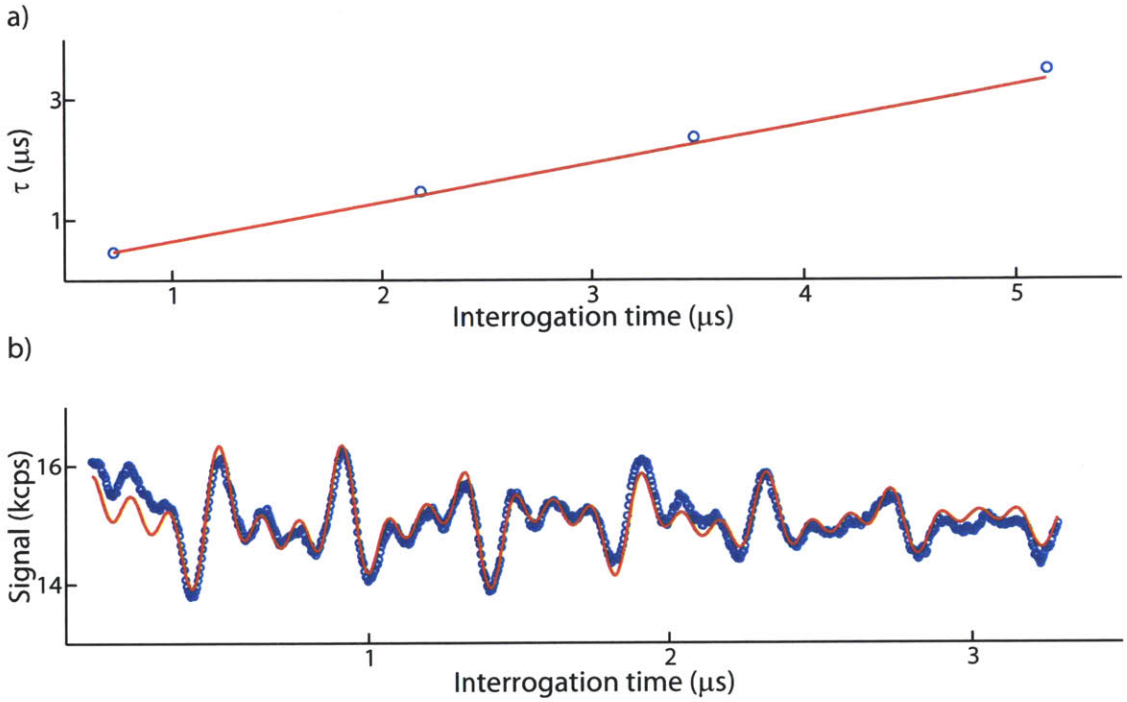

Figure 3-14: **Data fits to determine the experimental sensitivity of rotary-echo magnetometry.** a) The fitted periods τ (blue dots) are linear in t and agree well with the theoretically expected time $\frac{2t\sin(\theta/2)}{\theta}$ (red line). b) The Ramsey signal (purple circles) is fitted to $\mathcal{S}_{\mathrm{Ram}} = k_1 - k_2\left[\cos(\delta\omega t) + \cos((A+\delta\omega)t) + \cos((A-\delta\omega)t)\right]e^{-(t/T_2^\star)^2}$ (red), with fitting parameters $\{k_1, k_2, \delta\omega, A, T_2^\star\}$. In particular, $T_2^\star \sim 2.19 \pm 0.15\mu$s.

The standard deviation for the sensitivity measurements is obtained by

$$\Delta\eta = \frac{1}{\gamma_e}\left|\frac{\partial\eta}{\partial\overline{\mathcal{S}}}\right|\Delta\overline{\mathcal{S}}\sqrt{Nt} = \frac{1}{\gamma_e}\left|\frac{1-2\overline{\mathcal{S}}}{2\sqrt{\overline{\mathcal{S}}(1-\overline{\mathcal{S}})}}\frac{1}{\frac{\partial\overline{\mathcal{S}}}{\partial\delta\omega}}\right|\Delta\overline{\mathcal{S}}\sqrt{Nt}\ . \tag{3.18}$$

Secondly, to every point in the plot there corresponds a factor C taking into account imperfect state detection [1, 47]. While the theoretical signal $\mathcal{S}$ represents the population in the $|1\rangle$ state, measured from the observable $M \equiv |0\rangle\langle 0|$, the experimental signal records photons emitted by both $|0\rangle$ and $|1\rangle$ states, so that the measurement operator is best experimentally described by $M' \equiv n_0|0\rangle\langle 0| + n_1|1\rangle\langle 1|$. Here, $\{n_0, n_1\}$ are Poisson-distributed variables that indicate the number of collected photons; if

perfect state discrimination were possible, $n_0 \to \infty$ and $n_1 \to 0$.

Including this effect, after n full echo cycles, the signal is modified to

$$\mathcal{S}'(n) \approx \frac{1}{4}\left[(3n_0 + n_1 + (n_0 - n_1)\cos\theta) + (n_0 - n_1 - (n_0 - n_1)\cos\theta)\cos\left(\frac{4\delta\omega n}{\Omega}\sin\left(\frac{\theta}{2}\right)\right)\right]. \tag{3.19}$$

We calculate the sensitivity for $\overline{\mathcal{S}'}$ in the best-case scenario of minimum sensitivity given by the accumulated phase $\left(\frac{4\delta\omega n}{\Omega}\sin\left(\frac{\theta}{2}\right)\right) = \frac{\pi}{2}$, and note the existence of a factor C, with respect to the ideal sensitivity, $\eta_{M'} = \eta_M/C$:

$$C^{-1} = \sqrt{1 + \frac{1}{2} + \frac{(-11n_0 + 5n_1)}{2(n_0 - n_1)^2} + \frac{\cos\theta}{2}\left(1 - \frac{(n_0 + n_1)}{(n_0 - n_1)^2}\right) + \frac{8n_0}{(n_0 - n_1)^2\sin^2(\theta/2)}}. \tag{3.20}$$

We use for n_0 (n_1) the mean photon number for the $|0\rangle$ ($|1\rangle$) reference curve during each acquisition for different t. On average, $\overline{n_0} \sim 0.0022 \pm 0.0003$ and $\overline{n_1} \sim 0.0015 \pm 0.0002$.

Thirdly and finally, we also consider the fact that the signal $\overline{\mathcal{S}'}$ has contributions from three detunings $\{\delta\omega, A \pm \delta\omega\}$, where A is the hyperfine coupling between the NV center and spin-1 ^{14}N nucleus; taking such detunings into account is, incidentally, fundamental for the choice of interrogation times: given the modulation imposed by the multiple frequencies in the signal, full echo times yielding a high signal amplitude are preferred. A different strategy would be to polarize the nuclear spin [48].

In order to compare the ideal sensitivity with the experimental one, in our experiments we need to introduce a further correction factor C_A, since the accumulated phase is only equal to the optimal $\frac{\pi}{2}$ for the experimental realizations with $m_I = 0$. We expect the sensitivity to become larger as $\eta_A = \eta_{M'}/C_A = \eta_M/(C \times C_A)$, with

$$C_A^{-1} = \frac{3}{\left|1 + 2\cos\left(\frac{2At\sin(\theta/2)}{\theta}\right)\right|}. \tag{3.21}$$

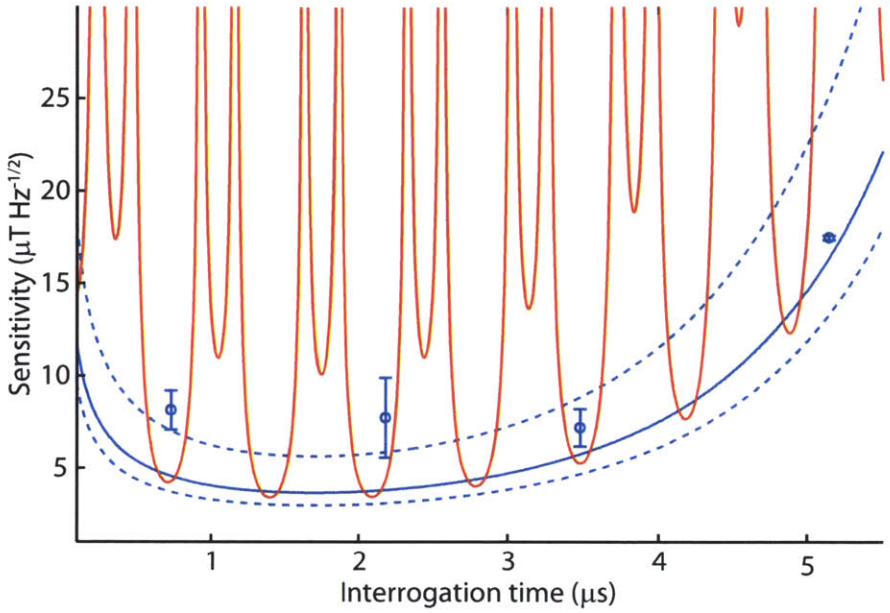

Figure 3-15: **Experimental sensitivity taking into account the time dependence of $\overline{C_A(t)}$.** This plot superimposes to Figure 3 in the main text the expected sensitivity of the quantum magnetometer for all times of the correction factor $\overline{C \times C_A(t)}$ (solid red line). The experimental points (blue circles) are chosen accordingly, so as to have each one of the four realizations of C_A at a local maximum. We see that the data do indeed correspond to points of maximal sensitivity of the quantum magnetometer. We note that the solid blue curve is estimated using an averaged correction factor $\overline{C \times C_A}$, for the four experimental realizations of C and C_A.

In order to estimate $C \times C_A$, we use the fitted value for A at each point ($\overline{A} \sim 2\pi \times (2.21 \pm 0.07)$MHz), the time t corresponding to the number of cycles at which the experimental point was taken, and a corrected $\theta \sim 0.984\pi$ that takes into account the real angle, given the experimental Rabi frequency, imposed by the duration of the echo half cycle, which can be controlled only up to the inverse of the AWG sample rate. A mean total correction factor of $\overline{C \times C_A} \sim (5.9 \pm 1.4) \times 10^{-3}$ is obtained for the set of points. The mean sensitivity curve (solid line) is expressed as the theoretically expected sensitivity in the absence of noise η_M, divided by $\overline{C \times C_A}$. Similarly, the lower (higher) bounds for the sensitivity are estimated by dividing the theoretical sensitivity by the maximum (minimum) $C \times C_A$ value in the set of points, and are plotted in the dashed blue lines of Figure 3-15.

We stress that the presence of an unpolarized nitrogen nuclear spin is the sole re-

sponsible for the $C_A(t)$ factor. The experimental sensitivity points were thus chosen for times having $C_A(t)$ at a local maximum. The landscape of the quantum magnetometer's expected sensitivity as a function of interrogation time, for an averaged $\overline{C \times C_A(t)}$ that considers the time dependence of $\overline{C_A(t)}$, is shown in red in Figure 3-15. The data cover the interrogation times where the sensitivity is optimal, even if the effect of the nitrogen nuclear spin were to be corrected for. Polarizing the nuclear spin [45] or decoupling it with a simple pulse sequence such as a spin echo [27] would remove the effects of the hyperfine coupling and thus set $C_A = 1$. In the experiments, given our careful choice of interrogation times and the estimated hyperfine interaction A, the average over the four points $\overline{C_A} \sim 0.90 \pm 0.13$ is very close to 1.

Repeated read-out methods [45, 49] also help increase the factor C. In this scheme, the state of the nuclear spin is repetitively mapped onto the electronic spin, which is then read out by optical means. The measurement projects the nuclear spin state into a mixed state, but the information about its population difference is preserved, under the assumption that the measurement is a good quantum non-demolition measurement. We can include the effect of these repeated read-out by defining an improved detection efficiency, which shows an improvement $\propto \sqrt{N}$, where N is the number of measurements. The sensitivity needs of course to be further modified to take into account the increased measurement time, but, provided that the time needed for one measurement step is smaller than the interrogation time, it becomes advantageous to use repeated read-outs.

3.4 Experimental resilience to noise

As determined in Chapter 2, the sensitivity of a NV magnetometer is ultimately limited by the interaction of the quantum probe with the nuclear spin bath.

We can model the effect of the spin bath by a classical noise source along σ_z [50],

described by an Ornstein-Ulhenbeck (OU) process of strength σ and correlation time τ_c. In the limit of long τ_c (static bath), the dephasing time associated with RE (Ramsey) magnetometry is $T'_{\mathrm{RE}} = \frac{\theta}{\sigma\sqrt{2}|\sin(\theta/2)|}$ ($T_2^\star = T'_{\mathrm{Ram}} = \frac{\sqrt{2}}{\sigma}$) respectively.

While at the optimum interrogation time $\frac{T'}{2}$ one has $\eta_{\mathrm{RE}}/\eta_{\mathrm{Ram}} = \sqrt{\frac{\theta}{2\sin(\theta/2)^3}} > 1$, RE magnetometry allows a greater flexibility in choosing the effective coherence time, as larger θ increase the resilience to bath noise. Thus one can match the RE interrogation time to the duration of the field one wants to measure.

In addition, RE can yield an overall advantage when taking into consideration the dead-time t_d. If $t_d \gg T'_{Ram}$, as in repeated read-out methods [45], a gain in sensitivity can be reached by exploiting the longer interrogation times enabled by RE magnetometry.

An even larger advantage is given by AC-magnetometry with $2\pi k$-RE [17], since RE provides better protection than DD schemes [14, 51].

Excitation field instabilities along σ_x also accelerate the decay of RE and Rabi signals. However, provided the echo period is shorter than τ_c, RE magnetometry corrects for stochastic noise in Rabi frequency, as seen in Chapter 2. This protection was demonstrated experimentally by applying static and OU noise ($\tau_c \approx 200$ns) in the excitation microwave, both with strength 0.05Ω.

The results for Rabi and π, 5π-RE sequences, depicted in Figure 3-16, clearly show that whereas the Rabi signal decays within $\approx 0.5\mu$s, 5π-RE refocuses static excitation noise and presents only a very weak decay under finite-correlation noise after much longer interrogation times $\approx 3\mu$s, in agreement with theory detailed in Chapter 2; π-RE is robust against the same finite-correlation noise.

In Figure 3-16, 40 realizations of both static and OU ($\tau_c = 200$ns) microwave noise

of strength 0.05Ω, $\Omega \approx 2\pi \times 19$MHz, for Rabi, 5π-RE and π-RE sequences are plotted. In the topmost panel, the peak of Rabi fringes in the presence of static and OU microwave noise are in agreement with the expected theoretical decay. The oscillations at the tail of the signals are due to the finite number of experimental realizations. The peaks of a no-noise Rabi experiment are plotted for comparison. In the middle panel, the peak of the 5π-RE revivals are plotted in the presence of static and OU microwave noise; the peaks of the 5π-RE in the absence of microwave noise are also plotted for comparison. Whereas the echo virtually does not decay in the presence of static noise, under the effect of stochastic noise, the echo decays as stipulated by the analytical formulas. Lastly, in the lowermost panel, the peak of the π-RE revivals are plotted in the presence of OU microwave noise; virtually no decay is found if compared to the peaks of a no-noise experiment.

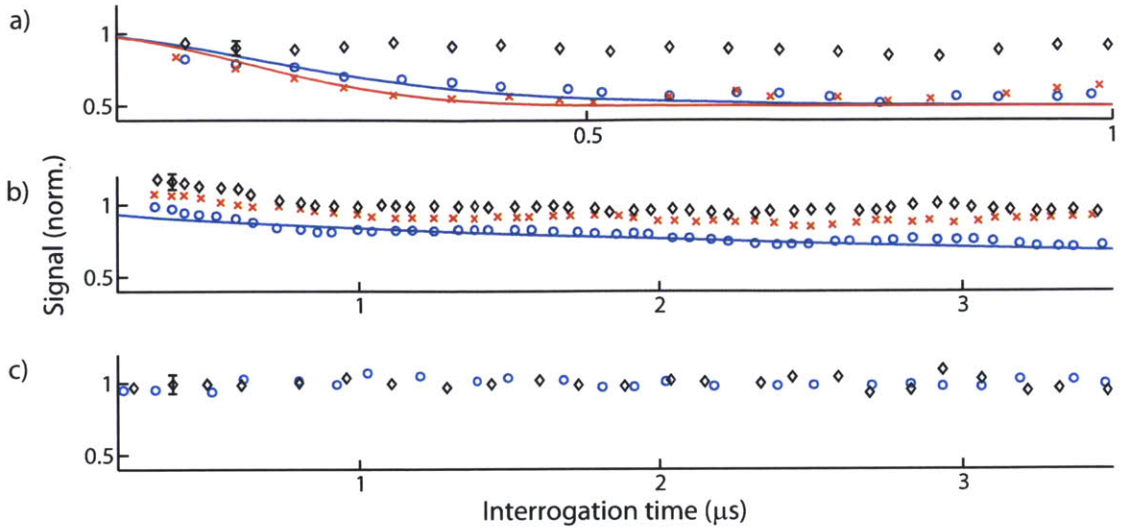

Figure 3-16: **Experimental implementation of microwave frequency noise, against which the rotary-echo is robust.** 40 realizations of both static (red) and OU ($\tau_c = 200$ns, blue) microwave noise of strength 0.05Ω, $\Omega \approx 2\pi\times19$MHz, for a) Rabi, b) 5π-RE and c) π-RE sequences. Typical errors in the measurement are indicated (black errorbars). a) We plot the peak of the Rabi fringes in the presence of static (red crosses) and OU (blue circles) microwave noise, which are in agreement with the expected theoretical decay detailed in Chapter 2 (solid blue line and solid red line, respectively). The oscillations at the tail of the signals are due to the finite number of experimental realizations. The peaks of a no-noise Rabi experiment are plotted for comparison (black diamonds). b) The peak of the 5π-RE revivals are plotted in the presence of static (red crosses) and OU (blue circles) microwave noise; the peaks of the 5π-RE in the absence of microwave noise are also plotted for comparison (black diamonds). Whereas the echo virtually does not decay in the presence of static noise, under the effect of stochastic noise, the echo decays as stipulated by theory (solid blue line) described in Chapter 2. c) The peak of the π-RE revivals are plotted in the presence of OU microwave noise (blue circles); virtually no decay is found if compared to the peaks of a no-noise experiment (black diamonds).

3.5 Applications

The unique ability of the RE magnetometer to adjust its response to distinct noise sources is relevant when the sample producing the magnetic field of interest is immersed in a realistic environment that changes constantly; the advantage is two-fold: interrogation times can be varied, and the protection from noise can be tuned by changing the echo angle.

NV center-based RE magnetometry could find useful application, for example, to sense the activity of differently-sized calcium signaling domains in living cells, more specifically in neurons. Although virtually all neuronal reactions are regulated by diffusing Ca^{2+} ions between membrane channel sources and cytoplasm target receptors, triggering specificity is ensured by the fact that such diffusion events are localized in time and space; the size of the signaling domain, understood as roughly the distance between channel and receptor (50nm to 0.5μm), determines the diffusion timescale (μs to ms) and strength, the latter measured by Ca^{2+} concentration (100 to 1μM) [52, 53]. The smaller, faster-signaling domains have resisted thorough investigation via both diffraction-limited optical microscopy [52], and the use of fluorescing dyes, which do not respond fast or accurately enough to Ca^{2+} transients [54].

Transient calcium fluxes regulate a myriad of cell reactions [52]. The signaling specificity of such fluxes is determined by their duration t and mean travelled distance d between membrane channel and cytoplasm receptor. The magnetic field at a distance r from a transient Ca^{+2} flux composed of l ions is estimated as

$$B(T) = \frac{\mu_0}{4\pi}\frac{2led}{tr^2}\ , \tag{3.22}$$

with e the electron charge, and with the magnetic permeability of the cell approximated by μ_0, the vacuum permeability. Therefore, the minimum required sensitivity to sense the aforedescribed calcium flux is

$$\eta\left(\frac{T}{\sqrt{\text{Hz}}}\right) = \sqrt{2\pi}\frac{\mu_0}{4\pi}\frac{2led}{\sqrt{t}r^2}\sqrt{N}\ . \tag{3.23}$$

The magnetic field produced by as few as 10^5 Ca^{2+}, being diffused within $\sim 10\mu$s through a $\sim$ 200nm domain, can be picked up by a nanodiamond scanning sensor [55, 56] with sensitivity $\sim 10\mu\text{THz}^{-\frac{1}{2}}$ placed at close proximity ($\sim$ 10nm). The trade-off between sensitivity and optimal interrogation time under RE magnetometry can be optimized to the characteristics of the signaling domain under study by a

suitable choice of θ.

Additionally, a RE-magnetometer can map magnetic noise sources given the sensor's well-understood decoherence behavior under different noise profiles, effectively enabling noise spectroscopy for both σ_z and σ_x-type noises. Techniques for repeated read-out in the presence of a strong external magnetic field $\gtrsim$ 1000G [45] can at once improve sensitivities and enable the use of much lower qubit resonance frequencies $\sim$MHz, preferable in biological settings.

3.6 Conclusion

In conclusion, we have demonstrated a quantum magnetometry scheme based on composite-pulses. Its key interest stems both from the continuous-excitation character, offering superior performance for solid state sensors such as the NV center, and from the possibility of tuning the sensor's coherence time and sensitivity in the presence of variable or unknown sensing environments, to protect from or map noise sources.

Current technology enables immediate implementation of such scheme at the nanoscale.

Chapter 4

Time-optimal algebraic $SU(2)$ synthesis with alternating controls: theory

In this chapter, we present an algebraic framework to study the time-optimal synthesis of any unitary in $SU(2)$ in the case of a restricted control set consisting of rotations around two non-parallel axes in the Bloch sphere. Our method bypasses usual control-theoretical techniques, and easily imposes necessary conditions on time-optimal sequences.

In a straightforward fashion, we derive the fact that time-optimal sequences are solely parametrized by three rotation angles, besides presenting general bounds on those angles as a function of the angle between the axes, and the relative rotation speed of each control. Results are substantially different whether allowed rotation angles are in $]0, 2\pi[$ or $]-\pi, \pi]$, corresponding respectively to the availability of only clockwise, or both clockwise and counterclockwise rotations. For rotation angles in $]-\pi, \pi]$, we prove that any finite time-optimal sequence is composed at most of five control concatenations, while for rotation angles in $]0, 2\pi[$, we present scaling laws on the maximum length of any finite time-optimal sequence; bounds for both cases are stricter than previously published ones. These bounds severely constrain the

structure of time-optimal sequences, allowing for a simple numerical search of the time-optimal solution.

An implementation of the method using an anisotropically-coupled spin pair in diamond is discussed in Chapter 5; the nuclear evolution can be steered via the switching of the 'actuator'-electronic spin, in a generally faster and noise-free way, as compared to the direct addressing of the nuclear spin.

4.1 Introduction

The power of quantum computing critically depends on the possibility of implementing a quantum algorithm before the quantum system has dephased. Given constraints in the control fields, it is hence desirable to implement unitaries or gates in the shortest possible time. While time-optimal control has been often studied in the state-to-state framework, unitary gate generation, or synthesis, is of even greater relevance in that it can be incorporated into control protocols regardless of the initial state of the evolving quantum system.

Time-optimal unitary synthesis in $SU(2)$ has been studied in the context of a continuous control set composed of rotations around any axis in a plane in the Bloch sphere [57, 58, 59].

Here, we address the challenge of synthesizing any $SU(2)$ unitary U_{goal} in a time-optimal fashion using a control set uniquely composed of alternating rotations X, V around two non-parallel axes in the Bloch sphere; for example, via the following concatenation:

$$U_{\text{goal}} = \mathsf{X}(t_n) \cdot \ \ldots \ \cdot \mathsf{V}(t_2) \cdot \mathsf{X}(t_1) \cdot \mathbb{1} \ . \tag{4.1}$$

This discrete control set of interest has mostly been studied in a state-to-state transfer framework for bounded controls that can vary in magnitude [60, 61, 62],

where it emerges as the time-optimal solution. It is experimentally relevant in quantum systems for which amplitude and phase modulation of the control fields is relatively difficult; and in systems with restricted control degrees of freedom. An example of the latter is a nuclear ^{13}C spin hyperfine-coupled to the electronic spin of nitrogen-vacancy (NV) centers in diamond [27, 63]. Due to the anisotropy in the hyperfine coupling, the electronic spin can be regarded as an actuator [64]; its switching between spin states steers the nuclear spin evolution, thus providing an alternative to the slow and noisy radio-frequency addressing of the ^{13}C. Moreover, the same control set is also relevant for robotics and satellite motion in $SO(3)$ [60, 65], due to the two-to-one homomorphic mapping of $SU(2)$ onto $SO(3)$.

The standard approach to time-optimal control usually involves general, but rather abstract optimization protocols, such as the Pontryagin maximum principle [66], or variational [67] and geometric control methods [57, 61, 62], all of which are hard to apply to specific cases. In the case of dynamics generated by a smoothly-varying Hamiltonian, a combination of optimization and geometric techniques lead to a simple characterization of the time-optimal solutions [58, 59]. In the case of alternating controls studied here, though, such methods either fail because of time discontinuities or become convoluted in all but some specific cases, thereby losing in generality. Besides, numerical methods to find the time-optimal solution in this case usually rely on the integration of complex systems of differential equations. Driven by experimental needs, we take a different approach, and use only algebraic methods first developed in [68] that turn out to be more powerful than more refined mathematical techniques, at least for the problem at hand. We obtain fully general results for the structure of time-optimal sequences in $SU(2)$, which can then be exploited to dramatically increase the efficiency of a numerical search for specific cases.

This Chapter is organized as follows. After a brief, background introduction to the field of control of quantum systems in Section 4.2, we clarify both the precise problem we tackle in this work and the related notation in Section 4.3. We then

proceed to derive the main results in Sections 4.4, 4.5 and 4.6. These consist in the necessary characteristics of time-optimal concatenations of control elements generating any $SU(2)$ unitary, and impose bounds on: the maximum number of independent parameters, namely three rotation angles; their values; and the maximal concatenation length. A full summary of our results is presented in the three Tables of Section 4.7, which can be used as a reference, independently of the preceding mathematical derivation of results. Finally, in Section 4.8, we discuss experimental settings for which the driving of qubits according to time-optimal controls numerically found using our method might prove beneficial, whilst noting that an experimentally relevant analysis will be conducted in Chapter 5 for the case of a pair of hyperfine-coupled spins in diamond. A conclusion follows in Section 4.9.

4.2 Background: control of quantum systems

Consider the following ordinary differential equation system:

$$\dot{\mathbf{x}}(t) = f(\mathbf{x}(t), \mathbf{u}(t)) \; ; \tag{4.2}$$

$$\mathbf{x}(0) = x_0 \; , \tag{4.3}$$

with $\mathbf{x}(\cdot) \in \mathbb{R}^n$, $\mathbf{u}(\cdot) \in \mathcal{U} \subset \mathbb{R}^m$ and $f : \mathbb{R}^n \times \mathcal{U} \to \mathbb{R}^n$. Here, the trajectory $\mathbf{x}(t)$, also called the 'state', represents the dynamical evolution of some 'system', which responds to piecewise continuous applied controls $\mathbf{u}(t)$ through a functional dependence given by f (assumed continuously differentiable). We will only consider functionals f which are linear in both the state and the control:

$$f(\mathbf{x}(t), \mathbf{u}(t)) \equiv \mathbf{M} \cdot \mathbf{x}(t) + \mathbf{N} \cdot \mathbf{u}(t) \; , \tag{4.4}$$

with real matrices $\mathbf{M}$ of size $n \times n$, and $\mathbf{N}$ of size $n \times m$.

The formal solution to the above differential equation, that can only be expressed

in closed form in special cases, is given by

$$\mathbf{x}(t) = e^{t\cdot\mathbf{M}}x_0 + e^{t\cdot\mathbf{M}}\int_0^t e^{-t'\cdot\mathbf{M}}\,\mathbf{u}(t')\,dt' \ . \tag{4.5}$$

Usually, applying controls $\mathbf{u}(t)$ have a non-null associated cost, generally expressed at time T by

$$J(\mathbf{u}(\cdot)) \equiv \underbrace{\phi(\mathbf{x}(T))}_{\text{terminal cost}} + \underbrace{\int_0^T L(\mathbf{x}(t),\mathbf{u}(t))dt}_{\text{running cost}} \ . \tag{4.6}$$

Here, $L : \mathbb{R}^n \times \mathcal{U} \to \mathbb{R}$, $\phi : \mathbb{R}^n \to \mathbb{R}$, and both are assumed to be continuously differentiable. The terminal cost term is relevant, for instance, if the optimization stresses the final state of the system, x_f,

$$J(\mathbf{u}(\cdot)) = \phi(\mathbf{x}(T)) = ||\mathbf{x}(T) - x_f||^2 \ ; \tag{4.7}$$

on the other hand, the running cost term is associated with situations where the cost accumulates with time; for example, as in the total energy required to steer the system,

$$J(\mathbf{u}(\cdot)) = \int_0^T ||\mathbf{u}(t)||^2 dt \ ; \tag{4.8}$$

or as in the total control time,

$$J(\mathbf{u}(\cdot)) = \int_0^T dt = T \ . \tag{4.9}$$

Hence, the control problem is abstractly posed as follows: find functions $\mathbf{x}(t)$, $\mathbf{u}(t)$ which minimize the appropriate cost functional $J(\mathbf{u}(\cdot))$ while satisfying the dynamical equations given by $\dot{\mathbf{x}}(t) = \mathbf{M}\cdot\mathbf{x}(t) + \mathbf{N}\cdot\mathbf{u}(t)$. Note that the solutions $\mathbf{x}(t)$, $\mathbf{u}(t)$ need not be unique.

Of interest here is the case where $\mathbf{x}(t)$ is a vectorized real parametrization of $SU(2)$ elements (in particular, $x_0 \to \mathbb{1}$ and $x_f \to U_{\text{goal}}$) and where the matrices $\mathbf{M}, \mathbf{N}$ yield the available Hamiltonians $\mathcal{H}$. We thus recover a version of the evolution equation

for unitaries in $SU(2)$,

$$\dot{\mathbf{x}}(t) = -i\ \mathcal{H}(\mathbf{u}(t)) \cdot \mathbf{x}(t)\ , \tag{4.10}$$

with associated cost $J(\mathbf{u}(\cdot)) = T$. Before considering this more restrictive case, we turn to preliminary questions that must be answered regarding the controllability of the dynamical system.

Let $\mathcal{C}$ be the set of final states x_f for which there is a control $\mathbf{u}(t),\ \forall\ t \in [0, T]$, such that $\mathbf{x}(T) = x_f$ for some finite time T; $\mathcal{C}$ is defined as the reachable set of the dynamical system with initial condition $\mathbf{x}(0) = x_0$.

The dynamical system of Eq. 4.2 can be proven to be reachable if the following controllability matrix $\mathbf{C}$ of size $n \times (n \cdot m)$,

$$\mathbf{C} \equiv [\mathbf{N}, \mathbf{M} \cdot \mathbf{N}, \mathbf{M}^2 \cdot \mathbf{N},\ \ldots\ , \mathbf{M}^{n-1} \cdot \mathbf{N}]\ , \tag{4.11}$$

has (full) rank n [69].

Once controllability has been confirmed, one needs to select or at least restrict the set of candidate optimal trajectories. The Pontryagin maximum principle [66], stated below, is a first order necessary condition for optimality that does exactly that.

Define a quantity usually referred to as 'extended Hamiltonian',

$$\mathbb{H}(\mathbf{x}, \mathbf{p}, \mathbf{u}) \equiv (\mathbf{M} \cdot \mathbf{x} + \mathbf{N} \cdot \mathbf{u}) \cdot \mathbf{p}\ ; \tag{4.12}$$

as previously, $\mathbf{x} \in \mathbb{R}^n$, $\mathbf{u} \in \mathcal{U}$; additionally, $\mathbf{p} \in \mathbb{R}^n$ is an 'adjoint state' (or 'costate'), a quantity that can be understood as a time-varying Lagrange multiplier.

Under those conditions, the Pontryagin maximum principle is stated as follows:

let $\mathbf{u}^*$ be a time-optimal control steering the corresponding time-optimal trajectory $\mathbf{x}^*$, with $\mathbf{x}^*(0) = x_0$ and $\mathbf{x}^*(T) = x_f$. Then there exists a costate $\mathbf{p}^*$ such that the original control system; its adjoint equations; and a maximization equation must hold concomitantly:

$$\dot{\mathbf{x}}^* = \frac{\partial H(\mathbf{x}^*, \mathbf{p}^*, \mathbf{u}^*)}{\partial p} \; ; \tag{4.13}$$

$$\dot{\mathbf{p}}^* = -\frac{\partial H(\mathbf{x}^*, \mathbf{p}^*, \mathbf{u}^*)}{\partial x} \; ; \tag{4.14}$$

$$\mathbb{H}(\mathbf{x}^*, \mathbf{p}^*, \mathbf{u}^*) = \max_{\mathbf{u} \in U} \mathbb{H}(\mathbf{x}^*, \mathbf{p}^*, \mathbf{u}) \; . \tag{4.15}$$

Note that $\mathbb{H}$ does not need to be differentiable with respect to $\mathbf{u}$.

For fixed time/free endpoint dynamics, the following extended Hamiltonian and terminal conditions must also be valid at time T:

$$\mathbf{p}^* = \nabla \phi(\mathbf{x}^*(T)) \; ; \tag{4.16}$$

$$\mathbb{H}(\mathbf{x}^*, \mathbf{p}^*, \mathbf{u}^*) = \mathrm{K} \; , \tag{4.17}$$

where K is a constant.

Conversely, for free time/fixed endpoint dynamics (in other words, if the parameter T needs to be determined), the extended Hamiltonian

$$\mathbb{H}(\mathbf{x}^*, \mathbf{p}^*, \mathbf{u}^*) = 0 \; , \tag{4.18}$$

for all times $t \in [0, \tau^*]$, where τ^* is the first time that the time-optimal trajectory $\mathbf{x}^*$ reaches the target state x_f.

In short, the problem of finding the optimal control is mapped into the problem of determining the point-wise maxima of the extended Hamiltonian. Functions $\{\mathbf{x}^*, \mathbf{p}^*, \mathbf{u}^*\}$ that satisfy the conditions of the minimum principle are called extremals.

A proof of the Pontryagin maximum principle can be found in [66].

In practice, it is very hard to explicitly solve Eqs. 4.13 and 4.14, which represent a mixed boundary value problem (in other words, the boundary conditions for the state are given at the initial and final times, whereas the boundary conditions for the costate are only given at the final time) interwoven with nonlinear differential equations; moreover, even in cases for which the solutions of the Pontryagin maximum principle can be found, a selection among optimal trajectories still need to be performed.

On the other hand, another necessary optimality condition, weaker than the one potentially yielded by the pontryagin maximum principle, can more generally be applied to dynamical systems (see, for instance, Section 4.4). It consists of a simple variational analysis; assuming a given control $\mathbf{u}^*(t)$ is optimal, one can vary $\mathbf{u}^* \rightarrow (\mathbf{u}^* + \epsilon)$, with sufficiently small ϵ, and impose that the costs

$$J((\mathbf{u}^* + \epsilon)(\cdot)) - J(\mathbf{u}^*(\cdot)) > 0 \; . \tag{4.19}$$

Very rarely can a complete analytical solution to an optimal control problem be obtained; it is customary then to input any necessary optimality condition that might have been obtained into numerical algorithms to search for the true optimal control.

4.2.1 Time-optimal control

Often, the relevant cost to be minimized is the total time required to steer the system between two fixed points in parameter space. In this case, the solution of the control problem is referred to as 'time-optimal'.

Controls $\mathbf{u}(\cdot) \in \mathcal{U}$ can be bounded or unbounded in magnitude. In the case of unbounded controls (that happens, for instance, when an infinite amount of energy

can be instantaneously transferred to the system), a time-optimal control does not exist; this is due to the fact that, given a proposed time-optimal control $\mathbf{u}^*(t)$, it is always possible to find an alternative $\mathbf{u}^{**}(t)$ which makes the time of transfer arbitrarily closer to an infimum [69]. For bounded controls $|\mathbf{u}| \leq S$, geometric control methods [70] indicate that the time-optimal control is 'bang-bang', that is, every time optimal trajectory is a finite concatenation of controls either at their maximum strength value $\mathbf{u}^*(t) = \pm S$, or equal to zero, $\mathbf{u}^*(t) = 0$, $\forall\, t$. Intervals for which $\mathbf{u}^*(t) = 0$ are referred to in standard control nomenclature as a 'singular arcs'. Using purely algebraic methods, we re-derive the 'bang-bang' property in Section 4.4; moreover, in our approach, singular arcs will be related to time-optimal sequences which are infinitely long.

4.2.2 $SU(2)$ and $SO(3)$ synthesis

Problems of synthesis of $SU(2)$ and $SO(3)$ elements given different control sets have been of interest to the classical and quantum control communities for a long time.

Controllability in the problem of $SU(2)$ and $SO(3)$ synthesis given two independent rotations axes $\vec{n}_a, \vec{n}_b$ has long been established, as well as the order of generation of those groups, that is, the maximum number of concatenations of control elements in between any two unitaries [71]. This number is 3 if $(\vec{n}_a \cdot \vec{n}_b) = 0$ and otherwise equal to

$$\left\lfloor \frac{\pi}{\arccos\left(\vec{n}_a \cdot \vec{n}_b\right)} \right\rfloor + 2\,. \tag{4.20}$$

For the same control set, also studied is the problem of minimum number of concatenations which are necessary to generated any unitary, as a function of unitary parameters [72]. These two problems do not seek to minimize the time needed for synthesis.

Now, generating $SU(2)$ elements using two alternating controls in minimum time

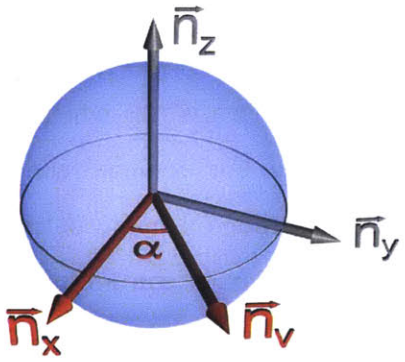

Figure 4-1: **Generation of $SU(2)$ element via rotations around two non-parallel axes in the Bloch sphere.** We investigate the generation of any $SU(2)$ element by solely allowing rotations around two non-parallel axis in the Bloch sphere, namely $\vec{n}_x$ and $\vec{n}_v$, which are separated by an angle α.

has obvious interest for quantum information purposes; it is, however, worthwhile to mention that time-optimal synthesis of $SO(3)$ has as relevant applications in, for instance, robotics. One can imagine a rigid body that can only be rotated around two fixed axes, and of interest is to bring this body into a given configuration in minimal time. This dynamical system is, indeed, a model for satellite reorientation [73].

4.3 Statement of problem and notation

We investigate the time-optimal synthesis of $SU(2)$ elements up to a global phase, using an alternating control set denoted by $\{\mathsf{X}(t_x) \equiv e^{-i\frac{t_x}{2}\sigma_x}, \mathsf{V}(t_v) \equiv e^{-i\frac{t_v}{2}\sigma_v}\}$. Here, $\sigma_v = \cos(\alpha)\sigma_x + \sin(\alpha)\sigma_y$, with $\alpha \in]0, \pi[$ and $\sigma_{x,y}$ the Pauli matrices; α is usually fixed by experimental constraints. The controls represent rotations of angle $t_{x,v}$ around two axes in the Bloch sphere parametrized by $\vec{n}_x = (1, 0, 0)$ and $\vec{n}_v = (\cos(\alpha), \sin(\alpha), 0)$, and separated by an angle α. This situation is depicted in Figure 4-1. For $\alpha = \pi/2$, the controls are orthogonal and $\mathsf{V}(\cdot) = \mathsf{Y}(\cdot)$.

As already discussed, this restricted control set confers complete controllability in

$SU(2)$ up to a global phase, $\forall\ \alpha \neq 0, \pi$ [74]; moreover, any element of $SU(2)$ can be generated by the control set (albeit in a non-time-optimal way) in at most $(\lfloor \frac{\pi}{\alpha} \rfloor + 2)$ concatenations [71].

Experimental constraints determine whether rotations can be realized only in the clockwise direction or in both clockwise and counterclockwise directions. In the first case we have $t_{x,v} \in]0, 2\pi[$, with two accessible Hamiltonians, $\{\sigma_x, \sigma_v\}$; in the second case we can either consider four accessible Hamiltonians, $\{\pm\sigma_x, \pm\sigma_v\}$ with $t_{x,v} \in]0, \pi]$, or, equivalently, two Hamiltonians with $t_{x,v} \in]-\pi, \pi]$, as we will do in the following. Our analysis is subdivided accordingly, in cases noted $t > 0$ and $t \lesseqgtr 0$.

Additionally, in physical realizations, it is often the case that rotations around distinct axes have different evolution speeds. To account for that, we introduce a dimensionless parameter $\kappa \in [0, 1]$ and assume, without loss of generality, that a rotation $\mathsf{V}(t_v)$ is effectively synthesized in a (shorter or equal) time $\kappa|t_v|$.

We call 'n-sequence' the synthesis of a unitary U_{goal} using n alternating controls. An n-sequence is time-optimal if it has minimum time cost among sequences of all lengths generating U_{goal}. A time-optimal sequence can be of finite length or infinite. It is immediate that any subsequence of a time-optimal sequence must be time-optimal itself. In the text, we denote such subsequences $U^\star$, as in $U_{\text{goal}} = \ldots \cdot U^\star \cdot \ldots \cdot \mathbb{1}$.

In what follows, we present necessary conditions that time-optimal n-sequences generating any $U_{\text{goal}} \in SU(2)$ must obey.

4.4 Relationship between internal rotation angles

The problem of finding a time-optimal sequence seems at first intractable since it requires optimizing over a large – possibly infinite – number of parameters. Here we

show instead that three angles are sufficient to parametrize time-optimal sequences of any length (both finite and infinite). Our proof generalizes and strengthens previous results [68] that only considered clockwise rotations.

The starting point of the analysis is a perturbative approach that fixes the relationship between rotation angles in any time-optimal sequence of length $n \geq 4$ [68] (sequences with $n \leq 3$ are always parametrized by at most three angles). Assuming the 4-subsequence

$$U^\star = \mathsf{X}(t_f) \cdot \mathsf{V}(t_v) \cdot \mathsf{X}(t_x) \cdot \mathsf{V}(t_i) \tag{4.21}$$

is time-optimal, the total time needed to synthesize $U^\star$, $\mathcal{T} \equiv |t_f| + \kappa|t_v| + |t_x| + \kappa|t_i|$, is at a global minimum.

Let t be $t(\delta)$. We examine an infinitesimal perturbation of the sequence

$$\mathsf{X}(t_f(\delta)) \cdot \mathsf{V}(t_v(\delta)) \cdot \mathsf{X}(t_x(\delta)) \cdot \mathsf{V}(t_i(\delta)) = U^\star + dU^\star \tag{4.22}$$

that keeps the unitary unchanged to first order, $dU^\star = 0$. By expanding the unitaries to first order in δ around $\delta = 0$,

$$\mathsf{X}(t(\delta)) \approx \mathsf{X}(t(0)) \cdot \left(\mathbb{1} - i \, \frac{\sigma_x}{2} \cdot \delta \, \frac{dt}{d\delta}\bigg|_{\delta=0} \right) \equiv \mathsf{X}(t(0)) \cdot \left(\mathbb{1} - i \, \frac{\sigma_x}{2} \cdot \epsilon \right) \, , \tag{4.23}$$

and using relationships such as

$$\begin{aligned} \sigma_x \cdot \mathsf{V}(t_v) &= \mathsf{V}(t_v) \cdot \mathsf{V}(-t_v) \cdot \sigma_x \cdot \mathsf{V}(t_v) \\ &= \mathsf{V}(t_v) \cdot \left(\cos^2\left(\frac{t_v}{2}\right) \sigma_x + \sin^2\left(\frac{t_v}{2}\right) \sigma_v \sigma_x \sigma_v - i \sin\left(\frac{t_v}{2}\right) \cos\left(\frac{t_v}{2}\right) [\sigma_x, \sigma_v] \right) \\ &\equiv \mathsf{V}(t_v) \cdot \eta \, , \end{aligned} \tag{4.24}$$

and similarly

$$\mathsf{X}(t_x) \cdot \sigma_v \equiv \eta' \cdot \mathsf{X}(t_x) \, , \tag{4.25}$$

with

$$\eta' \equiv \left(\cos^2\left(\frac{t_x}{2}\right)\sigma_v + \sin^2\left(\frac{t_x}{2}\right)\sigma_x\sigma_v\sigma_x - i\sin\left(\frac{t_x}{2}\right)\cos\left(\frac{t_x}{2}\right)[\sigma_v,\sigma_x]\right) \ , \quad (4.26)$$

we find that

$$U^\star + dU^\star = \mathsf{X}(t_f)\cdot\mathsf{V}(t_v)\cdot\left(\mathbb{1} - i\frac{\epsilon_f}{2}\eta\right)\cdot\left(\mathbb{1} - i\frac{\epsilon_v}{2}\sigma_v\right)\cdot\left(\mathbb{1} - i\frac{\epsilon_x}{2}\sigma_x\right)\cdot\left(\mathbb{1} - i\frac{\epsilon_i}{2}\eta'\right)\cdot\mathsf{X}(t_x)\cdot\mathsf{V}(t_i) \ . \quad (4.27)$$

Imposing $dU^\star = 0$ gives

$$\left(\mathbb{1} - i\frac{\epsilon_f}{2}\eta\right)\cdot\left(\mathbb{1} - i\frac{\epsilon_v}{2}\sigma_v\right)\cdot\left(\mathbb{1} - i\frac{\epsilon_x}{2}\sigma_x\right)\cdot\left(\mathbb{1} - i\frac{\epsilon_i}{2}\eta'\right) = \mathbb{1} \ . \quad (4.28)$$

To first order in ϵ, Eq. 4.28 yields three distinct constraint equations.
In addition, by assumption of time-optimality, the first derivative of the total time must obey, for $\delta \neq 0$,

$$\begin{aligned}
\delta\frac{dT}{d\delta} &= \mathrm{sgn}(t_f)\cdot\delta\left.\frac{dt_f}{d\delta}\right|_{\delta=0} + \kappa\ \mathrm{sgn}(t_v)\cdot\delta\left.\frac{dt_v}{d\delta}\right|_{\delta=0} \\
&\quad + \mathrm{sgn}(t_x)\cdot\delta\left.\frac{dt_x}{d\delta}\right|_{\delta=0} + \kappa\ \mathrm{sgn}(t_i)\cdot\delta\left.\frac{dt_i}{d\delta}\right|_{\delta=0} \\
&= \mathrm{sgn}(t_f)\ \epsilon_f + \kappa\ \mathrm{sgn}(t_v)\ \epsilon_v + \mathrm{sgn}(t_x)\ \epsilon_x + \kappa\ \mathrm{sgn}(t_i)\ \epsilon_i \\
&= 0 \ . \qquad (4.29)
\end{aligned}$$

Solutions of the above four equations give t_v as a function of t_x (or vice-versa) and are obtained upon imposing the non-triviality condition given by

$$\begin{vmatrix}
\cos(t_v) & 0 & 1 & 2\cos(\alpha)\sin^2\left(\frac{t_x}{2}\right) \\
2\cos(\alpha)\sin^2\left(\frac{t_v}{2}\right) & 1 & 0 & \cos(t_x) \\
\sin(t_v) & 0 & 0 & \sin(t_x) \\
\mathrm{sgn}(t_f) & \kappa\ \mathrm{sgn}(t_v) & \mathrm{sgn}(t_x) & \kappa\ \mathrm{sgn}(t_i)
\end{vmatrix} = 0 \ . \quad (4.30)$$

Analogous calculations provide similar constraint equations for a 4-subsequence of type $U^\star = \mathsf{V}(t_f)\cdot\mathsf{X}(t_x)\cdot\mathsf{V}(t_v)\cdot\mathsf{X}(t_i)$.

General solutions to Eq. 4.30 are found by considering the eight relative sign combinations for $\{t_i, t_x, t_v, t_f\}$; they fix t_v as a function of t_x for both finite $n \geq 4$ and infinitely long time-optimal sequences. These solutions are presented in Table 4.1. In this table, the sign vector entry corresponds to the signs of $\{t_i, t_x, t_v, t_f\}$.

Importantly, in true minima, the second derivative of the total time function must obey $\frac{d^2\mathcal{T}}{d\delta^2} > 0$, independently of the perturbation parameter δ. Note that, in [68], only the criticality condition $\frac{d\mathcal{T}}{d\delta} = 0$ is considered.

To discriminate the true minima, we perform a calculation similar to the preceding one, but expanding to second order in δ around $\delta = 0$, thereby obtaining:

$$\begin{aligned}\delta^2 \frac{d^2\mathcal{T}}{d\delta^2} = \operatorname{sgn}(t_f) \cdot \delta^2 \left.\frac{d^2 t_f}{d\delta^2}\right|_{\delta=0} + \kappa \operatorname{sgn}(t_v) \cdot \delta^2 \left.\frac{d^2 t_v}{d\delta^2}\right|_{\delta=0} \\ + \operatorname{sgn}(t_x) \cdot \delta^2 \left.\frac{d^2 t_x}{d\delta^2}\right|_{\delta=0} + \kappa \operatorname{sgn}(t_i) \cdot \delta^2 \left.\frac{d^2 t_i}{d\delta^2}\right|_{\delta=0} ; \end{aligned} \tag{4.31}$$

$$\mathsf{X}(t(\delta)) \approx \mathsf{X}(t(0)) \cdot \left[\mathbb{1} - i \frac{\sigma_x}{2} \cdot \left(\delta \left.\frac{dt}{d\delta}\right|_{\delta=0} + \delta^2 \left.\frac{d^2 t}{d\delta^2}\right|_{\delta=0} \right) - \left(\frac{\delta}{2} \left.\frac{dt}{d\delta}\right|_{\delta=0} \right)^2 \right] . \tag{4.32}$$

All eight cases in Table 4.1 obey $\frac{d\mathcal{T}}{d\delta} = 0$, but only some of them have regions in $\{\alpha, \kappa, t_x\}$ space with $\frac{d^2\mathcal{T}}{d\delta^2} > 0$. We thus established that if the experimentally given parameters α, κ are such that $\frac{d^2\mathcal{T}}{d\delta^2} \not> 0$, the time-optimal sequence generating any U_{goal} must be $n \leq 3$ long.

If a time-optimal sequence has length $n > 4$, any 4-subsequence must be time-optimal. Therefore, all pairs of 'internal' rotation angles $\{t_i, t_{i+1}\}$, with $1 < i < n-1$, must obey the prescribed relations in Table 4.1. From this, one immediately infers that all internal rotation angles t_i with $1 < i < n$ are fixed by a single internal time t_x.

In conclusion, time-optimal sequences which are $n \geq 4$ long have only three independent parameters, namely the initial and final rotation angles t_i, t_f, and the internal

case	signs	times	$\exists\ \delta^2 \frac{d^2\mathcal{T}}{d\delta^2} > 0$	length
(a)	$\{+,+,+,+\}$	$\tan(t_v/2) = \tan(t_x/2)\,\frac{\kappa-\cos(\alpha)}{1-\kappa\cos(\alpha)}$	yes	n, ∞
(b)	$\{+,+,+,-\}$	$\tan(t_v/2) = -\frac{\kappa+\cos(\alpha)+\cos(t_x)(\kappa-\cos(\alpha))}{(1-\kappa\cos(\alpha))\sin(t_x)}$	yes	$\varnothing$
(c)	$\{+,+,-,+\}$	$\tan(t_x/2) = \frac{1-\kappa\cos(\alpha)+\cos(t_v)(1+\kappa\cos(\alpha))}{(\kappa+\cos(\alpha))\sin(t_v)}$	yes	$\varnothing$
(d_1)	$\{+,+,-,-\}$	$\tan(t_x/2) = -\kappa\tan(t_v/2)$	yes	n
(d_2)	$\{+,+,-,-\}$	$\tan(t_v/2) = \cot(t_x/2)\sec(\alpha)$	no	$\varnothing$
(e)	$\{+,-,+,+\}$	$\tan(t_v/2) = \frac{\kappa-\cos(\alpha)+\cos(t_x)(\kappa+\cos(\alpha))}{(1+\kappa\cos(\alpha))\sin(t_x)}$	yes	$\varnothing$
(f)	$\{+,-,+,-\}$	$\tan(t_v/2) = -\tan(t_x/2)\,\frac{\kappa+\cos(\alpha)}{1+\kappa\cos(\alpha)}$	yes	∞
(g_1)	$\{+,-,-,+\}$	$\tan(t_x/2) = \kappa\tan(t_v/2)$	yes	n
(g_2)	$\{+,-,-,+\}$	$\tan(t_v/2) = \cot(t_x/2)\sec(\alpha)$	no	$\varnothing$
(h)	$\{+,-,-,-\}$	$\tan(t_x/2) = -\frac{1+\kappa\cos(\alpha)+\cos(t_v)(1-\kappa\cos(\alpha))}{(\kappa-\cos(\alpha))\sin(t_v)}$	yes	$\varnothing$

Table 4.1: **Relationship between internal rotation angles in a time-optimal n-sequence, $n \geq 4$.** Also described are the lengths of candidate time-optimal sequences. Note that case (a) can only yield a finite sequence if only positive times are allowed.

angle parameter t_x.

This simple, yet non-trivial result is the essential keystone that allows for a numerical search of time-optimal solutions; if this were not the case, in the presence of a growing number of parameters, any numerical search would soon become impractical. The numerical analysis will be further simplified by the results of Sections 4.5 and 4.6, which give additional constraints of the possible values of the three parameters.

We now summarize the relationship $t_v(t_x)$ by case.

■ Case $t > 0$. The relationship between internal times for sign combination (a) in Table 4.1 is [68]

$$\tan\left(\frac{t_v}{2}\right) = \tan\left(\frac{t_x}{2}\right)\cdot\frac{\kappa-\cos(\alpha)}{1-\kappa\cos(\alpha)} \equiv \tan\left(\frac{t_x}{2}\right)\cdot K_1\ . \tag{4.33}$$

Note that $\kappa > \cos(\alpha) \Leftrightarrow K_1 > 0$ (conversely, $\kappa < \cos(\alpha) \Leftrightarrow K_1 < 0$). This naturally subdivides case $t > 0$ in two subcases with different structures of time-optimal

sequences.

For $\kappa < \cos(\alpha)$, imposing $\frac{d^2\mathcal{T}}{d\delta^2}$ constrains $t_x < \pi$.

For $\kappa > \cos(\alpha)$, $\frac{d^2\mathcal{T}}{d\delta^2} > 0$ only holds for $\pi < t_x < \frac{5\pi}{3}$ and $\alpha < \frac{2\pi}{3}$; from this we easily conclude that, if $\alpha > \frac{2\pi}{3}$, finite time-optimal sequences are at most $n = 3$ long. In the limit $\kappa = 1$, $t_v = t_x$, with the constraint $t_x > \pi$ imposed by the second derivative condition.

The relationship of Eq. 4.33 must be valid for any time-optimal sequence of length $n \geq 4$, including for an infinite concatenation of control elements that realizes a given U_{goal} in (finite) optimal time. Thus, in this limit, necessarily $t_x \to 0$, and the relationship between t_x and t_v is obtained by noting that

$$\lim_{t_x \to 0} t_v = (t_x \cdot K_1 + o(t_x)) \bmod 2\pi \ . \tag{4.34}$$

If $K_1 < 0$, $t_v \to 2\pi - t_x \cdot |K_1| \approx 2\pi$; an infinite concatenation of control elements in this case would take an infinite time cost. Hence, if $\kappa < \cos(\alpha)$, time-optimal sequences must be finite [68].

Infinite-length time optimal sequence might thus exist only for $\kappa > \cos(\alpha)$. We define a rotation Q that effectively represents an infinite concatenation of control elements:

$$\mathsf{Q}(t_Q) \equiv e^{-i\frac{t_Q}{2}(\sigma_x + K_1\sigma_v)} = \lim_{k\to\infty} \left[\mathsf{X}\left(\frac{t_x}{k}\right) \cdot \mathsf{V}\left(\frac{t_v}{k}\right)\right]^k = \lim_{k\to\infty} \left[\mathsf{V}\left(\frac{t_v}{k}\right) \cdot \mathsf{X}\left(\frac{t_x}{k}\right)\right]^k . \tag{4.35}$$

The normalized axis of the Q rotation, $\vec{n}_q$, exactly bisects α for $\kappa = 1$; as κ decreases towards its lower limit $\cos(\alpha)$, the axis approaches $\vec{n}_x$: $(\vec{n}_v \cdot \vec{n}_q) = \kappa\ (\vec{n}_x \cdot \vec{n}_q)$. The

axis normalization is given by

$$N_q \equiv \frac{\sqrt{1+\kappa^2-2\kappa\cos(\alpha)}\sin(\alpha)}{1-\kappa\cos(\alpha)} \ . \tag{4.36}$$

The implementation time cost associated with such a $\mathsf{Q}(t_Q)$ rotation is $t_Q\,(1+\kappa\cdot K_1)$, where $t_Q \in \left]0, \frac{2\pi}{N_q}\right[$ is in principle unbounded. For simplicity, we define the renormalized time $t_q \equiv t_Q \cdot N_q$, which is bounded as $t_q \in]0, 2\pi[$.

■ **Case $t \gtrless 0$.** All eight relative sign combinations in Table 4.1 must be considered. Cases (d_2) and (g_2) have $\frac{d^2\mathcal{T}}{d\delta^2} = 0$ in all regions of $\{\alpha, \kappa, t_x\}$ space; incidentally, such cases have $\frac{d^3\mathcal{T}}{d\delta^3} \neq 0$, thus unambiguously ruling them out as saddle points.

We also find in Section 4.5 that cases (a), (b), (c), (e), (f) and (h) cannot yield finite time-optimal sequences. Hence, we establish that internal times in a finite time-optimal n-sequence, $n \geq 4$, must satisfy the time relationship described by cases (d_1) and (g_1),

$$\tan\left(\frac{t_v}{2}\right) = \pm\tan\left(\frac{t_x}{2}\right)\frac{1}{\kappa} \ , \tag{4.37}$$

with the only possible sign structures being

$$\{+,+,-,-\}, \{-,-,+,+\}, \{+,-,-,+\} \text{ and } \{-,+,+,-\} \ . \tag{4.38}$$

In infinite sequences, case (b) is ruled out since

$$\lim_{k\to\infty}\left[\mathsf{X}\left(\frac{t_x}{k}\right)\cdot\mathsf{V}\left(\frac{t_v}{k}\right)\cdot\mathsf{X}\left(\frac{t_x}{k}\right)\cdot\mathsf{V}\left(\frac{-t_v}{k}\right)\right]^k = [\mathsf{X}(t_x+t_x)\cdot\mathsf{V}(t_v-t_v)] = \mathsf{X}(2t_x) \ ; \tag{4.39}$$

in a similar fashion, we rule out cases (c), (e) and (h), which yield, respectively, $\mathsf{V}(2t_v)$, $\mathsf{X}(2t_x)$ and $\mathsf{V}(2t_v)$. Analogously, cases (d) and (g) are ruled out because

$$\lim_{k\to\infty}\left[\mathsf{X}\left(\frac{t_x}{k}\right)\cdot\mathsf{V}\left(\frac{t_v}{k}\right)\cdot\mathsf{X}\left(\frac{-t_x}{k}\right)\cdot\mathsf{V}\left(\frac{-t_v}{k}\right)\right]^k = [\mathsf{X}(t_x-t_x)\cdot\mathsf{V}(t_v-t_v)] = \mathbb{1} \ . \tag{4.40}$$

We thus establish that time and sign relationships allowed for infinite time-optimal sequences are those described by cases (a) and (f) in Table 4.1, namely

$$\tan\left(\frac{t_v}{2}\right) = \tan\left(\frac{t_x}{2}\right) K_1 \ , \ \text{with signs } \{+,+,+,+\},\ \{-,-,-,-\}\ ; \tag{4.41}$$

$$\tan\left(\frac{t_v}{2}\right) = -\tan\left(\frac{t_x}{2}\right) \frac{\kappa+\cos(\alpha)}{1+\kappa\cos(\alpha)} \equiv -\tan\left(\frac{t_x}{2}\right) K_3 \ , \tag{4.42}$$

$$\text{with signs } \{+,-,+,-\},\ \{-,+,-,+\}\ .$$

We already considered case (a), which gives rise to potential solutions via the operator $\mathsf{Q}(t_Q)$ if $\kappa > \cos(\alpha)$; to take into account counter-clockwise rotations, we redefine t_q so that $t_q \in\ ]-\pi,\pi]$.

Case (f) defines a rotation P,

$$\mathsf{P}(t_P) \equiv e^{-i\frac{t_P}{2}(\sigma_x - K_3\sigma_v)} = \lim_{k\to\infty}\left[\mathsf{X}\left(\frac{t_x}{k}\right)\cdot\mathsf{V}\left(\frac{-t_v}{k}\right)\right]^k = \lim_{k\to\infty}\left[\mathsf{V}\left(\frac{-t_v}{k}\right)\cdot\mathsf{X}\left(\frac{t_x}{k}\right)\right]^k . \tag{4.43}$$

The normalization of the axis $\vec{n}_p$ is given by

$$N_p \equiv \frac{\sqrt{1+\kappa^2+2\kappa\cos(\alpha)}\,\sin(\alpha)}{1+\kappa\cos(\alpha)} \ . \tag{4.44}$$

As previously,

$$\lim_{t_x\to 0} t_v = -t_x\cdot K_3 + \ o(t_x)\ ; \tag{4.45}$$

in order to maintain the alternating sign structure, $K_3 > 0$, which is obtained iif $\kappa > \cos(\pi-\alpha)$, defining the regions where a time-optimal sequence involving P may exist. The time cost associated with a $\mathsf{P}(t_P)$ rotation is $t_P\,(1+\kappa\cdot K_3)$.

As for the Q rotation, $t_P \in\ ]-\pi/N_p, \pi/N_p]$ is again unbounded. For simplicity, we renormalize $t_p \equiv t_P\cdot N_p$, $t_p \in\ ]-\pi,\pi]$.

4.5 Bounds on internal rotation angles and on maximal length n

In the preceding Section, we have shown that time-optimal sequences only depend on three angles. This still leaves undetermined the values of these angles, as well as the total length of the time-optimal sequence. In what follows, we will derive bounds for both the sequence length n and the values of the angles. This not only allows further restricting of the parameter space explored by a numerical search, but also sets constraints on the total time required to synthesize arbitrary unitaries.

In this Section, we concentrate on the sequence length n and on maximal values for the internal angle t_x (equivalently, for t_v). For given values of the angle α between rotation axes and the relative rotation speeds κ, we will show that only some values of t_x can occur in time-optimal sequences, a constraint expressed in terms of admissible regions in the $\{t_x, \alpha, \kappa\}$ space. Our core results are obtained by noting that subsequences $U^\star$ can have alternative decompositions with different total synthesis times in distinct regions of the parameter space; ruling out some of these equivalent decompositions as non-optimal defines the admissible regions.

We extensively use analytical decompositions of a given $U^\star$ into consecutive rotations $\mathsf{A}, \mathsf{B}, \mathsf{C}$ around three non-orthogonal axes $\vec{n}_a, \vec{n}_b, \vec{n}_c$ [75] (henceforth noted **decomposition #1**),

$$U^\star = \mathsf{C}(\theta_3) \cdot \mathsf{B}(\theta_2) \cdot \mathsf{A}(\theta_1) \; . \tag{4.46}$$

Such decompositions exist if and only if [75]

$$|\vec{n}_c^T (u_{\text{goal}} - \vec{n}_b \vec{n}_b^T) \vec{n}_a| \leq \sqrt{1 - (\vec{n}_c^T \vec{n}_b)^2} \sqrt{1 - (\vec{n}_a^T \vec{n}_b)^2} \; , \tag{4.47}$$

where u_{goal} is the $SO(3)$ representation of $U_{\text{goal}} \in SU(2)$ up to a global phase [76]:

$$U_{\text{goal}} \equiv \begin{pmatrix} A+iC & B+iD \\ -B+iD & A-iC \end{pmatrix}$$

$$\Leftrightarrow$$

$$u_{\text{goal}} = \begin{pmatrix} 1-2(B^2+C^2) & 2(AC+BD) & 2(-AB+CD) \\ 2(-AC+BD) & -1+2(A^2+B^2) & 2(AD+BC) \\ 2(AB+CD) & 2(-AD+BC) & -1+2(A^2+C^2) \end{pmatrix} , \tag{4.48}$$

with $A, B, C, D \in [-1, 1]$ and $A^2 + B^2 + C^2 + D^2 = 1$.

When they exist, the decompositions form either a distinct or degenerate pair, with rotation angles $\theta_i \in]-\pi, \pi]$ given by [75]

$$\theta_2 = \arctan_2(b, a) \pm \arctan_2(\sqrt{a^2+b^2-c^2}, c) \ ; \tag{4.49}$$

$$\theta_1 = -\arctan_2(w_a^T \vec{n}_a \times v_a, v_a^T w_a - (v_a^T \vec{n}_a) \cdot (w_a^T \vec{n}_a)) \ ; \tag{4.50}$$

$$\theta_3 = \arctan_2(w_c^T \vec{n}_c \times v_c, v_c^T w_c - (v_c^T \vec{n}_c) \cdot (w_c^T \vec{n}_c)) \ , \tag{4.51}$$

with the definitions

$$\begin{aligned} a &= -\vec{n}_c^T \cdot (\text{rod}(\vec{n}_b))^2 \cdot \vec{n}_a \ ; \\ b &= \vec{n}_c^T \cdot (\text{rod}(\vec{n}_b)) \cdot \vec{n}_a \ ; \\ c &= \vec{n}_c^T \cdot (u_{\text{goal}} - \mathbb{1} - (\text{rod}(\vec{n}_b))^2) \cdot \vec{n}_a \ ; \\ v_a &= e^{-\theta_2 \cdot (\text{rod}(\vec{n}_b))} \cdot \vec{n}_c \ ; \\ w_a &= u_{\text{goal}}^T \cdot \vec{n}_c \ ; \\ v_c &= e^{\theta_2 \cdot (\text{rod}(\vec{n}_b))} \cdot \vec{n}_a \ ; \\ w_c &= u_{\text{goal}} \cdot \vec{n}_a \ . \end{aligned} \tag{4.52}$$

Here $\arctan_2(y, x) = \text{Arg}(x+iy)$ and $\text{rod}(\{x, y, z\})$ is the matrix in Rodrigues' rotation

formula [76]:

$$\mathrm{rod}(\{x,y,z\}) = \begin{pmatrix} 0 & -z & y \\ z & 0 & -x \\ -y & x & 0 \end{pmatrix} .$$

A special case of the method above is obtained by noting that any 3-subsequence

$$U^\star = \mathsf{A}(\delta)\cdot\mathsf{B}(t)\cdot\mathsf{A}(\delta)\ , \tag{4.53}$$

$\forall\ |\delta| < |t|$, can be alternatively synthesized as

$$U^\star = \mathsf{B}(\tau)\cdot\mathsf{A}(\mu)\cdot\mathsf{B}(\tau)\ . \tag{4.54}$$

To first order in δ the times are

$$\tau = \frac{t}{2} + \delta\ (\vec{n}_a\cdot\vec{n}_b)\left(1-\cos\left(\frac{t}{2}\right)\right) + o(\delta^2)\ ; \tag{4.55}$$

$$\mu = 2\,\delta\cos\left(\frac{t}{2}\right) + o(\delta^2)\ . \tag{4.56}$$

For the time-optimal synthesis problem, $\mathsf{A}(\delta)\cdot\mathsf{B}(t)\cdot\mathsf{A}(\delta)$ is to be replaced with $\mathsf{V}(\delta)\cdot\mathsf{X}(t_x)\cdot\mathsf{V}(\delta)$ or $\mathsf{X}(\delta)\cdot\mathsf{V}(t_v)\cdot\mathsf{X}(\delta)$. In both cases we have $(\vec{n}_a\cdot\vec{n}_b) = (\vec{n}_x\cdot\vec{n}_v) = \cos(\alpha)$.

In regions of $\{\alpha,\kappa,t_x\}$ space where $2\kappa|\delta| + |t_x| > 2|\tau| + \kappa|\mu|$ (respectively, in regions of $\{\alpha,\kappa,t_v\}$ space where $2|\delta| + \kappa|t_v| > 2\kappa|\tau| + |\mu|$), the original 3-subsequence $\mathsf{V}(\delta)\cdot\mathsf{X}(t_x)\cdot\mathsf{V}(\delta)$ (respectively, $\mathsf{X}(\delta)\cdot\mathsf{V}(t_v)\cdot\mathsf{X}(\delta)$) synthesizing $U^\star$ cannot be time-optimal [68] (**decomposition #2**).

Finally, we explore the symmetries that arise when considering rotations such as $[\mathsf{X}(t_x)\mathsf{V}(t_v)] \equiv \mathsf{M}(\theta)$. $\mathsf{M}(\theta)$ is the effective rotation accomplished by the alternating

controls; it is described by an axis $\vec{n}_m \equiv (m_x, m_y, m_z)$, with

$$m_x(t_x, t_v, \alpha) = \frac{\cos(\alpha)\sin\left(\frac{t_v}{2}\right)\cos\left(\frac{t_x}{2}\right) + \cos\left(\frac{t_v}{2}\right)\sin\left(\frac{t_x}{2}\right)}{\sqrt{1 - \left(\cos\left(\frac{t_v}{2}\right)\cos\left(\frac{t_x}{2}\right) - \cos(\alpha)\sin\left(\frac{t_v}{2}\right)\sin\left(\frac{t_x}{2}\right)\right)^2}} \; ; \tag{4.57}$$

$$m_y(t_x, t_v, \alpha) = \frac{\sin(\alpha)\sin\left(\frac{t_v}{2}\right)\cos\left(\frac{t_x}{2}\right)}{\sqrt{1 - \left(\cos\left(\frac{t_v}{2}\right)\cos\left(\frac{t_x}{2}\right) - \cos(\alpha)\sin\left(\frac{t_v}{2}\right)\sin\left(\frac{t_x}{2}\right)\right)^2}} \; ; \tag{4.58}$$

$$m_z(t_x, t_v, \alpha) = \frac{\sin(\alpha)\sin\left(\frac{t_v}{2}\right)\sin\left(\frac{t_x}{2}\right)}{\sqrt{1 - \left(\cos\left(\frac{t_v}{2}\right)\cos\left(\frac{t_x}{2}\right) - \cos(\alpha)\sin\left(\frac{t_v}{2}\right)\sin\left(\frac{t_x}{2}\right)\right)^2}} \; ; \tag{4.59}$$

and by the angle

$$\theta(t_x, t_v, \alpha) = 2\arccos\left(\cos\left(\frac{t_v}{2}\right)\cos\left(\frac{t_x}{2}\right) - \cos(\alpha)\sin\left(\frac{t_v}{2}\right)\sin\left(\frac{t_x}{2}\right)\right) \; . \tag{4.60}$$

We point out that, if $[\mathsf{X}(t_x) \cdot \mathsf{V}(t_v)]$ has axis (m_x, m_y, m_z) and rotation angle θ, related rotations such as $[\mathsf{V}(t_v) \cdot \mathsf{X}(t_x)]$ are similarly parametrized (see Table 4.2). These relationships allow us to analytically derive alternative decompositions to $U^\star$ composed of three or more consecutive rotations (**decomposition #3**).

rotation	axis	angle
$[\mathsf{X}(t_x) \cdot \mathsf{V}(t_v)]$	(m_x, m_y, m_z)	θ
$[\mathsf{X}(-t_x) \cdot \mathsf{V}(-t_v)]$	$(m_x, m_y, -m_z)$	$-\theta$
$[\mathsf{V}(t_v) \cdot \mathsf{X}(t_x)]$	$(m_x, m_y, -m_z)$	θ
$[\mathsf{V}(-t_v) \cdot \mathsf{X}(-t_x)]$	(m_x, m_y, m_z)	$-\theta$

Table 4.2: **Related rotation parametrizations used for alternative decompositions of a unitary.** Such relationships enable the analytical derivation of unitary alternative decompositions of three or more consecutive rotations.

The simplest example of these alternative decompositions (**decomposition #4**) is obtained by considering that any rotation

$$U^\star = \mathsf{A}(t) \tag{4.61}$$

can be alternatively synthesized up to a global phase as

$$U^\star = \mathsf{B}(t^*) \cdot \mathsf{A}(-t) \cdot \mathsf{B}(t^*) \,, \tag{4.62}$$

with

$$t^* = -2 \operatorname{arccot}\left((\vec{n}_a \cdot \vec{n}_b) \, \tan\left(\frac{t}{2}\right)\right) \,. \tag{4.63}$$

In what follows, necessary bounds on the internal rotation angles and on the maximal length n of time-optimal sequences are presented; they are directly derived by fully analytic procedures adopting the four **decompositions** described above.

■ **Case $t > 0$, $\kappa > \cos(\alpha)$, finite sequences.** Applied to this case, **decomposition #2** implies that 3-sequences or subsequences of type

$$U^\star = \mathsf{V}(t_f) \cdot \mathsf{X}(t_x) \cdot \mathsf{V}(t_i) \tag{4.64}$$

are only time-optimal for $t_x > \pi$. For sequences longer than $n = 3$, $t_x > \pi$ implies that $t_v > \pi$ as well. Similarly, 3-sequences such as

$$U^\star = \mathsf{X}(t_f) \cdot \mathsf{V}(t_v) \cdot \mathsf{X}(t_i) \tag{4.65}$$

are only time-optimal for $t_v > \pi$.

To further bound the allowed t_x and sequence length n, we focus on the case $\kappa = 1$ and show that for some ranges of $\{\alpha, t_x\}$, n and longer finite time-optimal sequences do not exist. While for simplicity we omit details for the case $\kappa \neq 1$, we note that our methods can be extended in a straightforward way to rotations with different implementation speeds. In addition, we observed that, given a sequence of length n, the allowed regions for time-optimal sequences in $\{\alpha, t_x\}$ space expand with increasing κ. Thus, although a formal proof is lacking, the limit $\kappa = 1$ may be taken as a loose bound for the necessary structure of a time-optimal sequence.

A 4-sequence can only be time-optimal in the regions shown in Figure 4-2. There are several ways of deriving this result; one of them is to overlay the regions in $\{\alpha, t_x\}$ space where, concomitantly, $\frac{d^2\mathcal{T}}{d\delta^2} > 0$ and one alternative decomposition of $[\mathsf{X}(t_x) \cdot \mathsf{V}(t_v)]$, for example

$$[\mathsf{X}(t_x) \cdot \mathsf{V}(t_v)] = \mathsf{V}(\theta_3) \cdot \mathsf{Q}(\theta_2) \cdot \mathsf{X}(\theta_1) \text{ (decomposition \#1) ;} \tag{4.66}$$

$$[\mathsf{X}(t_x) \cdot \mathsf{V}(t_v)] = \mathsf{V}(\theta_3) \cdot \mathsf{X}(\theta_2) \cdot \mathsf{V}(\theta_1) \cdot \mathsf{X}(-t_x) \text{ (decompositions \#1,3) ,} \tag{4.67}$$

is synthesized in less time. Here and in the following, negative rotation angles such as $-t_x$ should be interpreted as implemented by physical rotations by the positive angle $2\pi - t_x$. There are two distinct regions in Figure 4-2; while the appearance of the region with $\pi/2 < \alpha < 2\pi/3$ is not intuitive, numerical simulations independently confirm the existence of both disjoint regions. The region for $\alpha < \frac{\pi}{2}$ is given by $t_x \leq t^\dagger$, where $t^\dagger$ is the angle for which $[\mathsf{X}(t^\dagger) \cdot \mathsf{V}(t^\dagger)] = [\mathsf{V}(-t^\dagger) \cdot \mathsf{X}(-t^\dagger)]$; the significance of angles of high sequence symmetry such as $t^\dagger$ will be further explored below.

For orthogonal controls $\alpha = \frac{\pi}{2}$, we remark that finite $n \geq 4$ sequences are never time-optimal; to our knowledge, this is an original proof that time-optimal sequences using orthogonal controls are achieved either with 3-long Euler-like decompositions, or with an infinite concatenation of controls.

Finally, note that the perturbative approach of Section 4.4 had already ruled out $n \geq 4$ or longer finite subsequences for $\alpha > \frac{2\pi}{3}$ as non-optimal.

For longer sequences with $n \geq 5$, two alternative decompositions can be employed based on decompositions #1,3, namely

$$[\mathsf{X}(t_x) \cdot \mathsf{V}(t_v)]^k \cdot \mathsf{X}(t_x) = \mathsf{X}(\theta_3) \cdot [\mathsf{X}(-t_x) \cdot \mathsf{V}(-t_v)]^k \cdot \mathsf{X}(-t_x) \cdot \mathsf{V}(\theta_1) \text{ ,} \tag{4.68}$$

$$[\mathsf{X}(t_x) \cdot \mathsf{V}(t_v)]^k \cdot \mathsf{X}(t_x) = \mathsf{X}(\theta_3) \cdot [\mathsf{X}(-t_x) \cdot \mathsf{V}(-t_v)]^k \cdot \mathsf{X}(-t_x) \cdot \mathsf{X}(\theta_1) \text{ ;} \tag{4.69}$$

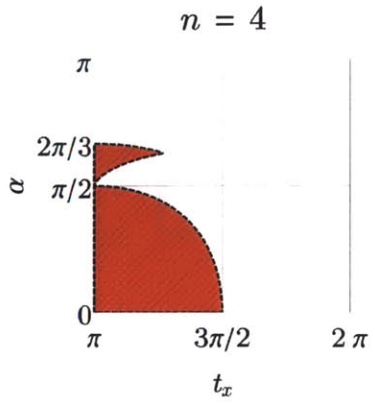

Figure 4-2: **Case $t > 0$, $\kappa > \cos(\alpha)$: optimality of $n = 4$ sequences.** Regions in $\{\alpha, t_x\}$ space where a $n = 4$ sequence can be time-optimal, in the case $\kappa = 1$, are depicted in dashed red. The region for which $\alpha < \frac{\pi}{2}$ is described by $t_x \leq t^\dagger$, with $t^\dagger$ defined as the angle for which $[\mathsf{X}(t^\dagger) \cdot \mathsf{V}(t^\dagger)] = [\mathsf{V}(-t^\dagger) \cdot \mathsf{X}(-t^\dagger)]$.

if n is odd; and, for even n,

$$[\mathsf{X}(t_x) \cdot \mathsf{V}(t_v)]^k = \mathsf{X}(\theta_3) \cdot [\mathsf{V}(-t_v) \cdot \mathsf{X}(-t_x)]^k \cdot \mathsf{X}(\theta_1) \; ; \tag{4.70}$$

$$[\mathsf{X}(t_x) \cdot \mathsf{V}(t_v)]^k = \mathsf{X}(\theta_3) \cdot [\mathsf{X}(-t_x) \cdot \mathsf{V}(-t_v)]^k \cdot \mathsf{V}(\theta_1) \; . \tag{4.71}$$

Using these decompositions, for $\kappa = 1$, we obtain a consistent scaling law for the regions in $\{\alpha, t_x\}$ space where time-optimal sequences of length $n \geq 5$ can exist.

Define the rotation angles $t_{\text{odd},k}, t_{\text{even},k}$ such that

$$[\mathsf{X}(t_{\text{odd},k}) \cdot \mathsf{V}(t_{\text{odd},k})]^k \cdot \mathsf{X}(t_{\text{odd},k}) = [\mathsf{V}(-t_{\text{odd},k}) \cdot \mathsf{X}(-t_{\text{odd},k})]^k \cdot \mathsf{V}(-t_{\text{odd},k}) \; ; \tag{4.72}$$

$$[\mathsf{X}(t_{\text{even},k}) \cdot \mathsf{V}(t_{\text{even},k})]^k = [\mathsf{V}(-t_{\text{even},k}) \cdot \mathsf{X}(-t_{\text{even},k})]^k \; . \tag{4.73}$$

Such angles are explicitly given by

$$t_{\text{odd},k} = 2 \arccos\left(-\sqrt{\frac{\cos(\alpha) - \cos\left(\frac{\pi}{2k+1}\right)}{1 + \cos(\alpha)}} \right) \; ; \tag{4.74}$$

$$t_{\text{even},k} = 2 \arccos\left(-\sqrt{\frac{\cos(\alpha) - \cos\left(\frac{\pi}{2k}\right)}{1 + \cos(\alpha)}} \right) \; . \tag{4.75}$$

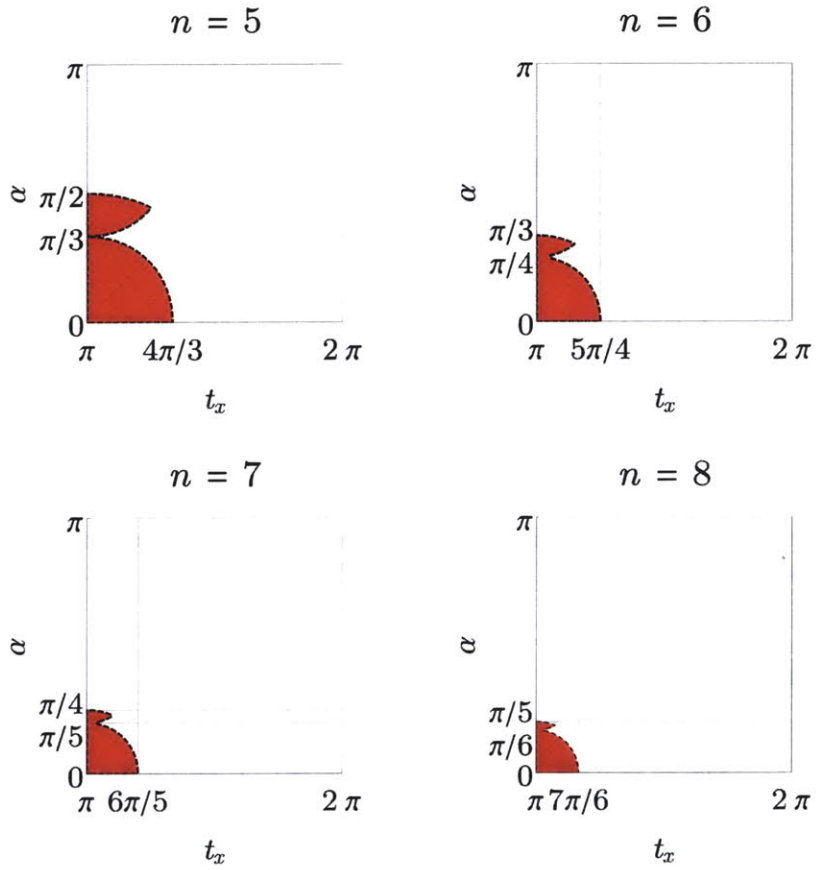

Figure 4-3: **Case $t > 0$, $\kappa > \cos(\alpha)$: scaling laws for optimality of $n \geq 5$ sequences.** Regions in $\{\alpha, t_x\}$ where time-optimal sequences of length $n \geq 5$ can exist, for the particular case $\kappa = 1$, are depicted in dashed red. Note the scaling laws $t_x \leq \frac{(n-1)}{(n-2)}\pi$, and $\alpha \leq \frac{1}{(n-3)}\pi$.

Now, an odd $n = (2k+3)$, $n \geq 5$, time-optimal sequence with middle rotation angle t_x can exist for $t_x \leq t_{\text{odd},k}$ and for a small region such that $t_{\text{odd},k} \leq t_x \leq t_{\text{even},k}$. These relationships are obtained by employing, respectively, Eq. 4.68 and Eq. 4.69.

Similarly, an even $n = (2k+2)$, $n \geq 6$, time-optimal sequence must have the middle rotation angle $t_x \leq t_{\text{even},k}$ or within a small region given by $t_{\text{even},k} \leq t_x \leq t_{\text{odd},(k-1)}$, as obtained from equations Eq. 4.70 and Eq. 4.71 respectively. This situation is depicted in Figure 4-3.

For the particular cases $n = 5, 6$, we could however find tighter bounds using the

following alternative decompositions:

$$\mathsf{X}(t_x)\cdot\mathsf{V}(t_v)\cdot\mathsf{X}(t_x)=\mathsf{V}(\theta_3)\cdot\mathsf{X}(\theta_2)\cdot\mathsf{V}(\theta_1)\ \text{(decomposition \#1)}\ ; \tag{4.76}$$

$$[\mathsf{X}(t_x)\cdot\mathsf{V}(t_v)]^2=\mathsf{V}(\theta_3)\cdot\mathsf{X}(\theta_2)\cdot\mathsf{V}(\theta_1)\cdot\mathsf{X}(-t_x)\ \text{(decompositions \#1,3)}\ . \tag{4.77}$$

These new decompositions completely cut the small disjoint region at higher α (while further constraining the maximal $t_x < t_{\text{even},k}, t_{\text{odd},k}$). The viable smaller regions are plotted in Figure 4-4 against the previous bounds shown in Figure 4-3. Numerical simulations confirm these tighter bounds. Thus, we conjecture that there might be other decomposition of $n \geq 7$ sequences that remove the disjoint region for those longer sequences as well, although this does not appear to be the case for $n = 4$.

To sum up, $n = 4$ time-optimal sequences are bounded by $t_x < \frac{3\pi}{2}$ and $\alpha < \frac{2\pi}{3}$, while for $n \geq 5$ they satisfy $t_x \leq \frac{(n-1)}{(n-2)}\pi$, and $\alpha \leq \frac{\pi}{n-3}$ (with a plausible tighter limit at $\alpha \leq \frac{\pi}{n-2}$).

Inverting the constraints on the admissible regions, $\alpha(n) \rightarrow n(\alpha)$, we find new bounds on the maximum length of a time-optimal sequence:

$$n \leq \lfloor \frac{\pi}{\alpha} \rfloor + 3, \text{ for } n \geq 5\ . \tag{4.78}$$

Note that, especially for small $\alpha \leq \frac{\pi}{3}$, this is a much tighter bound than those previously obtained with index theory [77], which predicts that a finite time-optimal sequence would bear no more than $n \leq \lfloor \frac{2\pi}{\alpha} \rfloor$ control concatenations; and with geometric control [60], which sets $n \leq \lfloor \frac{\pi}{\alpha} \rfloor + 5$.

■ **Case $t > 0, \kappa > \cos(\alpha)$, infinite sequences.** Infinite sequences that are time-optimal must necessarily be of form $\mathsf{X}(t_f)\cdot\mathsf{Q}(t_Q)\cdot\mathsf{V}(t_i)$ or $\mathsf{V}(t_f)\cdot\mathsf{Q}(t_Q)\cdot\mathsf{X}(t_i)$, with $t_q < \pi$.

This result stems from the fact that decomposition #2 imposes that an infinite se-

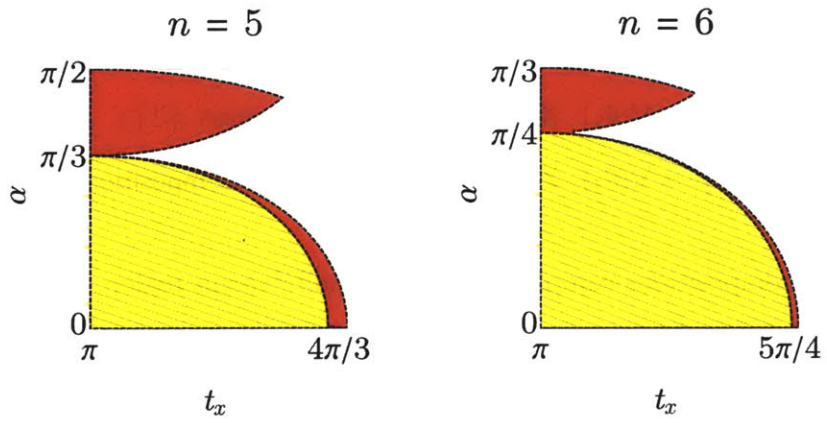

Figure 4-4: **Case $t > 0$, $\kappa > \cos(\alpha)$: tighter bounds on optimality of $n = 5, 6$ sequences.** Stricter regions in $\{\alpha, t_x\}$ space where a $n = 5, 6$ sequence can be time-optimal, in the case $\kappa = 1$, are depicted in fine-dashed yellow; bounds obtained in Figure 4-3 are in dashed red.

quence of the form $\mathsf{A}(t_f) \cdot \mathsf{Q}(t_Q) \cdot \mathsf{A}(t_i)$ can only be optimal for $t_q > \pi$; whereas decomposition #4 requires that an optimal infinite sequence of any form must have $t_q < \pi$. By contradiction, we conclude that an infinite sequence may only be time-optimal in the forms outlined above.

■ Case $t > 0$, $\kappa < \cos(\alpha)$. Decomposition #2 requires that 3 or longer time-optimal sequences have $t_x < \pi$. Note that $t_v(t_x) > \pi$.
Although we cannot simply find further bounds for $n = 4, 5$-long time-optimal sequences, a straightforward application of decomposition #1 constrains $n = 6$ or longer time-optimal sequences to have $t_x > \frac{\pi}{3}$. Additionally, using the same decomposition we find that, if $\alpha > \min\{\frac{\pi}{1+k}, \arccos(\kappa)\}$, an $n = (2k+2), (2k+3)$ sequence, with $k \geq 2$, cannot be time-optimal.

Hence, if $\frac{\pi}{1+k} \leq \arccos(\kappa)$, one can place a bound on the maximal length of a time-optimal sequence:

$$n \leq \lfloor \frac{2\pi}{\alpha} \rfloor + 1, \text{ for } n \geq 6 \,. \tag{4.79}$$

■ **Case $t \lesseqgtr 0$, finite sequences.** Bounds on the maximal length of a finite time-optimal sequence are readily obtained. In particular, for all $n \geq 6$ finite time-optimal sequences, there is always at least one alternative decomposition, $\forall\, \kappa$, that synthesizes the same unitary in a shorter time. For example, considering a 4-subsequence of a $n \geq 6$ sequence, the unitary realized by the inner rotations such as

$$U^\star = \mathsf{X}(+t_x) \cdot [\mathsf{V}(+t_v) \cdot \mathsf{X}(-t_x)] \cdot \mathsf{V}(-t_v) \tag{4.80}$$

has alternative decompositions:

$$U^\star = \mathsf{V}(\theta_3) \cdot \mathsf{X}(\theta_2) \cdot \mathsf{V}(\theta_1) \text{ (decomposition \#1) ;} \tag{4.81}$$

$$U^\star = \mathsf{X}(+t_x) \cdot (\mathsf{V}(\theta_3) \cdot [\mathsf{X}(+t_x) \cdot \mathsf{V}(-t_v)] \cdot \mathsf{V}(\theta_1)) \cdot \mathsf{V}(-t_v) \text{ (decompositions \# 1,3) ;} \tag{4.82}$$

$$U^\star = \mathsf{X}(+t_x) \cdot (\mathsf{X}(\theta_3) \cdot [\mathsf{V}(-t_v) \cdot \mathsf{X}(+t_x)] \cdot \mathsf{V}(\theta_1)) \cdot \mathsf{V}(-t_v) \text{ (decompositions \# 1,3) ,} \tag{4.83}$$

with at least one of the above having a lower total synthesis time, in all regions of $\{\alpha, \kappa, t_x\}$ space.

We thus proved the important result that, for $t \lesseqgtr 0$, time-optimal sequences must be $n \leq 5$ long, or infinite.

This conclusion is stronger than previously published bounds establishing that every time-optimal trajectory is a finite concatenation of at most five bang-bang or singular arcs [73], in that our results rule out, for example, the existence of a time-optimal sequence of type $\mathsf{A}(t_5) \cdot \mathsf{B}(t_4) \cdot \mathsf{Q}(t_3) \cdot \mathsf{B}(t_2) \cdot \mathsf{A}(t_1)$.

For this case, we can further characterize the admissible time-optimal sequences and impose stricter constraints on their times. 3-sequences or subsequences of type

$$U^\star = \mathsf{X}(t_f) \cdot \mathsf{V}(t_v) \cdot \mathsf{X}(t_i) \tag{4.84}$$

must, according to **decomposition #2**, have $\mathrm{sgn}(t_f) \neq \mathrm{sgn}(t_i)$ and $|t_v| < 2\arccos\left(\frac{\kappa|\cos(\alpha)|}{1+\kappa|\cos(\alpha)|}\right)$. 3-sequences or subsequences of type

$$U^\star = \mathsf{V}(t_f) \cdot \mathsf{X}(t_x) \cdot \mathsf{V}(t_i) \ , \tag{4.85}$$

must, in turn, obey $\mathrm{sgn}(t_f) \neq \mathrm{sgn}(t_i)$ and $|t_x| < 2\arccos\left(\frac{|\cos(\alpha)|}{\kappa+|\cos(\alpha)|}\right)$. Time-optimal sequences of this type which are exactly $n = 3$ long may also have $\mathrm{sgn}(t_f) = \mathrm{sgn}(t_i)$; if so, $|t_x| < 2\arccos\left(\frac{\cos(\alpha)-\kappa}{\cos(\alpha)+\kappa}\right)$ should hold.

Applying **decomposition #4** to the two possible inner subsequences of a 5-long time-optimal sequence, namely

$$U^\star = \mathsf{V}(-t_v) \cdot \mathsf{X}(t_x) \cdot \mathsf{V}(t_v) \ ; \tag{4.86}$$

$$U^\star = \mathsf{X}(-t_x) \cdot \mathsf{V}(t_v) \cdot \mathsf{X}(t_x) \ , \tag{4.87}$$

we conclude that $|t_x| < 2\,\mathrm{arccot}\left(\frac{1}{\kappa}\right)$ in the first case, and $|t_x| < \frac{\pi}{2}$ in the second.

■ **Case $t \lesseqgtr 0$, infinite sequences.** Because of the sign structure imposed on time-optimal sequences for this case, some forms of infinite sequences can be ruled out.

Infinite time-optimal sequences can then take only one of the following shapes: $\mathsf{X}(t_f) \cdot \mathsf{Q}(t_Q) \cdot \mathsf{V}(t_i)$, $\mathsf{V}(t_f) \cdot \mathsf{Q}(t_Q) \cdot \mathsf{X}(t_i)$, with $\mathrm{sgn}(t_i) = \mathrm{sgn}(t_f) = \mathrm{sgn}(t_Q)$; or $\mathsf{A}(t_f) \cdot \mathsf{P}(t_P) \cdot \mathsf{B}(t_i)$, with $\mathrm{sgn}(t_i) \neq \mathrm{sgn}(t_f)$. In the latter case, if $\mathsf{A}(\cdot) = \mathsf{B}(\cdot) = \mathsf{X}(\cdot)$ (respectively, $\mathsf{A}(\cdot) = \mathsf{B}(\cdot) = \mathsf{V}(\cdot)$), according to **decomposition #4**, $|t_p| < \frac{2\pi}{3}$ ($|t_p| < 2\arccos\left(\frac{\kappa}{1+\kappa}\right)$).

4.6 Bounds on outer rotation angles

Using the same methods as those outlined in Section 4.5, outer rotation angles can also be constrained. We denote those angles $t_{x,\text{out}}$ ($t_{v,\text{out}}$) if

$$U_{\text{goal}} = \mathsf{X}(t_{x,\text{out}}) \cdot \ \ldots \ \text{ or } \ U_{\text{goal}} = \ \ldots \ \cdot \mathsf{X}(t_{x,\text{out}}) \ . \tag{4.88}$$

■ **Case $t > 0$, $\kappa > \cos(\alpha)$.** For any $n \geq 4$ sequence, we find loose bounds for the outer times by employing **decomposition #4**.

For $\alpha > \frac{\pi}{2}$, we have $t_{x,\text{out}}, t_{v,\text{out}} < \pi$; for $\alpha < \frac{\pi}{2}$, we obtain $t_{x,\text{out}} < 2\pi + 2\,\text{arccot}\left(\cos(\alpha)\tan\left(\frac{t_v}{2}\right)\right)$ and, similarly, $t_{v,\text{out}} < 2\pi + 2\,\text{arccot}\left(\cos(\alpha)\tan\left(\frac{t_x}{2}\right)\right)$. Note that these last two bounds are tighter than the simpler bounds $t_{\{x,v\},\text{out}} < 3\pi - t_{\{v,x\}}$.

■ **Case $t \lesseqgtr 0$.** When applied to 3-subsequences such as

$$U^\star = \mathsf{V}(-t_{v,\text{out}}) \cdot \mathsf{X}(t_x) \cdot \mathsf{V}(t_v) \ , \tag{4.89}$$

decomposition #4 dictates that $|t_{\{x,v\},\text{out}}| < \pi - |t_{\{x,v\}}|$. Similarly, for a 4-sequence to be time-optimal, $|t_{v,\text{out}}| + |t_{x,\text{out}}| < \frac{2\pi}{3}$; this bound is further tightened for a 5-sequence, for which either $|t_{v,\text{out}}| < t_v$, $|t_{x,\text{out}}| < t_x$ or $|t_{v,\text{out}}|, |t_{x,\text{out}}| < \frac{\pi}{3}$ (whichever is tighter).

4.7 Summary of results

We present a summary of the derived necessary conditions for time-optimal sequences of length $3 \leq n \leq \infty$. As with the rest of this work, the results are subdivided by cases.

■ **Case $t > 0$.** Time-optimal sequences only depend on four parameters, namely

the outer angles t_i, t_f, the internal angle t_x (or t_v or t_q), and the total number of rotations $n \leq \infty$. In this case, if $n \geq 4$, the internal angles are related by Eq. 4.33,

$$\tan\left(\frac{t_v}{2}\right) = \tan\left(\frac{t_x}{2}\right) \cdot \frac{\kappa - \cos(\alpha)}{1 - \kappa\cos(\alpha)} \ . \tag{4.33}$$

Admissible time-optimal sequences and their derived bounds are summarized in Table 4.3 for $\kappa > \cos(\alpha)$, and in Table 4.4 for $\kappa < \cos(\alpha)$. All angles $t \in [0, 2\pi[$.

We can further provide bounds on the maximum total time $\mathcal{T}_{\max}$ required for a finite time-optimal sequence.

For the case $\kappa > \cos(\alpha)$, noting that

$$\max(t_x + t_v) = 2\pi + \frac{(n-1)}{(n-2)}\pi = \frac{(3n-5)}{(n-2)}\pi \ ; \tag{4.90}$$

$$\max(t_{x,\text{out}} + t_v) = \pi(2+\kappa) \ ; \tag{4.91}$$

$$\max(t_{v,\text{out}} + t_x) = \pi(1+2\kappa) \ , \tag{4.92}$$

we establish the following:

- For n odd and outer controls X, $\mathcal{T}_{\max} = 2\pi(2+\kappa) + \mathbb{1}_{n>3} \cdot \left(\frac{(n-5)}{2}\frac{(3n-5)}{(n-2)}\pi + \frac{(n-1)}{(n-2)}\pi\right)$;
- For n odd and outer controls V, $\mathcal{T}_{\max} = 2\pi(1+2\kappa) + \mathbb{1}_{n>3} \cdot \left(\frac{(n-5)}{2}\frac{(3n-5)}{(n-2)}\pi + 2\pi\kappa\right)$;
- For $n \geq 4$ even, $\mathcal{T}_{\max} = 3\pi(1+\kappa) + \frac{(n-4)}{2}\frac{(3n-5)}{(n-2)}\pi$.

Similarly, for $\kappa < \cos(\alpha)$, given

$$\max(t_x + t_v) = 3\pi \ , \tag{4.93}$$

the maximum times follow:

- For n odd and outer controls X, $\mathcal{T}_{\max} = 2\pi(2+\kappa) + \frac{(n-3)}{2}3\pi$;
- For n odd and outer controls V, $\mathcal{T}_{\max} = \pi(1+4\kappa) + \frac{(n-3)}{2}3\pi$;

- For $n \geq 4$ even, $\mathcal{T}_{\max} = 2\pi(1+\kappa) + \frac{(n-2)}{2} 3\pi$.

We note that these are quite loose bounds, since they are obtained by combining bounds on all free parameters; they might still be of guidance when designing practical experiments.

■ **Case $t \lesseqgtr 0$.** Time-optimal sequences only depend on four parameters, namely the outer angles t_i, t_f, the internal angle t_x (or t_v or t_q), and the total number of rotations. All angles $t \in [-\pi, \pi]$. It holds that either $n \leq 5$, or $n \to \infty$; moreover, the relative signs of the rotation angles are restricted to a few combinations. If $n \geq 4$, internal angles are related by Eq. 4.37,

$$\tan\left(\frac{t_v}{2}\right) = \pm \tan\left(\frac{t_x}{2}\right) \cdot \frac{1}{\kappa} \tag{4.37}$$

in finite sequences; and, in infinite sequences, by Eqs. 4.41 and 4.42,

$$\tan\left(\frac{t_v}{2}\right) = \tan\left(\frac{t_x}{2}\right) \cdot \frac{\kappa - \cos(\alpha)}{1 - \kappa\cos(\alpha)} \; ; \tag{4.41}$$

$$\tan\left(\frac{t_v}{2}\right) = -\tan\left(\frac{t_x}{2}\right) \cdot \frac{\kappa + \cos(\alpha)}{1 + \kappa\cos(\alpha)} \; . \tag{4.42}$$

Admissible time-optimal sequences and their derived bounds are summarized in Table 4.5. All angles $t \in]-\pi, \pi]$. These bounds further provide constraints on the total time of an optimal unitary synthesis. Analogously as above, the maximal total time $\mathcal{T}_{\max}$ for a finite time-optimal sequence can be estimated:

- For $n = 3$ and outer controls X, $\mathcal{T}_{\max} = \pi(4+\kappa)$;
- For $n = 3$ and outer controls V, $\mathcal{T}_{\max} = \pi(1+4\kappa)$;
- For $n = 4$, $\mathcal{T}_{\max} = \pi(1+\kappa)$;
- For $n = 5$ and outer controls X, $\mathcal{T}_{\max} = \frac{13\pi}{6} + \pi\kappa$;
- For $n = 5$ and outer controls V, $\mathcal{T}_{\max} = 2\pi + \frac{2\pi}{3}\kappa$.

n	α range	type	internal angle	outer angles
3	$\alpha < \pi$	$\mathsf{V}(t_f) \cdot \mathsf{X}(t_x) \cdot \mathsf{V}(t_i)$	$\pi < t_x$	
		$\mathsf{X}(t_f) \cdot \mathsf{V}(t_v) \cdot \mathsf{X}(t_i)$	$\pi < t_v$	
4	$\alpha \leq \frac{2\pi}{3}$	$\mathsf{V}(t_f) \cdot [\mathsf{X}(t_x) \cdot \mathsf{V}(t_v)] \cdot \mathsf{X}(t_i)$	$\pi < t_x < \frac{3\pi}{2}$	$\begin{cases} t_i, t_f < \pi \text{ if } \alpha > \frac{\pi}{2} \ (n = 4 \text{ only}) \\ t_{x,\text{out}} < 3\pi - t_v, \\ t_{v,\text{out}} < 3\pi - t_x \text{ if } \alpha < \frac{\pi}{2} \end{cases}$
		$\mathsf{X}(t_f) \cdot [\mathsf{V}(t_v) \cdot \mathsf{X}(t_x)] \cdot \mathsf{V}(t_i)$		
$4 < n \leq \lfloor \frac{\pi}{\alpha} \rfloor + 3$	$\alpha \leq \frac{\pi}{n-3}$	$\mathsf{V}(t_f) \cdot [\mathsf{X}(t_x) \cdot \mathsf{V}(t_v)]^k \cdot \mathsf{X}(t_x) \cdot \mathsf{V}(t_i), \ k \geq 1$	$\pi < t_x \leq \frac{(n-1)}{(n-2)}\pi$	
		$\mathsf{V}(t_f) \cdot [\mathsf{X}(t_x) \cdot \mathsf{V}(t_v)]^k \cdot \mathsf{X}(t_i), \ k \geq 2$		
		$\mathsf{X}(t_f) \cdot [\mathsf{V}(t_v) \cdot \mathsf{X}(t_x)]^k \cdot \mathsf{V}(t_v) \cdot \mathsf{X}(t_i), \ k \geq 1$		
		$\mathsf{X}(t_f) \cdot [\mathsf{V}(t_v) \cdot \mathsf{X}(t_x)]^k \cdot \mathsf{V}(t_i), \ k \geq 2$		
∞	$\arccos(\kappa) < \alpha < \pi$	$\mathsf{V}(t_f) \cdot \mathsf{Q}(t_Q) \cdot \mathsf{X}(t_i)$	$t_q < \pi$	
		$\mathsf{X}(t_f) \cdot \mathsf{Q}(t_Q) \cdot \mathsf{V}(t_i)$		

Table 4.3: **Admissible structures of time-optimal sequences, case $t > 0$, $\kappa > \cos(\alpha)$.**

n	α range	type	internal angle
3	$0 < \alpha < \arccos(\kappa)$	$\mathsf{V}(t_f) \cdot \mathsf{X}(t_x) \cdot \mathsf{V}(t_i)$	$t_x < \pi$
		$\mathsf{X}(t_f) \cdot \mathsf{V}(t_v) \cdot \mathsf{X}(t_i)$	$\pi < t_v$
4		$\mathsf{V}(t_f) \cdot [\mathsf{X}(t_x) \cdot \mathsf{V}(t_v)] \cdot \mathsf{X}(t_i)$	$t_x < \pi$
		$\mathsf{X}(t_f) \cdot [\mathsf{V}(t_v) \cdot \mathsf{X}(t_x)] \cdot \mathsf{V}(t_i)$	
5		$\mathsf{V}(t_f) \cdot [\mathsf{X}(t_x) \cdot \mathsf{V}(t_v)] \cdot \mathsf{X}(t_x) \cdot \mathsf{V}(t_i)$	
		$\mathsf{X}(t_f) \cdot [\mathsf{V}(t_v) \cdot \mathsf{X}(t_x)] \cdot \mathsf{V}(t_v) \cdot \mathsf{X}(t_i)$	
$6 \leq n < \infty$	$\alpha \leq \min\{\frac{\pi}{1+k}, \arccos(\kappa)\}$	$\mathsf{V}(t_f) \cdot [\mathsf{X}(t_x) \cdot \mathsf{V}(t_v)]^k \cdot \mathsf{X}(t_i), \ k \geq 2$	$\frac{\pi}{3} < t_x < \pi$
		$\mathsf{V}(t_f) \cdot [\mathsf{X}(t_x) \cdot \mathsf{V}(t_v)]^k \cdot \mathsf{X}(t_x) \cdot \mathsf{V}(t_i), \ k \geq 2$	
		$\mathsf{X}(t_f) \cdot [\mathsf{V}(t_v) \cdot \mathsf{X}(t_x)]^k \cdot \mathsf{V}(t_i), \ k \geq 2$	
		$\mathsf{X}(t_f) \cdot [\mathsf{V}(t_v) \cdot \mathsf{X}(t_x)]^k \cdot \mathsf{V}(t_v) \cdot \mathsf{X}(t_i), \ k \geq 2$	

Table 4.4: **Admissible structures of time-optimal sequences, case $t > 0$, $\kappa < \cos(\alpha)$.**

n	α range	type	signs	internal angle	outer angles
3	$\alpha < \pi$	$\mathsf{V}(t_f)\mathsf{X}(t_x)\mathsf{V}(t_i)$	$\operatorname{sgn}(t_f) \neq \operatorname{sgn}(t_i)$	$\lvert t_x\rvert < 2\arccos\left(\frac{\lvert\cos(\alpha)\rvert}{\kappa+\lvert\cos(\alpha)\rvert}\right)$	
		$\mathsf{V}(t_f)\mathsf{X}(t_x)\mathsf{V}(t_i)$	$\operatorname{sgn}(t_f) = \operatorname{sgn}(t_i)$	$\lvert t_x\rvert < 2\arccos\left(\frac{\cos(\alpha)-\kappa}{\cos(\alpha)+\kappa}\right)$	
		$\mathsf{X}(t_f)\mathsf{V}(t_v)\mathsf{X}(t_i)$	$\operatorname{sgn}(t_f) \neq \operatorname{sgn}(t_i)$	$\lvert t_v\rvert < 2\arccos\left(\frac{\kappa\lvert\cos(\alpha)\rvert}{1+\kappa\lvert\cos(\alpha)\rvert}\right)$	
4		$\mathsf{V}(t_f)[\mathsf{X}(t_x)\mathsf{V}(t_v)]\mathsf{X}(t_i)$	$\{+,+,-,-\}$	$\lvert t_x\rvert < 2\arccos\left(\frac{\lvert\cos(\alpha)\rvert}{\kappa+\lvert\cos(\alpha)\rvert}\right)$	$\begin{cases} \lvert t_{x,\text{out}}\rvert < \pi - \lvert t_x\rvert \\ \lvert t_{v,\text{out}}\rvert < \pi - \lvert t_v\rvert \\ \lvert t_{x,\text{out}}\rvert + \lvert t_{v,\text{out}}\rvert < \frac{2\pi}{3} \end{cases}$
		$\mathsf{V}(t_f)[\mathsf{X}(t_x)\mathsf{V}(t_v)]\mathsf{X}(t_i)$	$\{-,+,+,-\}$		
		$\mathsf{X}(t_f)[\mathsf{V}(t_v)\mathsf{X}(t_x)]\mathsf{V}(t_i)$	$\{+,+,-,-\}$		
		$\mathsf{X}(t_f)[\mathsf{V}(t_v)\mathsf{X}(t_x)]\mathsf{V}(t_i)$	$\{-,+,+,-\}$		
5		$\mathsf{V}(t_f)[\mathsf{X}(t_x)\mathsf{V}(t_v)]\mathsf{X}(t_x)\mathsf{V}(t_i)$	$\{+,+,-,-,+\}$	$\lvert t_x\rvert < \frac{\pi}{2}$	$\begin{cases} \lvert t_{x,\text{out}}\rvert < \min\{\lvert t_x\rvert, \frac{\pi}{3}\} \\ \lvert t_{v,\text{out}}\rvert < \min\{\lvert t_v\rvert, \frac{\pi}{3}\} \end{cases}$
		$\mathsf{V}(t_f)[\mathsf{X}(t_x)\mathsf{V}(t_v)]\mathsf{X}(t_x)\mathsf{V}(t_i)$	$\{-,+,+,-,+\}$		
		$\mathsf{X}(t_f)[\mathsf{V}(t_v)\mathsf{X}(t_x)]\mathsf{V}(t_v)\mathsf{X}(t_i)$	$\{+,+,-,-,+\}$	$\lvert t_x\rvert < 2\operatorname{arccot}\left(\frac{1}{\kappa}\right)$	
		$\mathsf{X}(t_f)[\mathsf{V}(t_v)\mathsf{X}(t_x)]\mathsf{V}(t_v)\mathsf{X}(t_i)$	$\{+,-,-,+,+\}$		
∞	$\arccos(\kappa) < \alpha < \pi$	$\mathsf{V}(t_f)\mathsf{Q}(t_Q)\mathsf{X}(t_i)$	$\{+,+,+\}$		
		$\mathsf{X}(t_f)\mathsf{Q}(t_Q)\mathsf{V}(t_i)$	$\{+,+,+\}$		
	$\alpha < \pi - \arccos(\kappa)$	$\mathsf{V}(t_f)\mathsf{P}(t_P)\mathsf{V}(t_i)$	$\operatorname{sgn}(t_f) \neq \operatorname{sgn}(t_i)$	$\lvert t_p\rvert < 2\arccos\left(\frac{\kappa}{1+\kappa}\right)$	
		$\mathsf{X}(t_f)\mathsf{P}(t_P)\mathsf{X}(t_i)$	$\operatorname{sgn}(t_f) \neq \operatorname{sgn}(t_i)$	$\lvert t_p\rvert < \frac{2\pi}{3}$	
		$\mathsf{V}(t_f)\mathsf{P}(t_P)\mathsf{X}(t_i)$	$\operatorname{sgn}(t_f) \neq \operatorname{sgn}(t_i)$		
		$\mathsf{X}(t_f)\mathsf{P}(t_P)\mathsf{V}(t_i)$	$\operatorname{sgn}(t_f) \neq \operatorname{sgn}(t_i)$		

Table 4.5: **Admissible structures of time-optimal sequences, case $t \gtrless 0$.** The shown sign combinations are relative, that is, the sequences remain admissible under a global sign change.

4.8 Applications

The restricted control set that was studied in the preceding Sections is of relevance in many electron-nuclear spin systems exhibiting anisotropic hyperfine couplings, for example: a ^{13}C proximal to an NV center in diamond [27, 63, 78]; a proton coupled to a free electron in malonic acid [64, 79, 80]; ^{31}P in P donors in Si [81]; N in buckyballs [82]; and other quantum compounds studied in nuclear magnetic resonance [83]. For such systems, the nuclear evolution can be steered via the switching of the actuator-electronic spin, in a generally faster and noise-free way, as compared to the direct addressing of the nuclear spin.

Specifically for the coupled qubits in diamond, we will shown in Chapter 5 that this actuator protocol for driving the ^{13}C nuclear spin is in general advantageous over radio-frequency direct driving.

Additionally, the same control set is used to model machine motion such as satellite reorientation [60, 65], so that we believe our results will be of interest to the robotics community as well.

4.9 Conclusion

In conclusion, we have addressed the problem of time-optimal generation of $SU(2)$ unitaries through concatenations of elementary rotations about two non-parallel, and generally non-orthogonal, axes. We have algebraically derived the necessary general structure of time-optimal sequences, and shown that such sequences are described solely in terms of three independent parameters representing rotation angles, and the total number of rotations n. Bounds for such parameters were found, as a function of the angle between the rotation axes, α, and a parameter describing the difference in effective implementation cost of the rotations, κ. Given the experimentally relevant

α, κ, in certain cases we can also predict the maximal number of rotations n in a time-optimal sequence.

Our method maps an optimization problem involving differential equations into a much simpler, algebraic linear problem. While our analysis starts from abstract mathematical results in optimal control theory, we go beyond previous literature in providing the experimental physicist with a general set of instructions to find the time-optimal operations in a large set of realistic experimental conditions. While these instructions are in general not sufficient to single out the time-optimal sequence for the desired unitary, they provide a very powerful set of rules that constrains the structure of time-optimal solutions so strongly, that the solution can be found through a simple numerical search.

The key interest of our results stems from their wide applicability to quantum systems with a restricted control set. In particular, we foresee fast unitary control of a nuclear spin by switching the spin states of an electronic spin, if the hyperfine interaction is anisotropic. This setting occurs, for example, in a proximal ^{13}C coupled to a NV center in diamond, case which will be explored in great detail in Chapter 5.

Furthermore, outside quantum science, the very general control problem we address will be of interest in diverse fields of physics and engineering, for instance robotics; the accessible approach we employ, and the power of the general results and insights into the structure of time-optimal sequences it provides, are bound to become an invitation to the physicist un-initiated in theoretical control methods.

Chapter 5

Time-optimal algebraic $SU(2)$ synthesis with alternating controls: application

We propose to use alternating controls, in the same framework as developed in Chapter 4, to drive the evolution of a nuclear spin anisotropically hyperfine-coupled to an electronic spin [64, 78]; in particular, we numerically show that periodically driving the spin of a NV center in diamond can steer the evolution of a proximal ^{13}C nuclear spin in a potentially shorter time than a direct, slow radio-frequency addressing.

In general, the method ensures the use of the nuclear spin as a resource within the same implementation time-range of direct addressing, while entirely by-passing the application of radio-frequency, and thus reducing the strong noise component associated with it.

5.1 Actuator driving protocol

Upon flipping of the NV electronic spin, a proximal hyperfine-coupled ^{13}C nuclear spin has both its quantization axis and Larmor frequency altered. Let the nuclear Larmor

frequency $\omega_0 = \gamma B_0$, with gyromagnetic ratio $\gamma \sim 1\text{kHz/G}$, when the electronic spin is in its magnetic sublevel $m_s = |0\rangle$ state; in this case, an external magnetic field B_0 aligned with the axis connecting the nitrogen and vacancy in the crystal lattice provides a definite quantization axis for both electronic and nuclear spins. With an electronic spin flip to $m_s = |\pm 1\rangle$, contact and dipolar contributions from the hyperfine interaction change the nuclear Larmor frequency to $\omega_{\pm 1} = \sqrt{(\omega_0 \pm \mathcal{A})^2 + \mathcal{B}^2}$. Similarly, and following the nomenclature of Chapter 4, the angle between the different quantization axes of the nuclear spin is $\alpha = \arctan\left(\frac{\mathcal{B}}{\omega_0 \pm \mathcal{A}}\right)$. Here, $\mathcal{B}, \mathcal{A}$ are, respectively, the anisotropic and isotropic components of the hyperfine interaction. Finally, it follows that we can express the parameter $\kappa = \frac{\omega_0}{\omega_{\pm 1}}$. As previously mentioned, since the nuclear evolution can be arbitrarily steered by means of the hyperfine interaction, we refer to the electronic spin as an actuator.

The experimental system is such that only the case of positive rotation angles is of relevance here. Within this case, both regimes $\kappa \lesseqgtr \cos(\alpha)$ can be explored considering the coupling to ^{13}C at different distances from the NV defect [35, 84]. The hyperfine tensors for ^{13}C located up to ~ 8Å away from the NV center were estimated using density functional theory [85]. In what follows, we numerically compare the performance of the actuator protocol against direct driving (using radio-frequency fields) under diverse experimental conditions and $\{\alpha, \kappa\}$ values.

5.2 Direct driving of the nuclear spin: considerations

The strength of the direct driving of the nuclear spin depends on the state of the hyperfine-coupled electronic spin [86]; the effective Rabi frequency Ω delivered by the radio-frequency to an isolated nuclear spin, hence, is modified by the hyperfine coupling, $\Omega \to |\zeta_{0,\pm 1}| \cdot \Omega$. Here, the enhancement factors $\zeta_{0,\pm 1}$ for the electronic spin

states $|0\rangle, |\pm 1\rangle$, to first order in the magnetic field, read:

$$\zeta_0 = 1 + \frac{4\gamma_e \mathcal{B}(\mathcal{A}-\Delta)}{\gamma_n(\mathcal{A}-\Delta+B_0(\gamma_e-\gamma_n))(\mathcal{A}-\Delta-B_0(\gamma_e-\gamma_n))} ; \quad (5.1)$$

$$\zeta_{+1} = 1 - \frac{2\gamma_e \mathcal{B}}{\gamma_n(\mathcal{A}-\Delta-B_0(\gamma_e-\gamma_n))} ; \quad (5.2)$$

$$\zeta_{-1} = 1 - \frac{2\gamma_e \mathcal{B}}{\gamma_n(\mathcal{A}-\Delta+B_0(\gamma_e-\gamma_n))} . \quad (5.3)$$

In the above, $\gamma_e \sim 2.8$MHz/G is the gyromagnetic ratio of the electronic spin, and $\Delta \sim 2.87$GHz its zero-field splitting. Note that ζ_i can be either positive or negative, and $\lesseqgtr 1$.

We evaluate $\Omega \sim 83$kHz as an upper-limit on realistic bare nuclear Rabi frequencies by considering experimental conditions in [87]. For the reported parameters $B_0 \sim 250$G and $\overline{\overline{\zeta}} \cdot \Omega \sim 100$kHz, we estimate $\overline{\overline{\zeta}} \equiv \overline{\frac{1}{3}(\zeta_0+\zeta_{+1}+\zeta_{-1})} \sim 1.21$ as an average enhancement factor considering all ^{13}C, bar the three ^{13}C that can occupy the adjacent lattice position to a NV defect ('first shell'), which have enhancement factors typically one order of magnitude larger than those of other nuclear spins.

5.3 Realistic comparison between actuator and direct driving times

We numerically search for sequences $U^\star$ generating a desired U_{goal}. The search is successful (by definition) when the fidelity $F \equiv \frac{1}{2}|\text{tr}(U^\star \cdot U_{\text{goal}}^\dagger)| = 1$ up to $\sim 10^{-10}$, typically yielding $||U^\star \pm U_{\text{goal}}|| \sim 10^{-4}$. We choose the sequence with minimal time cost among all sequences obtained by successful searches (while noting that it does not necessarily attain global time-optimality).

Firstly, the case $\kappa < \cos(\alpha)$ is illustrated in Figure 5-1 by a ^{13}C at a radial distance of ~ 2.92Å from the NV center, at an external magnetic field $B_0 \sim 500$G

aligned with the $\vec{n}_x$ axis. Here, the hyperfine interaction is confined to the $\{\vec{n}_x, \vec{n}_y\}$ plane, $\mathcal{A} \sim 1.98$MHz, $\mathcal{B} \sim 0.51$MHz, $\kappa \sim 0.20$, $\alpha \sim 11.6^o$, $\zeta_0 \sim -1.43$, $\zeta_{+1} \sim 1.62$ and $\zeta_{-1} \sim 2.81$. We have previously established that, for $\kappa < \cos(\alpha)$, time-optimal sequences must be finite, with their maximum length being $n \leq \lfloor \frac{2\pi}{\alpha} \rfloor + 1 = 32$ as derived in Chapter 5. We use uniquely the relationship between internal times given by Eq. 4.33 for $n \geq 4$ sequences, and the stricter bound $\frac{\pi}{3} < t_x < \pi$ for $n \geq 6$ sequences.

Simulation results indicate that, given a goal rotation angle t, the actuator implementation time for rotations around any axis in the $\{\vec{n}_y, \vec{n}_z\}$ plane are comparable, with a maximum around $t \sim \pi$, and a symmetry for $t \pm \tau$, $\forall\ \tau$. We plot in the leftmost (rightmost) panel, in blue circles (diamonds), in particular, the simulated actuator times for generation of the goal unitary $\mathsf{Y}(t_y)$ ($\mathsf{Z}(t_z)$) as a function of the goal rotation angle. The green shaded area represents, in comparison, the fastest direct driving times (that is, for electronic spin state $|-1\rangle$) for the same unitaries, over a range of realistic bare Rabi frequencies from $\Omega \sim 20 - 83$kHz; bare Rabi frequencies $\Omega \sim 20$kHz are, in our experience, in the upper achievable range with modest amplifiers. Note that for bare Rabi frequencies weaker than ~ 20kHz, the actuator protocol is advantageous for any rotation angle. The auxiliary axis to the right indicates the length of the numerically found time-optimal sequence with red crosses.

In Figure 5-2, we examine the driving of a ^{13}C at a radial distance of ~ 2.49Å from the NV center, for which $\mathcal{A} \sim -0.1$MHz and $\mathcal{B} \sim 0.39$MHz. Under the same magnetic field conditions, namely $B_0 \sim 500$G, we have $\kappa \sim 0.90$, $\alpha \sim 44.5^o$, and thus $\kappa > \cos(\alpha)$, with the maximal possible length of a finite time-optimal sequence being $n = 7$. In the leftmost (rightmost) panel, in the left axis we plot the numerically simulated actuator implementation time for the unitary $\mathsf{Y}(t_y)$ as a function of the rotation angle t_y ($\mathsf{Z}(t_z)$ as a function of t_z) using blue circles (diamonds). In the leftmost panel, we compare the time of the actuator protocol to the direct driving with the upper-limit bare Rabi frequency $\Omega \sim 83$kHz, for the three different electronic spin states $|0\rangle, |+1\rangle, |-1\rangle$ (dashed-dot, dashed, and dotted green lines); in the right-

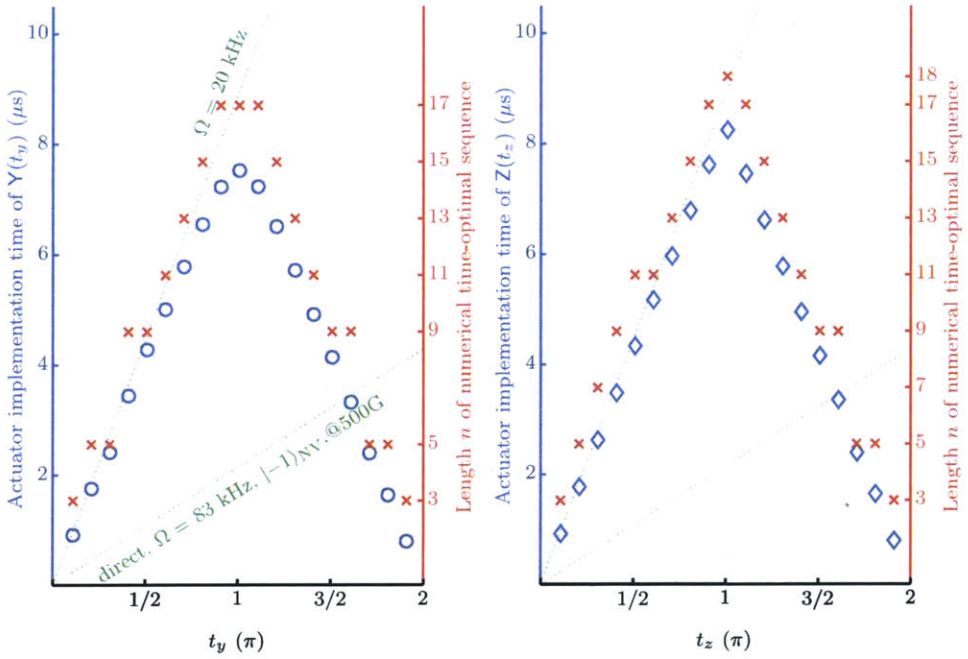

Figure 5-1: **Simulated actuator and driving times for realistic case $\kappa < \cos(\alpha)$.** This case occurs, for example, for a ^{13}C at a radial distance of ~ 2.92Å from the NV center, with an external magnetic field $B_0 \sim 500$G aligned with the $\vec{n}_x$ axis. The simulated actuator implementation time of the unitaries $\mathsf{Y}(t_y)$ and $\mathsf{Z}(t_z)$ are plotted as a function of the goal rotation angle $t_{y,z}$ (in blue circles and diamonds, respectively). The green shaded area represents the direct driving times of the nuclear spin for Rabi frequencies between $20 - 83$kHz, when the electronic spin in state $|-1\rangle$, thus maximizing the enhancement factor. The right axis indicates with red crosses the length of the simulated time-optimal sequence of the actuator protocol.

most panel, the comparison is made with a bare Rabi frequency of $\Omega \sim 20$kHz. The enhancement factors are $\zeta_0 \sim 0.25 \times 10^{-2}$, $\zeta_{+1} \sim 1.26$ and $\zeta_{-1} \sim 1.74$. Even for the higher Rabi frequency, in particular for rotation angles $\gtrsim \pi$, the actuator protocol has a lower time-cost.

We numerically investigate the actuator implementation time for the particular unitary $\mathsf{Z}(\pi)$ for an extended range in $\{\alpha, \kappa\}$ space; the result is plotted in the leftmost panel of Figure 5-3. $\mathsf{Z}(\pi)$ is, according to our simulations, a unitary with relatively high time cost, and as such a good upper estimate of the time requirements of the actuator protocol. The thick red lines represent limiting values for κ, namely $\kappa = 1$

and a very small $\kappa = 10^{-3}$. The thin red lines, in turn, span $\kappa = 0.1$ to 0.9 in 0.1 intervals. We interpolate the numerical data to obtain the implementation times to generate $\mathsf{Z}(\pi)$ for each tabulated nuclear spin and its unique pair $\{\alpha, \kappa\}$; these implementation times are indicated by the blue crosses. As guides to the eye, we plot the direct driving times for bare Rabi frequencies $\Omega \sim 20$kHz and $\Omega \sim 83$kHz, using $\overline{\overline{\zeta}} \sim 1.41$ calculated at 500G (green lines). In particular for $\Omega \sim 20$kHz, we depict in the rightmost panel the ratio of actuator to direct driving times for the same unitary $\mathsf{Z}(\pi)$, for all electronic spin states, and as a function of radial distance ^{13}C-NV. At the particular magnetic field $B_0 \sim 500$G and Rabi frequency considered, there are nuclear spins over the whole considered radial distance range that would evolve faster if driven with the actuator protocol. Note that much larger radial distances $\gg 8$Åyield very low hyperfine couplings, and as such are neglected here.

5.4 Comparison as a function of radial distance and magnetic field

Finally, we plot the bare Rabi frequency for which the actuator implementation time of $\mathsf{Z}(\pi)$ coincides with the minimum direct driving time (namely, considering the electronic spin state for which the enhancement factor is maximal), as a function of the radial distance between the hyperfine-coupled spins, and for different values of the external magnetic field. Experimental Rabi frequencies which are lower than the depicted values at any given field will yield an advantage of the actuator control method over direct driving. In the range $B_0 \sim 250 - 500$G, Rabi frequencies that favor direct driving are relatively large, indicating a region where actuator control can prove especially beneficial.

Note, incidentally, that the upper bound on the implementation time of any considered unitary, $T \sim \frac{1}{\omega_0} \sim 2\mu$s, is still much shorter than the nitrogen-vacancy center

spin-lattice relaxation time at room temperature, $T_1 \sim$ ms [25].

5.5 Conclusion

We have numerically shown that the actuator protocol for driving the ^{13}C nuclear spin is in general advantageous over radio-frequency direct driving, especially for external magnetic fields in the range $B_0 \sim 250 - 500$G, and bare nuclear Rabi frequencies $\Omega \lesssim 20$kHz such as those which are usually obtained with modest amplifiers. Our method ensures that the nuclear evolution, steered solely by the influence of the anisotropic hyperfine coupling, be fast and noise-free.

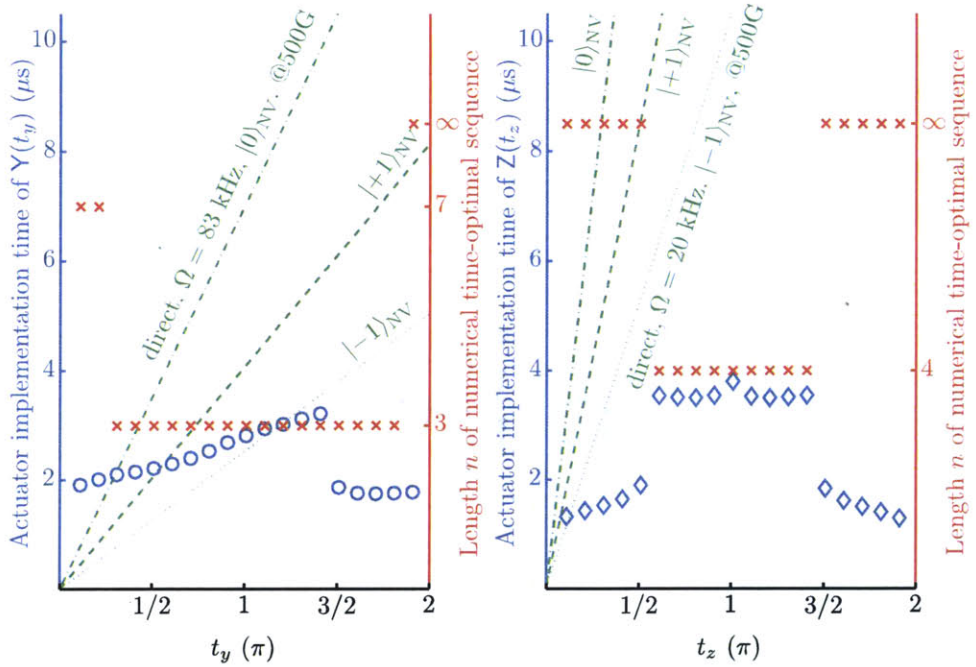

Figure 5-2: **Simulated actuator and driving times for realistic case $\kappa > \cos(\alpha)$.** It occurs, for a ^{13}C at a radial distance of ~ 2.49Å from the NV center, with an external magnetic field $B_0 \sim 500$G aligned with the $\vec{n}_x$ axis. In the left axis, we plot with blue circles the simulated times of the actuator protocol for generating: a unitary $\mathsf{Y}(t_y)$ as a function of t_y in the leftmost panel, and, with blue diamonds, a unitary $\mathsf{Z}(t_z)$ as a function of t_z in the rightmost panel. Those times are compared to the times of direct radio-frequency addressing of the nuclear spin, whose Rabi frequency depends on the different electronic spin states $|0\rangle, |+1\rangle, |-1\rangle$ (dashed-dot, dashed, and dotted green lines); in the leftmost panel, we use an estimated upper-limit of the bare nuclear Rabi frequency, namely $\Omega \sim 83$kHz, whereas in the rightmost panel, a more modest Rabi frequency of $\Omega \sim 20$kHz is employed. The right axis indicates with red crosses the length of the simulated time-optimal sequence of the actuator protocol.

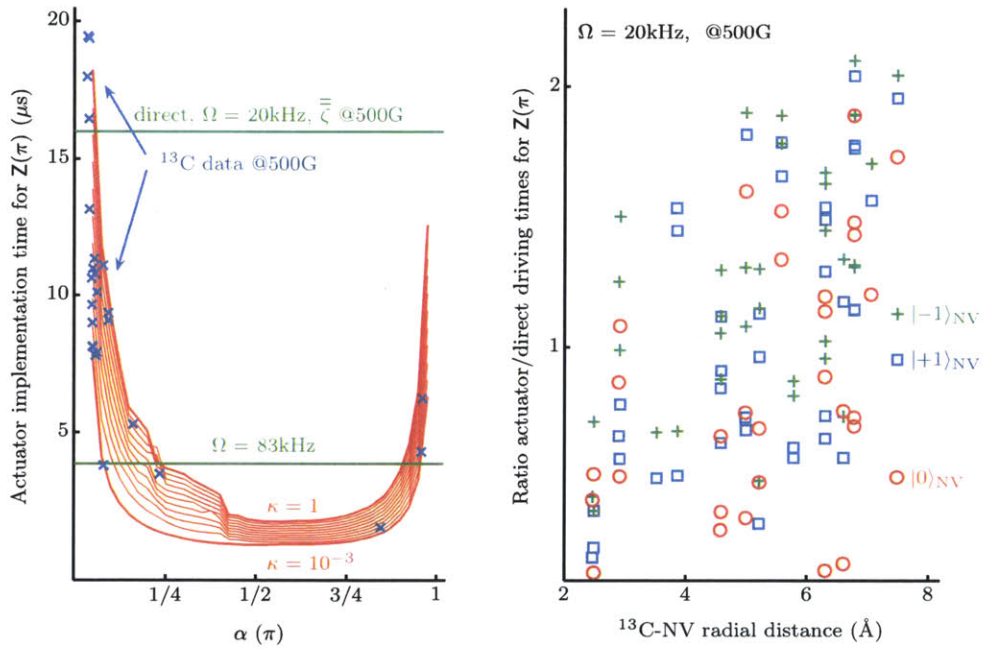

Figure 5-3: **Simulated actuator times for extended range of $\{\alpha, \kappa\}$.** In the leftmost panel, we show the simulated actuator implementation times for $\mathsf{Z}(\pi)$, for the entire α range. Values for κ span from 10^{-3} (bottom thick red line), through 0.1 to 0.9 in 0.1 intervals (thin red lines), to 1 (top thick red line). The actuator implementation times to generate $\mathsf{Z}(\pi)$ for all the tabulated carbons are plotted for comparison using blue crosses. We indicate the direct driving times for Rabi frequencies $\Omega \sim 20$kHz and $\Omega \sim 83$kHz. In the rightmost panel, we display the ratio of actuator to direct driving times in the generation of $\mathsf{Z}(\pi)$, for all three electronic spin states $|0\rangle, |+1\rangle, |-1\rangle$ (blue circles, red squares, and green plus signs, respectively), in the case of Rabi frequency $\Omega \sim 20$kHz, and as a function of radial distance between nuclear and electronic spins.

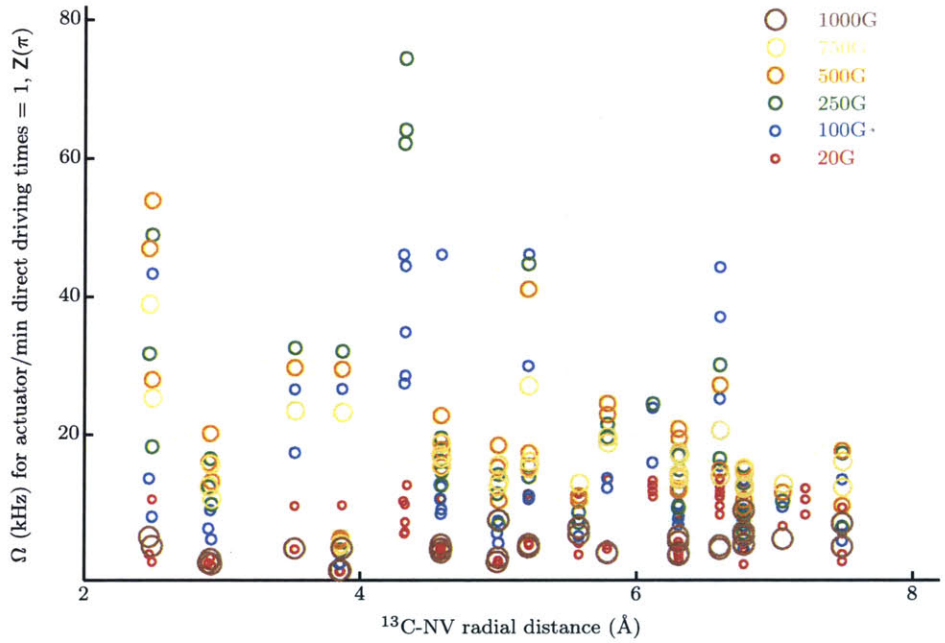

Figure 5-4: **Advantageous regimes for actuator protocol as a function of magnetic field.** Maximal bare Rabi frequency for which the actuator method is advantageous over direct driving for the implementation of $\mathsf{Z}(\pi)$, for different magnetic fields.

Bibliography

[1] J. M. Taylor, P. Cappellaro, L. Childress, L. Jiang, D. Budker, P. R. Hemmer, A. Yacoby, R. Walsworth, and M. D. Lukin, *High-sensitivity diamond magnetometer with nanoscale resolution*, Nat. Phys. **4**, 810 (2008).

[2] M. H. Levitt, *Composite pulses*, Prog. Nucl. Mag. Res. Spect. **18**, 61 (1986).

[3] I. Solomon, *Multiple echoes in solids*, Phys. Rev. **110**, 61 (1958).

[4] N. F. Ramsey, *Molecular beams* (Oxford University Press, 1990).

[5] E. L. Hahn, *Spin echoes*, Phys. Rev. **80**, 580 (1950).

[6] S. Meiboom and D. Gill, *Modified spin-echo method for measuring nuclear relaxation times*, Rev. Sc. Instr. **29**, 688 (1958).

[7] N. Kosugi, S. Matsuo, K. Konno, and N. Hatakenaka, *Theory of damped Rabi oscillations*, Phys. Rev. B **72**, 172509 (2005).

[8] H. Fedder, F. Dolde, F. Rempp, T. Wolf, P. Hemmer, F. Jelezko, and J. Wrachtrup, *Towards T_1-limited magnetic resonance imaging using Rabi beats*, Appl. Phys. B: Lasers and Optics **102**, 497 (2011).

[9] S. L. Braunstein and C. M. Caves, *Statistical distance and the geometry of quantum states*, Phys. Rev. Lett. **72**, 3439 (1994).

[10] S. L. Braunstein, C. M. Caves, and G. J. Milburn, *Generalized uncertainty relations: theory, examples, and Lorentz invariance*, Ann. Phys. **247**, 135 (1996).

[11] J. Ma, X. Wang, C. P. Sun, and F. Nori, *Quantum spin squeezing*, Phys. Rep. **509**, 89 (2011).

[12] R. J. Sewell, M. Koschorreck, M. Napolitano, B. Dubost, N. Behbood, and M. W. Mitchell, *Magnetic Sensitivity Beyond the Projection Noise Limit by Spin Squeezing*, Phys. Rev. Lett. **109**, 253605 (2012).

[13] G. S. Uhrig, *Exact results on dynamical decoupling by π pulses in quantum information processes*, New J. Phys. **10**, 083024 (2008).

[14] J.-M. Cai, B. Naydenov, R. Pfeiffer, L. P. McGuinness, K. D. Jahnke, F. Jelezko, M. B. Plenio, and A. Retzker, *Robust dynamical decoupling with concatenated continuous driving*, New J. Phys. **14**, 113023 (2012).

[15] X. Xu, Z. Wang, C. Duan, P. Huang, P. Wang, Y. Wang, N. Xu, X. Kong, F. Shi, X. Rong, and J. Du, *Coherence-protected quantum gate by continuous dynamical decoupling in diamond*, Phys. Rev. Lett. **109**, 070502 (2012).

[16] D. J. Wineland, J. J. Bollinger, W. M. Itano, F. L. Moore, and D. J. Heinzen, *Spin squeezing and reduced quantum noise in spectroscopy*, Phys. Rev. A **46**, R6797 (1992).

[17] M. Hirose, C. D. Aiello, and P. Cappellaro, *Continuous dynamical decoupling magnetometry*, Phys. Rev. A **86**, 062320 (2012).

[18] M. Duer, *Introduction to solid-state NMR spectroscopy* (John Wiley & Sons, 2004).

[19] U. Haeberlen, *High resolution NMR in solids: selective averaging* (Academic Press Inc., 1976).

[20] R. Kubo, *Generalized cumulant expansion method*, J. Phys. Soc. Jpn. **17**, 1100 (1962).

[21] V. V. Dobrovitski, A. E. Feiguin, R. Hanson, and D. D. Awschalom, *Decay of Rabi oscillations by dipolar-coupled dynamical spin environments*, Phys. Rev. Lett. **102**, 237601 (2009).

[22] P. Cappellaro, J. S. Hodges, T. F. Havel, and D. G. Cory, *Principles of control for decoherence-free subsystems*, J. Chem. Phys. **125**, 044514 (2006).

[23] K. Khodjasteh and D. A. Lidar, *Fault-tolerant quantum dynamical decoupling*, Phys. Rev. Lett. **95**, 180501 (2005).

[24] J. H. N. Loubser and J. A. van Wyk, *Electron spin resonance in the study of diamond*, Rep. Prog. Phys. **41**, 1201 (1978).

[25] A. Jarmola, V. M. Acosta, K. Jensen, S. Chemerisov, and D. Budker, *Temperature- and magnetic-field-dependent longitudinal spin relaxation in nitrogen-vacancy ensembles in diamond*, Phys. Rev. Lett. **108**, 197601 (2012).

[26] G. Waldherr, J. Beck, P. Neumann, R. Said, M. Nitsche, M. Markham, D. J. Twitchen, J. Twamley, F. Jelezko, and J. Wrachtrup, *High-dynamic-range magnetometry with a single nuclear spin in diamond*, Nature Nanotechnol. **7**, 105 (2012).

[27] L. Childress, M. V. Gurudev Dutt, J. M. Taylor, A. S. Zibrov, F. Jelezko, J. Wrachtrup, P. R. Hemmer, and M. D. Lukin, *Coherent dynamics of coupled electron and nuclear spin qubits in diamond*, Science **314**, 281 (2006).

[28] P. Cappellaro, G. Goldstein, J. S. Hodges, L. Jiang, J. R. Maze, A. S. Sørensen, and M. D. Lukin, *Environment-assisted metrology with spin qubits*, Phys. Rev. A **85**, 032336 (2012).

[29] G. Goldstein, P. Cappellaro, J. R. Maze, J. S. Hodges, L. Jiang, A. S. Sørensen, and M. D. Lukin, *Environment-assisted precision measurement*, Phys. Rev. Lett. **106**, 140502 (2011).

[30] L. P. McGuinness, Y. Yan, A. Stacey, D. A. Simpson, L. T. Hall, D. Maclaurin, S. Prawer, P. Mulvaney, J. Wrachtrup, F. Caruso, R. E. Scholten, and L. C. L. Hollenberg, *Quantum measurement and orientation tracking of fluorescent nanodiamonds inside living cells*, Nat. Nanotechnol. **6**, 358 (2011).

[31] J. R. Maze, P. L. Stanwix, J. S. Hodges, S. Hong, J. M. Taylor, P. Cappellaro, L. Jiang, A. Zibrov, A. Yacoby, R. Walsworth, and M. D. Lukin, *Nanoscale magnetic sensing with an individual electronic spin qubit in diamond*, Nature **455**, 644 (2008).

[32] G. Balasubramanian, I.-Y. Chan, R. Kolesov, M. Al-Hmoud, C. Shin, C. Kim, A. Wojcik, P. R. Hemmer, A. Krüger, F. Jelezko, and J. Wrachtrup, *Magnetic resonance imaging and scanning probe magnetometry with single spins under ambient conditions*, Nature **445**, 648 (2008).

[33] T. Gaebel, M. Domhan, I. Popa, C. Wittmann, P. Neumann, F. Jelezko, J. R. Rabeau, N. Stavrias, A. D. Greentree, S. Prawer, J. Meijer, J. Twamley, P. R. Hemmer, and J. Wrachtrup, *Room-temperature coherent coupling of single spins in diamond*, Nature Phys. **2**, 408 (2006).

[34] N. B. Manson, J. P. Harrison, and M. J. Sellars, *Nitrogen-vacancy center in diamond: model of the electronic structure and associated dynamics*, Phys. Rev. B **74**, 104303 (2006).

[35] A. Gali, M. Fyta, and E. Kaxiras, *Ab initio supercell calculations on nitrogen-vacancy center in diamond: electronic structure and hyperfine tensors*, Phys. Rev. B **77**, 155206 (2008).

[36] L. Robledo, L. Childress, H. Bernien, B. Hensen, P. F. A. Alkemade, and R. Hanson, *High-fidelity projective read-out of a solid-state spin quantum register*, Nature **477**, 574 (2011).

[37] W. V. Smith, P. P. Sorokin, I. L. Gelles, and G. J. Lasher, *Electron-spin resonance of nitrogen donors in diamond*, Phys. Rev. **115**, 1546 (1959).

[38] G. Balasubramanian, P. Neumann, D. Twitchen, M. Markham, R. Kolesov, N. Mizuochi, J. Isoya, J. Achard, J. Beck, J. Tissler, V. Jacques, P. R. Hemmer, F. Jelezko, and J. Wrachtrup, *Ultralong spin coherence time in isotopically engineered diamond*, Nat. Mater. **8**, 383 (2009).

[39] A. Schweiger and G. Jeschke, *Principles of pulse electron paramagnetic resonance* (Oxford University Press, 2001).

[40] L. Landau, *Zur Theorie der Energieübertragung*, Phys. Z. Sowjetunion **2**, 46 (1932).

[41] C. Zener, *Non-adiabatic crossing of energy levels*, Proc. R. Soc. A **137**, 696 (1932).

[42] G. L. Bretthorst, *Bayesian spectrum analysis and parameter estimation* (Springer-Verlag, 1988).

[43] D. C. Rife and R. R. Boorstyn, *Single-tone parameter estimation from discrete-time observations*, IEEE Trans. Inf. Theory **20**, 591 (1974).

[44] W. W. S. Wei, *Time series analysis: univariate and multivariate methods* (Pearson Addison Wesley, 2006).

[45] P. Neumann, J. Beck, M. Steiner, F. Rempp, H. Fedder, P. R. Hemmer, J. Wrachtrup, and F. Jelezko, *Single-shot readout of a single nuclear spin*, Science **5991**, 542 (2010).

[46] V. Jacques, P. Neumann, J. Beck, M. Markham, D. Twitchen, J. Meijer, F. Kaiser, G. Balasubramanian, F. Jelezko, and J. Wrachtrup, *Dynamic polarization of single nuclear spins by optical pumping of nitrogen-vacancy color centers in diamond at room temperature*, Phys. Rev. Lett. **102**, 057403 (2009).

[47] C. A. Meriles, L. Jiang, G. Goldstein, J. S. Hodges, J. Maze, M. D. Lukin, and P. Cappellaro, *Imaging mesoscopic nuclear spin noise with a diamond magnetometer*, J. Chem. Phys. **133**, 124105 (2010).

[48] P. Neumann, R. Kolesov, B. Naydenov, J. Beck, F. Rempp, M. Steiner, V. Jacques, G. Balasubramanian, M. L. Markham, D. J. Twitchen, S. Pezzagna, J. Meijer, J. Twamley, F. Jelezko, and J. Wrachtrup, *Quantum register based on coupled electron spins in a room-temperature solid*, Nat. Phys. **6**, 249 (2010).

[49] L. Jiang, J. S. Hodges, J. R. Maze, P. Maurer, J. M. Taylor, D. G. Cory, P. R. Hemmer, R. L. Walsworth, A. Yacoby, A. S. Zibrov, and M. D. Lukin, *Repetitive readout of a single electronic spin via quantum logic with nuclear spin ancillae*, Science **326**, 267 (2009).

[50] J. R. Klauder and P. W. Anderson, *Spectral diffusion decay in spin resonance experiments*, Phys. Rev. **125**, 912 (1962).

[51] A. Laraoui and C. A. Meriles, *Rotating frame spin dynamics of a nitrogen-vacancy center in a diamond nanocrystal*, Phys. Rev. B **84**, 161403 (2011).

[52] G. J. Augustine, F. Santamaria, and K. Tanaka, *Local calcium signaling in neurons*, Neuron **40**, 331 (2003).

[53] B. Fakler and J. P. Adelman, *Control of K_{Ca} channels by calcium nano/microdomains*, Neuron **59**, 873 (2008).

[54] D. X. Keller, K. M. Franks, T. M. Bartol Jr, and T. J. Sejnowski, *Calmodulin activation by calcium transients in the postsynaptic density of dendritic spines*, PLoS ONE **3**, e2045 (2008).

[55] M. S. Grinolds, P. Maletinsky, S. Hong, M. D. Lukin, R. L. Walsworth, and A. Yacoby, *Quantum control of proximal spins using nanoscale magnetic resonance imaging*, Nat. Phys. **7**, 687 (2011).

[56] C. L. Degen, *Scanning magnetic field microscope with a diamond single-spin sensor*, Appl. Phys. Lett. **92**, 243111 (2008).

[57] N. Khaneja, R. W. Brockett, and S. J. Glaser, *Time-optimal control of spin systems*, Phys. Rev. A **63**, 032308 (2001).

[58] A. D. Boozer, *Time-optimal synthesis of $SU(2)$ transformations for a spin-$\frac{1}{2}$ system*, Phys. Rev. A **85**, 012317 (2012).

[59] A. Garon, S. J. Glaser, and D. Sugny, *Time-optimal control of SU(2) quantum operations*, Phys. Rev. A **88**, 043422 (2013).

[60] U. Boscain and Y. Chitour, *Time-optimal synthesis for left-invariant control systems on $SO(3)$*, SIAM J. Control Optim. **44**, 111 (2005).

[61] U. Boscain and P. Mason, *Time minimal trajectories for a spin-$\frac{1}{2}$ particle in a magnetic field*, J. Math. Phys. **47**, 062101 (2006).

[62] U. Boscain, F. Grönberg, R. Long, and H. Rabitz, *Time minimal trajectories for two-level quantum systems with two bounded controls*, arXiv:1211.0666v1 [math.OC] (2012).

[63] F. Jelezko, T. Gaebel, I. Popa, M. Domhan, A. Gruber, and J. Wrachtrup, *Observation of coherent oscillation of a single nuclear spin and realization of a two-qubit conditional quantum gate*, Phys. Rev. Lett. **93**, 130501 (2004).

[64] J. S. Hodges, J. C. Yang, C. Ramanathan, and D. G. Cory, *Universal control of nuclear spins via anisotropic hyperfine interactions*, Phys. Rev. A **78**, 010303 (2008).

[65] E. Trelat, *Optimal control and applications to aerospace: some results and challenges*, J. Optimiz. Theory App. **154**, 713 (2012).

[66] L. S. Pontryagin, V. Boltianski, R. Gamkrelidze, and E. Mitchtchenko, *The mathematical theory of optimal processes* (John Wiley and Sons, Inc., 1961).

[67] A. Carlini, A. Hosoya, T. Koike, and Y. Okudaira, *Time-optimal quantum evolution*, Phys. Rev. Lett. **96**, 060503 (2006).

[68] Y. Billig, *Time-optimal decompositions in $SU(2)$*, Quantum Inf. Process. **12**, 955 (2013).

[69] D. D'Alessandro, *Introduction to quantum control and dynamics* (Chapman & Hall/CRC Press, 2008).

[70] V. Jurdjevic, *Geometric control theory* (Cambridge University Press, 1997).

[71] F. Lowenthal, *Uniform finite generation of the rotation group*, Rocky Mountain J. Math. **1**, 575 (1971).

[72] D. D'Alessandro, *Optimal evaluation of generalized Euler angles with applications to control*, Automatica **40**, 1997 (2004).

[73] U. Boscain and Y. Chitour, *On the minimum time problem for driftless left-invariant control systems on $SO(3)$*, Commun. Pure Appl. Anal. **1**, 285 (2002).

[74] V. Jurdjevic and H. J. Sussmann, *Control systems on Lie groups*, J. Differ. Equations **12**, 313 (1972).

[75] G. Piovan and F. Bullo, *On coordinate-free rotation decomposition: Euler angles about arbitrary axes*, IEEE T. Robot. **28**, 728 (2012).

[76] R. M. Murray, Z. Li, and S. S. Sastry, *A mathematical introduction to robotic manipulation* (CRC Press, 1994).

[77] A. A. Agrachev and R. V. Gamkrelidze, *Symplectic geometry for optimal control*, Non-Linear Controllability and Optimal Control; Monogr. Textbooks Pure Appl. Math. Vol. 133 (Dekker, 1990), pp. 263–277.

[78] S. Kolkowitz, Q. P. Unterreithmeier, S. D. Bennett, and M. D. Lukin, *Sensing distant nuclear spins with a single electron spin*, Phys. Rev. Lett. **109**, 137601 (2012).

[79] N. Khaneja, *Switched control of electron nuclear spin systems*, Phys. Rev. A **76**, 032326 (2007).

[80] G. Mitrikas, Y. Sanakis, and G. Papavassiliou, *Ultrafast control of nuclear spins using only microwave pulses: towards switchable solid-state quantum gates*, Phys. Rev. A **81**, 020305 (2010).

[81] J. J. L. Morton, A. M. Tyryshkin, R. M. Brown, S. Shankar, B. W. Lovett, A. Ardavan, T. Schenkel, E. E. Haller, J. W. Ager, and S. A. Lyon, *Solid-state quantum memory using the ^{31}P nuclear spin*, Nature **455**, 1085 (2008).

[82] J. J. L. Morton, A. M. Tyryshkin, A. Ardavan, S. C. Benjamin, K. Porfyrakis, S. A. Lyon, and G. A. D. Briggs, *Bang-bang control of fullerene qubits using ultrafast phase gates*, Nature Phys. **2**, 40 (2006).

[83] E. Assémat, M. Lapert, Y. Zhang, M. Braun, S. J. Glaser, and D. Sugny, *Simultaneous time-optimal control of the inversion of two spin-$\frac{1}{2}$ particles*, Phys. Rev. A **82**, 013415 (2010).

[84] S. Felton, A. M. Edmonds, M. E. Newton, P. M. Martineau, D. Fisher, D. J. Twitchen, and J. M. Baker, *Hyperfine interaction in the ground state of the negatively charged nitrogen vacancy center in diamond*, Phys. Rev. B **79**, 075203 (2009).

[85] A. Gali, personal communication.

[86] A. Abragam and B. Bleaney, *Electron Paramagnetic Resonance of Transition Ions* (Clarendon Press, Oxford, 1970).

[87] P. C. Maurer, G. Kucsko, C. Latta, L. Jiang, N. Y. Yao, S. D. Bennett, F. Pastawski, D. Hunger, N. Chisholm, M. Markham, D. J. Twitchen, J. I. Cirac, and M. D. Lukin, *Room-temperature quantum bit memory exceeding one second*, Science **336**, 1283 (2012).